


RESEARCH ARTICLE

WILEY

Geo-archaeological prospecting of Gunung Padang buried prehistoric pyramid in West Java, Indonesia

Danny Hilman Natawidjaja¹  | Andang Bachtiar² | Bagus Endar B. Nurhandoko³ | Ali Akbar⁴ | Pon Purajatnika² | Mudrik R. Daryono¹ | Dadan D. Wardhana¹ | Andri S. Subandriyo⁵ | Andi Krisyunianto⁶ | Tagyuddin⁷ | Budiarto Ontowiryo⁸ | Yusuf Maulana²

¹Research Center for Natural Disasters, National Research and Innovation Agency (BRIN), Bandung, Indonesia

²Independent Researcher, West Java, Indonesia

³Physics Department, Bandung Institute of Technology (ITB), Bandung, West Java, Indonesia

⁴Archaeology Department, University of Indonesia, Depok City, West Java, Indonesia

⁵Geology Department, Bandung Institute of Technology (ITB), Bandung, West Java, Indonesia

⁶Geosains Delta Andalan (GDA), Bekasi City, West Java, Indonesia

⁷Geography Department, University of Indonesia, Depok City, West Java, Indonesia

⁸Civil Engineering Department, Bakrie University, Jakarta, Indonesia

Correspondence

Danny Hilman Natawidjaja, Research Center for Natural Disasters, National Research and Innovation Agency (BRIN), Bandung 40135, Indonesia.

Email: danny.hilman@gmail.com

Abstract

The multidisciplinary study of Gunung Padang has revealed compelling evidence of a complex and sophisticated megalithic site. Correlations between rock stratifications observed through surface exposures, trenching and core logs, combined with GPR facies, ERT layers, and seismic tomograms, demonstrate the presence of multi-layer constructions spanning approximately 20–30 m. Notably, a high-resistive anomaly in electric resistivity tomography aligns with a low-velocity anomaly detected in seismic tomography, indicating the existence of hidden cavities or chambers within the site. Additionally, drilling operations revealed significant water loss, further supporting the presence of underground spaces. Radiocarbon dating of organic soils from the structures uncovered multiple construction stages dating back thousands of years BCE, with the initial phase dating to the Palaeolithic era. These findings offer valuable insights into the construction history of Gunung Padang, shedding light on the engineering capabilities of ancient civilizations during the Palaeolithic era.

KEYWORDS

core drilling, geophysical prospecting, megalith, pre-history, pyramid

1 | INTRODUCTION

Gunung Padang, located in Cianjur District, West Java Province, Indonesia, has been the subject of comprehensive archaeological, geological, and geophysical studies. (Figure 1, Index Map 1). Early descriptions by Veerbek (1896) and Krom (1915) described it as an ancient cemetery on top of the mound, but further investigations did not take place until local reports prompted government attention in 1979 (Bintarti, 1982). The name Gunung Padang translates to ‘mountain of

enlightenment’ in the local language, as it has been used for religious rituals throughout history (Akbar, 2013).

The National Archeological Institute conducted studies that led to the site’s restoration in 1985, and in 1998, Gunung Padang was designated a Provincial-level Cultural Heritage Site. Previous studies regarded it as a significantly large megalithic site consisting of stone terraces (Bintarti, 1982; Ramadina, 2010; Sukendar, 1985), known as *punden berundak*, which are common in Indonesia but not on the same scale as Gunung Padang. Further archaeological studies were carried

This is an open access article under the terms of the [Creative Commons Attribution](https://creativecommons.org/licenses/by/4.0/) License, which permits use, distribution and reproduction in any medium, provided the original work is properly cited.

© 2023 The Authors. *Archaeological Prospection* published by John Wiley & Sons Ltd.

out until 2005, including limited excavation pits that reached less than a meter deep (Tim-Peneliti, 2003). While lacking radiocarbon dating, it was assumed that Gunung Padang was a prehistoric site built between several hundred and a couple of thousand BCE, following regional megalithic cultures in Asia (Kim, 1982).

Situated in the southern mountainous ranges of West Java, near the headwater of the Cimandiri River, Gunung Padang is surrounded by other megalithic sites such as Kujang 1 and 2, Cengkuk, Arcadomas and Lebak Cibedug step pyramid (Figure 1, Index Map 2). The site is

located within Mio-Pliocene volcanic rocks, comprising pyroclastic, epiclastic, basaltic-andesite lava and intrusive rocks. To the north, the mountainous terrain consists primarily of Quaternary volcanic products from active volcanoes. The presence of the Cimandiri Active Fault Zone near the site poses earthquake hazards to the region (Irsyam et al., 2020; Marliyani et al., 2016).

Indonesia's tropical climate, characterized by intense weathering and sedimentation processes, combined with dense vegetation, has led to the burial and concealment of ancient cultural remains.

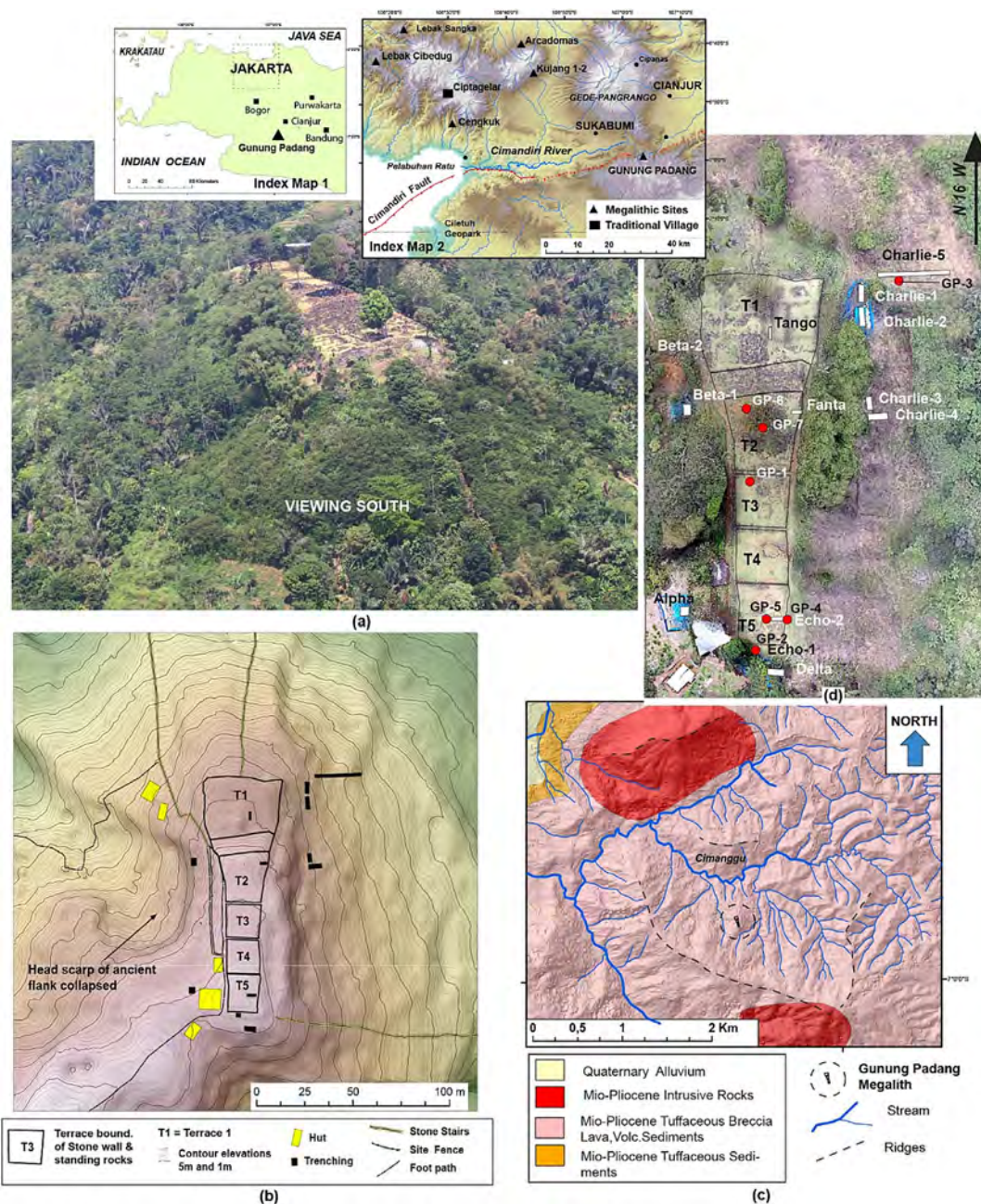


FIGURE 1 (a) Aerial view of Gunung Padang taken from a helicopter. (b) Topography and site map generated from a detailed geodetic survey. (c) Geology map of the Gunung Padang region (Sudjatmiko, 1972). (d) Orthophoto map obtained from a drone survey conducted in 2014, indicating the locations of trenching sites (white rectangles) and core-drilling sites (red dots). T1, Terrace 1; T2, Terrace 2; T3, Terrace 3; T4, Terrace 4; T5, Terrace 5. [Colour figure can be viewed at [wileyonlinelibrary.com](https://onlinelibrary.wiley.com)]

Furthermore, Indonesia's archipelago has undergone drastic climate changes over the past 15 000 years, resulting in rising sea levels and submerging ancient land known as Sundaland (Sathiamurthy & Voris, 2006; Voris, 2000). These dynamic natural processes have caused the disappearance of numerous ancient heritage sites in forests, underwater and buried underground. Traditional archaeological methods face significant challenges in their discovery. This study exemplifies how a comprehensive approach integrating archaeological, geological and geophysical methods can uncover hidden and vast ancient structures.

The field survey of Gunung Padang began in October 2011 and continued until October 2014, comprising multiple seasons. The survey encompassed detailed mapping, geological and archaeological observations, shallow geophysical surveys, excavation trenches and core drillings. It is one of the most extensive and integrated archaeological, geological and geophysical studies conducted on a buried ancient structure. The studies indicated that Gunung Padang is not merely a simple prehistoric stone terrace (e.g. Bintarti, 1982; Yondri, 2017) but a complex underground construction with substantial chambers and cavities. Carbon dating analysis indicates that it may have been constructed during the last glacial period in the Palaeolithic era, with subsequent modifications during the Holocene or Neolithic era.

The early publication of these findings in mass media outlets, along with public lectures and conferences (Natawidjaja et al., 2016, 2018), has garnered significant attention and popularity for Gunung Padang nationally and globally. Consequently, the Ministry of Education and Culture issued Decree in 2014, elevating the site's status from provincial to national heritage. The strength and significance of this study lie in the comprehensive and integrated use of multiple techniques to explore the buried and expansive ancient structures at Gunung Padang.

2 | METHODS

2.1 | Integrated multi-method studies

The integrated surveys at Gunung Padang were conducted for 3 years, from November 2011 to October 2014 (Natawidjaja, 2015, 2016, 2017). These surveys involved a combination of detailed landscape and surface mapping, core drillings, trenching and integrated geophysical techniques involving two-dimensional (2D) and three-dimensional (3D) electrical resistivity tomography (ERT), ground-penetrating radar (GPR) and seismic tomography (ST). The use of multiple methods allowed for cross-validation and enhanced interpretation of subsurface structures.

We utilized an IFSAR-5m Digital Surface Model (DSM) and Digital Terrain Model (DTM) to analyse the regional topography. These data provided a high-resolution landscape representation, enabling us to identify local features, including exposed megalithic stones and existing infrastructure. To achieve more precise mapping of these features, we conducted a geodetic survey using total stations (Figure 1b).

Additionally, we employed a small drone to perform 3D aerial surveys (Figure 1d, Figure SA.2–6). The drone-captured images were used to develop a high-resolution Digital Elevation Model (DEM), a geographically referenced mosaic orthophoto and a 3D image of the Gunung Padang mound.

2.2 | Geo-archaeological trenching

The geo-archaeological trenching activities at Gunung Padang aimed to understand better the vertical profile and lateral extensions of the buried structures near the surface. The selection of trenching sites was based on the interpretations derived from the preceding geophysical surveys. The trenching operations commenced mid-2012, with most work conducted in August–September 2014. Trench sizes varied, ranging from 1×2 to 3×9 m on the surface, and depths reached between 2 and 4 m, except for Echo1, which was excavated to 11 m. The trenches were manually dug using various tools, including spades and hoes. The trenches were carefully backfilled upon completing the excavations, and measures were taken to prevent erosion by replanting the surfaces.

2.3 | Core drilling

The core drilling activities were undertaken to explore the deeper rock layers. For this purpose, we employed Jacro 100 drilling equipment equipped with a diamond bit NQ measuring 2 in. in diameter and 5 ft core barrels (Figure SC.7). The collected rock cores were subjected to petrological and petrographic analysis to gain insights into their composition and characteristics. Additionally, the drilling operations allowed us to delineate the interface between the rock formations and groundwater, providing valuable information about the hydrological aspects of the site. Organic soil samples were carefully extracted from the spaces between rock fragments, which were subsequently used for carbon dating analysis. In specifically targeted locations, drilling activities aimed to explore suspected large underground cavities. These drilling operations were executed carefully and cautiously to ensure that no megalithic stones exposed on the surface were disturbed or removed. Suitable open spaces were selected for drilling, and customized wooden constructions were utilized as foundations for the drilling equipment (Figure SC.7c).

2.4 | Radiocarbon analysis

This study represents the first comprehensive analysis of ^{14}C dating at the Gunung Padang site. Organic soil samples obtained from the drill cores and the trenching walls were meticulously selected for ^{14}C dating analysis. These organic samples were believed to contain traces of bio-organic activities during and after the construction phases. However, it is essential to consider potential sources of contamination, such as older carbon sources or recent bio-organism activities,

which could impact the dating results. Notably, modern vegetation and roots were identified as the most common sources of contamination, leading to significantly younger age determinations (Natawidjaja et al., 2017). Great care was taken during sample collection to avoid modern vegetation.

Additionally, any remaining carbons derived from modern vegetation were separated and thoroughly cleaned during laboratory processing. Most samples were analysed using the accelerator mass spectrometry (AMS) dating method at the BETA Analytic Lab in Florida, USA. Some samples were analysed using the conventional carbon dating method at the National Nuclear Energy Agency (BATAN). The OxCal program was utilized to calibrate the results of the conventional ^{14}C ages and to conduct a robust chronological analysis (Bronk Ramsey, 2016).

2.5 | Shallow geophysical prospecting

The application of high-resolution shallow geophysical methods in archaeological studies has grown significantly over the past two decades (e.g. Tsokas et al., 1994). However, the extensive use of geophysical prospecting to investigate buried and expansive ancient structures, particularly pyramids, remains uncommon (e.g. Papadopoulous et al., 2010; Tejero-Andrade et al., 2018). Geophysical surveys that combine extensive excavations and core drillings to validate and refine interpretations of the imaged geophysical features are relatively rare (e.g. Shi et al., 2020). Most archaeological prospecting efforts have focused on uncovering smaller buried structures or features ranging from tens of centimetres to several meters in scale, such as tombs (e.g. Sarris et al., 2007).

The research conducted at Gunung Padang breaks new ground by employing multi-high-resolution geophysical methods on a large scale, addressing the challenges associated with investigating vast ancient structures. By integrating these methods with extensive excavations and core drillings, the study offers a unique and comprehensive approach to exploring the hidden complexities of the site. This pioneering methodology provides valuable insights into the nature and construction of the structures, surpassing the limitations of traditional archaeological prospecting techniques focused on more minor features.

2.6 | GPR survey

For the GPR survey, we utilized SIR-2000 and SIR-3000 GSSI units equipped with various antennas, including unshielded multiple low frequency (MLF) and shielded 100- and 270-MHz antennas (<https://www.geophysical.com>). However, the field conditions posed limitations on the GPR survey. It was not feasible to conduct high-slope survey lines due to issues with topographic correction, and heavily vegetated areas required path clearance for effective surveying. Therefore, this study primarily focused on using GPR on flat, clear ground atop megalithic terraces.

During the survey, we experimented with different antennas and frequencies, primarily focusing on the MLF antenna that was deemed most suitable for our objectives. The MLF antenna was employed at 15, 40 and 80 MHz frequencies. However, it was found that the 40 MHz frequency provided the optimal balance between resolution and depth penetration for our study, reaching depths of up to 30 m. The 15 MHz frequency did not achieve significant depth penetration on the site while exhibiting lower resolution. Additionally, using the 80 MHz frequency did not yield improved imaging results, leading us to solely present the outcomes obtained with the MLF 40-MHz antenna.

We employed the common-offset measurement technique to acquire data along the survey lines, incrementally capturing point data at intervals of 50–100 cm. These acquired data points were then processed using RADAN software that comes with the GSSI units. The processing steps included time-zero shifts, topographic correction, noise filtering, background removal, deconvolution, migration and depth conversion utilizing the Common Depth Point (CDP) method to estimate the radar wave velocity through the subsurface layers. The CDP measurement provided a radar wave velocity of 1.08×10^9 m/s, equivalent to a dielectric constant of 8.09, which was subsequently utilized to convert the travel time of radar waves into depth measurements.

We employed various colour spectrums in the radargrams to visualize and interpret the processed data. A neutral conventional grey colour scheme was utilized to display contrasting degrees, textures and patterns, while a red-blue colour spectrum was employed to highlight the positive and negative polarities of radar waves. Bright spots observed in the radargrams corresponded to high-amplitude reflections from subsurface materials with a higher dielectric constant, whereas dark spots or negative polarity reflections indicated materials with a lower dielectric constant. GPR facies analysis was conducted to identify radar stratifications, and the results were subsequently compared to the borehole, ERT and ST data for comprehensive analysis and interpretation.

2.7 | ERT survey

ERT data played a crucial role in this study, offering valuable insights into the subsurface structures (Figure 8a, Figure SF). ERT surveys provide flexibility in terms of target resolution, coverage and desired depth of penetration by adjusting the electrode spacing. This method can be conducted in various field conditions, including high slopes and areas with dense vegetation. For data acquisition, we utilized the SuperSting R8 multichannel resistivity system from Advanced Geoscience Inc (<https://www.agiusa.com/>) with two sets of 56 and 112 electrode cables configured at different spacing intervals, predominantly employing a dipole–dipole configuration.

The electrode spacing directly affects the resolution and penetration depth of the ERT data. Wider electrode spacings yield greater depth penetration but sacrifice spatial resolution. The penetration depth is approximately 10 times the spacing for the 56-electrode

cable and 15 times the spacing for the 112-electrode cable—moreover, the penetration depth increases when surveying over convex surfaces. The spatial resolution is typically half the electrode spacing, meaning that with a 5-m spacing, the resolution is around 2.5 m. To accurately measure the topographic profiles along the survey lines, we employed the ZIPL Level Pro-2000 High Precision Altimeter, known for its sub-millimetre accuracy (<https://www.ziplevel.com/>). Data processing was conducted using the EarthImager 2D and 3D software included with the SuperSting system.

ERT surveys were performed with various electrode spacing configurations for 2D, 2.5D grid and 3D surveys (Figure 8a, Figures SF.3–SF.6). By employing different electrode spacings, we obtained ERT images with a wide range of resolutions and penetration depths. This allowed us to investigate shallow and deeper objects in detail and compare variations in models to enhance interpretations. The primary ERT data for this study were obtained from a 2-m spacing electrode survey conducted along NS (North–South) and EW (East–West) parallel lines with 5- to 10-m spacing between the lines, covering the upper part of the mound. Consequently, a 2.5D spatial analysis was performed (Figure SF.14). Additionally, gridded 1-m spacing electrode lines were utilized (Figure 8a, Figure SF.15). To image the entire mound from top to base, we employed larger electrode spacings of 3, 4, 5 and 8 m (Figures SF.7 and SF.8). Furthermore, a 3D survey was conducted on the megalith terraces using a 5-m spacing grid spread across four parallel-line cables, covering an area of approximately 15×135 m to explore suspected large cavities.

2.8 | ST survey

ST is not commonly employed in archaeological prospecting but offers several advantages over conventional seismic refraction methods (e.g. Forte & Pipan, 2008). One key advantage is the superior velocity information obtained from tomography, surpassing the layering models used in conventional seismic refraction. Additionally, the heterogeneities and complexities of the subsurface structures at Gunung Padang may limit the applicability of seismic reflection methods.

In this study, we conducted three ST lines: Line-1 running north–south, crossing T1–5 and the entire mound; Line-2 and Line-3 running east–west, crossing ramp T1–2 and T-5, respectively (Figure 12a). Data acquisition was performed using a 2×24 channel seismograph set with a spacing of 5 m. Firecrackers or sledgehammers were utilized as seismic sources, positioned in the middle of each receiver (geophones), and fired at 5-m intervals. Data were continuously downloaded to the hard disk of a portable PC while repositioning the shot point. This configuration allowed for high-resolution ST with deep penetration. The topography of Gunung Padang, resembling an inverted boat, facilitated line configurations that covered the targets at a sufficient aperture angle (Figure SG1A), significantly enhancing the capability of ST to reveal shallow and deep targets, including large cavities.

We employed the Fresnel wavepath tomography method, which combines ray path and phase components based on the Rytov

approximation (Nurhandoko, 2000, 2016; Nurhandoko et al., 1999, 2016; Nurhandoko & Ashida, 1998; Vasco et al., 1995). The Fresnel wavepath is thin at higher frequencies and wider at lower frequencies. To achieve stable inversion, we performed the inversion procedure using a wide wavepath and gradually transitioned to a thinner wavepath by sweeping the frequency component. This approach ensured stable tomography inversion, and the smoothed procedure based on the wavepath frequency was adopted in the inversion process. By incorporating a broad spectrum of frequencies for inverse modelling, multiple alternative tomography images with varying resolutions were generated (Figures SG.3–SG.5). Comparing these multi-images improved the visualization and interpretation of the subsurface structures. For further details on the method and results, refer to Figure SG.

3 | RESULTS

3.1 | Observations of megalithic exposures and the surroundings

The landscape of Gunung Padang reveals an isolated and elongated hill, oriented south–north, with symmetrical and flat east and west flanks. The hilltop is characterized by a flat-truncated surface adorned with stone terraces embellished with standing stones, known as menhirs. This majestic amphitheatre-like structure faces northward, offering a captivating view of the Gede-Pangrango active volcano complex (Figure 1, Index Map 2; Figure SA.1). Water streams encircle the perimeter of the mound that eventually merge with the Cimanggu River, the principal branch of the Cimandiri River. The surrounding higher mountainous ridges exhibit advanced erosions, resulting in rough terrains with streams eroding the slopes. This terrain landscape, characterized by intense erosion, is typical of the region's Tertiary rock terrain (Soeria-Atmadja et al., 1994). In contrast, the upper half of Gunung Padang displays a remarkably smooth surface, indicating a lesser degree of erosion. This observation provides an initial clue that Gunung Padang is a more recent feature than the surrounding landscapes.

The Gunung Padang megalithic site consists of stone terraces cascading northward, occupying the elongated flat top of the hill, which rises approximately 200 m above the main river in the north or around 100 m above the entrance gate in the parking lot where a stone stairway leads to the top (Figure 1a). The site comprises five substantial rectangular stone terraces, named Terraces 1, 2, 3, 4 and 5 (referred to as T1, T2, T3, T4 and T5) from north to south (Figure 1b,c). These megalithic stones primarily consist of naturally formed basaltic-andesite columnar-joint rocks, resulting from the cooling of hot igneous liquid under specific temperature and pressure conditions. Terrace T1 spans 30×40 m (width \times length) and is separated from T2 by a 9-m high ramp. T2 measures 20×25 m, T3 is 18×18 m, T4 is 17×17 m, and T5 is 15×18 m. The terraces are divided by 50-cm steps between T2 and T3 and T3 and T4, while a 1-m step separates T4 and T5. The exteriors and interiors of the terraces are adorned

with alignments of rock walls and rows of standing columnar rocks, forming intricate spatial patterns and geometries (Figure 2). In 2014, the vegetation on the east slope was cleared to reveal these stone terraces (Figure 1d, Figure SA.2); however, they have since become heavily vegetated once again (Figure SA.3–4). Pyroclastic and epiclastic rocks predominantly occupy the lower part of the hill.

A comparative example of stone terraces is Lebak Cibedug, a stepped pyramid close to Gunung Padang, which shares a similar size and antiquity but has not been extensively studied (Takashi, 2014). Another example is Candi Kethek in Central Java (Purwanto et al., 2017). Stone terraces constructions can be found worldwide, such as Machu Picchu in Peru, built by the Inca civilization (Bingham, 1930). Nan Madol, a megalithic complex on Pohnpei Island, Micronesia, utilizes similar columnar-joint rocks (McCoy et al., 2016; McCoy & Athens, 2012). Interestingly, based on oral traditions, the Saudeleur Dynasty, the newcomers to Pohnpei Island, is believed to have constructed Nan Madol (McCoy et al., 2016). The pronunciation of 'saudeleur' is remarkably similar to the Sundanese word 'sadulur',

meaning 'one family' in the local language of West Java, which is significant considering Gunung Padang's location. Some columnar rock arrangements observed in Gunung Padang resemble those found in Nan Madol (Figure 2c).

3.1.1 | Multi-phase construction and hidden layers

The visual observations at Gunung Padang reveal a complex construction history, with evidence of multiple phases and diverse architectural styles. At the ground surface, known as Unit 1 (#1), the prominent megalithic stones exhibit a variety of arrangement techniques positioned on soils containing numerous andesite rock fragments (Akbar, 2013). Unit 1 comprises columnar rock arrangements of standing rocks and ramps, defining the spatial geometry and terrace spaces (Figure 2c). Notably, interwoven columnar rocks form ascending stone steps from the lower levels, while tall rock walls enclose T1 (Figure 2e). Intriguingly, this study unveils that Unit 1 stone terraces

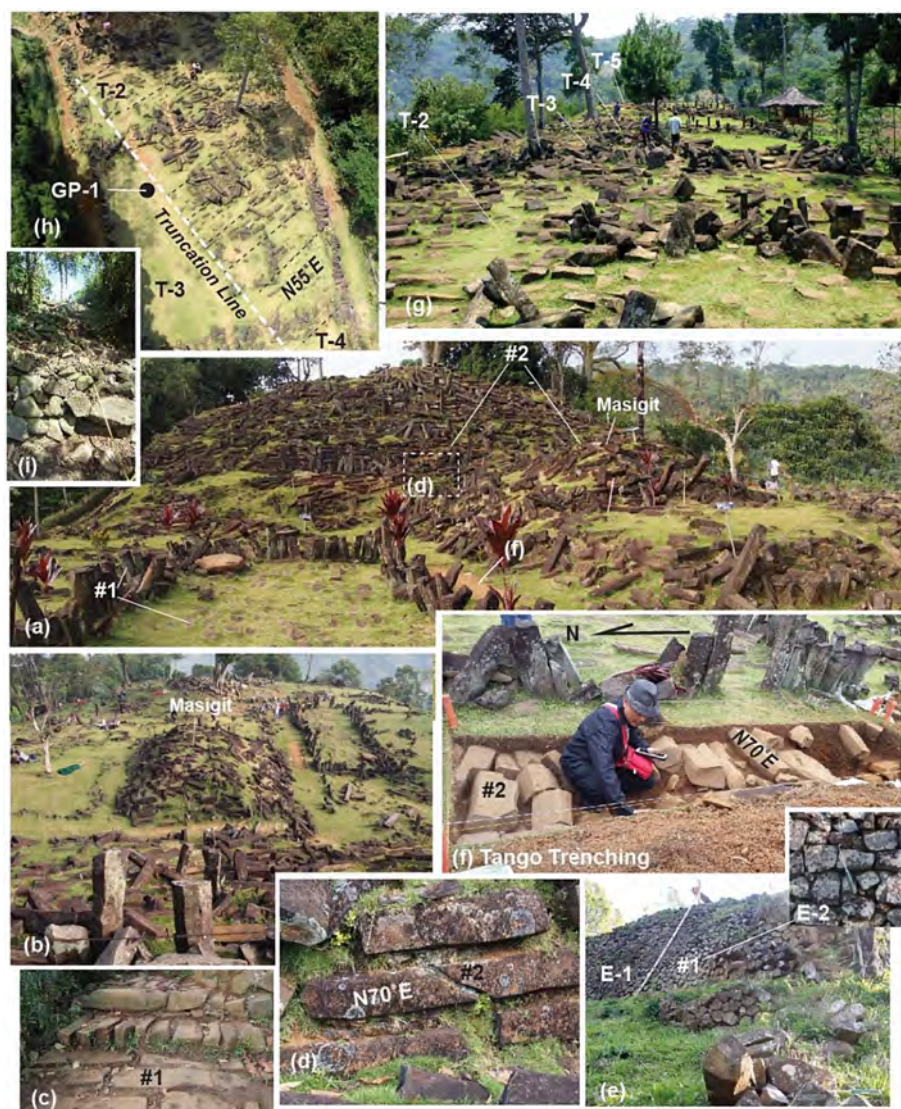


FIGURE 2 Surface exposures of megalithic stones illustrating two units of construction, Unit 1 (#1) and Unit 2 (#2). (a) South-facing view of T1 landscape, revealing a stone floor and standing columnar rocks of #1, as well as the exposed #2 ramp and altar. (b) North-facing view from T2 onto T1. (c) Columnar rock arrangement example of #1. (d) Unit 2 on the ramp between T1 and T2, showcasing columnar rock fragments enclosed in a fine-grained mortar. (e) Columnar rock wall of #1 construction encircling the margin of T1. (f) Tango trench on T1 exposing the thinly buried #2 columnar rock, aligned in N70°E similar to those on the ramp. (g) Southward view of T2, T3, T4 and T5. (h) Overhead photo of T2 and T3, demonstrating the N55°E alignment of #2 columnar rock with a truncation line. (i) GPR survey uncovering #1 step-stone terraces on the east slope. [Colour figure can be viewed at [wileyonlinelibrary.com](https://onlinelibrary.wiley.com)]

extend beyond the hilltop, visible on the east slope and in other cleared areas (Figure 2i). It has been confirmed that these terraces were not recently constructed by local inhabitants for agricultural purposes (Akbar, 2013). Unfortunately, significant portions of the stone terraces on the hill slopes have not been preserved.

Beneath Unit 1 lies an older layer of columnar rocks displaying more sophisticated construction techniques. These regularly cut columnar rocks are arranged like bricks in a building, with fine-grained fillers or mortar between them (e.g. Figure 2d). This layer, called here as Unit 2, remains hidden in plain sight, with exposed parts.

Exposed areas reveal various elements of Unit 2, including (1) the stone-wall ramp between T1 and T2 (Figure 2a,d), (2) an altar-shaped rock mound situated in the middle of T1, referred to as Masigit (meaning 'a place for praying') (Figure 2a, b), and (3) diagonally oriented tiles of columnar rocks spanning T2 and T3 in an approximately N55E direction (Figure 2h). Notably, on T1, the top of Unit 2 lies just a few tens of centimetres beneath the ground surface, as uncovered by the Tango trench (Figure 2f). The interwoven columnar rocks beneath T1 and the ramp connecting T1 and T2 are aligned similarly in the N70°E direction. This evidence confirms that Unit 2 is a product of human construction, challenging previous notions that it consisted solely of natural columnar rocks (e.g. Yondri, 2017).

We have mapped a sizeable ancient flank collapse or large landslide on the west slope (Figure 1b). A part of its head scarp, Beta2 cliff, exposes not just Unit 1 and Unit 2 but also an older unit beneath them. The three layers are parallel to the ground surface (Figure 3). Unit 1 has many rock fragments of broken columnar-joint basaltic-andesitic rocks. Beneath it, Unit 2 is the interwoven columnar-joint basaltic-andesitic rocks aligned in approximately N70°E direction, like those exposed on T1. The columnar-joint rocks, unlike in nature, are stacked parallel to the layer, not perpendicular, and have been regularly cut about 1–2 m long on average. Furthermore, natural columnar-joint rocks are more homogeneous in size and shape and are tightly interlocked, but Beta2 exposure exhibits columnar rocks with different shapes and diameter sizes, and their surfaces do not interlock directly but are separated by fine-grained mortar (Figure 3b,c). The orthogonal sections of the columnar rocks vary in shape, including hexagonal, pentagon, rectangular, trapezoidal and triangular. There are also distinct thin-flat rocks between the columnar blocks, probably added to tighten the structure (Figure 3d). Like exposures on T1, the mortar between the columns has an average thickness of 5 cm. The columnar rocks are only slightly weathered, showing sharp corner edges.

The Beta2 scarp is critical in providing evidence of Unit 2's foundation. It reveals a distinct and sudden boundary where Unit 2 meets the underlying rock layer, which has undergone extensive weathering and decay. This layer consists of homogeneous, coarse sands with a gravelly texture, possibly originating from a variety of volcanic rock materials. It is evident that this layer was exposed to the air for a significantly more extended period before being covered by Unit 2. In contrast to the homogeneous mass, there are embedded pillar-like structures that contain columnar rocks. These columnar rocks have experienced advanced spheroidal weathering, resulting in rounded

corners and edges caused by exfoliation (Figure 3e). This rock-pillar structure appears to be an integral part of the overall construction. We designate the homogeneous mass layer as Unit 3A and the decayed columnar rocks as Unit 3B. The observed weathering profile is intriguing since natural weathering typically occurs due to exposure to air and water, resulting in weathering and decay towards the ground surface rather than the opposite.

3.2 | Results of trenching

The trenching excavations were conducted at 12 selected sites (Figure 1b,d), each with its designated name. These sites include Tango on T1, Alpha on the west side of T5, Charlie1, Charlie2, Charlie3, Charlie4 and Charlie5 on the East Slope, Delta on the south slope, Echo1 near the southern edge of T5, Echo2 on T5 and Fanta at T2.

The trenching excavations revealed that Unit 2 is a substantial construction that extends vertically and laterally along the west and east flanks. This indicates that the megalithic stones on the ground surface (Unit 1) are built upon the buried and more massive Unit 2. Unit 1 appears to be a surface re-arrangement of Unit 2. In the Fanta Trench at T2, the alignment of columnar rocks observed on the surface continues underground (Figure 4A2,A3; Figure SB.2). Although the trench reached a depth of 3.5 m, it did not reach the base of Unit 2, which can be seen at Beta2 on the west slope (Figure 3). Unit 2 extends down to the east slope, as revealed by the Charlie 1–5 trenches (Figure 4B1). The layer of columnar rock dips at an angle of about 15° on the east and west slopes, while both flanks incline 30° (Figure 4B2). The flat surfaces of the east and west hill flanks represent the top of Unit 2, which is buried beneath 1–2 m of soil containing numerous broken basaltic-andesite rock fragments.

The geometry of Unit 2 is complex. The alignment of columnar rocks on T1 and the ramp and on the east and west slopes is approximately N70°E, perpendicular to the long axis of the megalithic structure. On T2 and T3 and down to their slopes, as revealed by the Charlie3 and Charlie4 trenches, the alignment of columnar rocks is approximately N55°E. It is worth noting that the stone blocks that resemble bricks are not always columnar rocks. For example, the Charlie2 trench on the east slope reveals neatly packed irregular rock slabs/fragments aligned in a similar orientation to the columnar rocks (Figure 4e).

In Trench Echo2 on T5, a steep wall constructed from interwoven columnar rocks is exposed but buried under a soil fill (Figure 4c). According to the GP5 core drilling data described in the next section, the thickness of the soil fill is approximately 7 m (Figure 6). The columnar rocks in this trench have undergone extensive weathering, exhibiting spheroidal weathering similar to those in Unit 3B of the Beta2 scarp. Hence, it is considered part of Unit 3. Although Echo2 was excavated to a depth of 4 m, the base of the columnar rock wall was not reached.

The Delta trench on the south slope of T5 exposes a 3-m-thick layer of homogeneous soil fill that buries decayed and unrecognizable



FIGURE 3 Beta-2 cliff exposures on the west slope. (a) Field photo and interpreted stratigraphy of the subsurface layers. (b) Side view highlighting Unit 2 and its distinct boundary with the underlying Unit 3. (c) Plan view of Unit 2, showcasing the alignment of columnar rocks enclosed in a fine-grained mortar. (d) Photo displaying planar rock fragments inserted between columnar rocks. (e) Photo featuring a weathered vertical pillar composed of highly weathered columnar rocks surrounded by fine-grained materials. [Colour figure can be viewed at [wileyonlinelibrary.com](https://onlinelibrary.wiley.com/doi/10.1002/arp.1912)]

rocks, characterized by large rounded rock fragments instead of columnar rocks. These rocks display intensive concentric exfoliations indicative of spheroidal weathering. This rock layer, classified as part of #3, is named #3C. On top of this buried decayed rock mass, a unique stone artefact resembling a traditional Sundanese dagger called *Kujang* Stone was discovered (Figure 4d,D1). It was found alongside some granular quartz crystals not associated with the weathered rocks beneath it.

3.3 | Results of core drillings

Core drillings were conducted at seven selected sites around the hill-top (Figure 1d) with varying depths. The deepest core drilling, GP5 on T5, reached 36 m. The drillings penetrated Unit 1, Unit 2 and Unit 3, as well as a deeper section composed of massive basaltic-andesite rocks referred to as Unit 4 (Figures 5 and 6). The characteristics of each rock unit are summarized in Table 1.

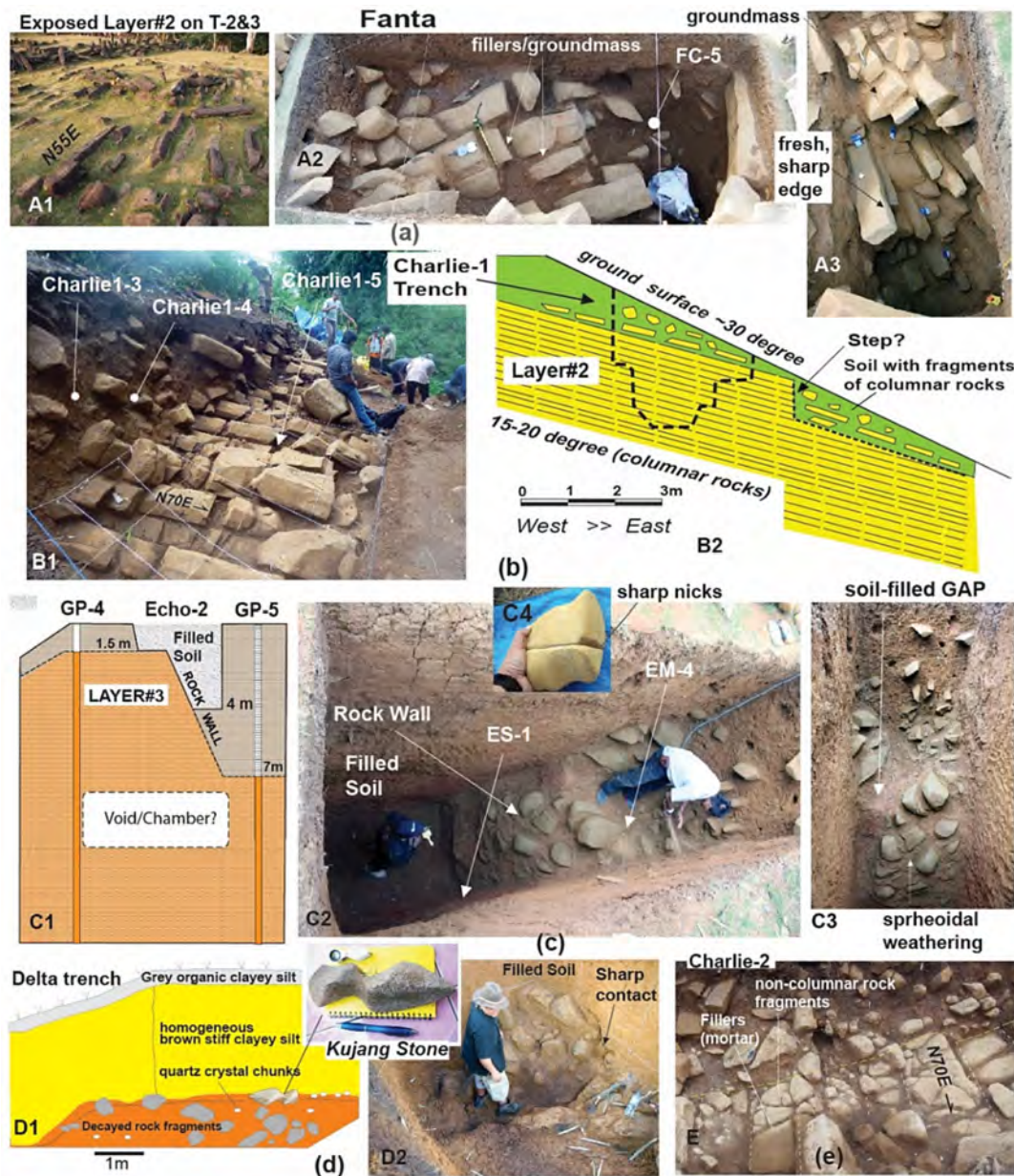


FIGURE 4 Results of geo-archaeological trenching. (a) Fanta trench: A1. Columnar rock alignment visible on the surface of T2, A2. Oblique view revealing underground continuation of columnar rock alignments (#2), A3. Front profile of #2 columnar rocks exhibiting various sizes and shapes, encased in a 5-cm-thick mortar. (b) Charlie1 trench on the east slope: B1. N70E-oriented columnar rock alignment (#2) dipping 15° towards the slope, B2. Cross-section drawing of Charlie1 trench. (c) Trenching Echo2: C1. East-west cross-section drawing of Echo2 trench, C2. Oblique view displaying buried Unit 3 rock wall, C3. Front view of steep wall comprising highly weathered columnar rock alignment. (d) Delta trench on the south slope: D1. Drawing of the trench, D2. Photo revealing rounded, highly weathered rock fragments buried by homogeneous soil fill. (e) Trenching Charlie2 on the east slope: N70E alignment of non-columnar, blocky rock fragments enclosed in mortar. FC-5, Charlie1-3,4,5, EM-4 and ES-1 represent sample locations for radiocarbon analysis. [Colour figure can be viewed at wileyonlinelibrary.com]

Unit 1 represents the topsoil or near-surface soil, typically less than 1 m thick, containing fragmented columnar basaltic-andesite rocks. In GP2, GP4 and GP5 boreholes on T5, an ancient soil fill was discovered, burying Unit 3 rocks beneath the topsoil (refer to Figure 6).

Unit 2, referred to as #2, is easily identifiable as it can be seen both on the ground surface and in the trenches. It consists of columnar basaltic-andesite rocks held together by a sandy-silt mortar of

anthropogenic origin. The individual cores of the columnar rocks have smooth planar surfaces and typically measure between 20 and 30 cm in length, representing their typical diameter. At the base of Unit 2, there is a relatively thick layer of soil, occasionally containing loose gravelly sands.

Unit 3, or #3, shares similarities with Unit 2 but is considerably more weathered, often showing signs of water circulation loss during drilling. The length of andesite cores in Unit 3 can exceed 30 cm,

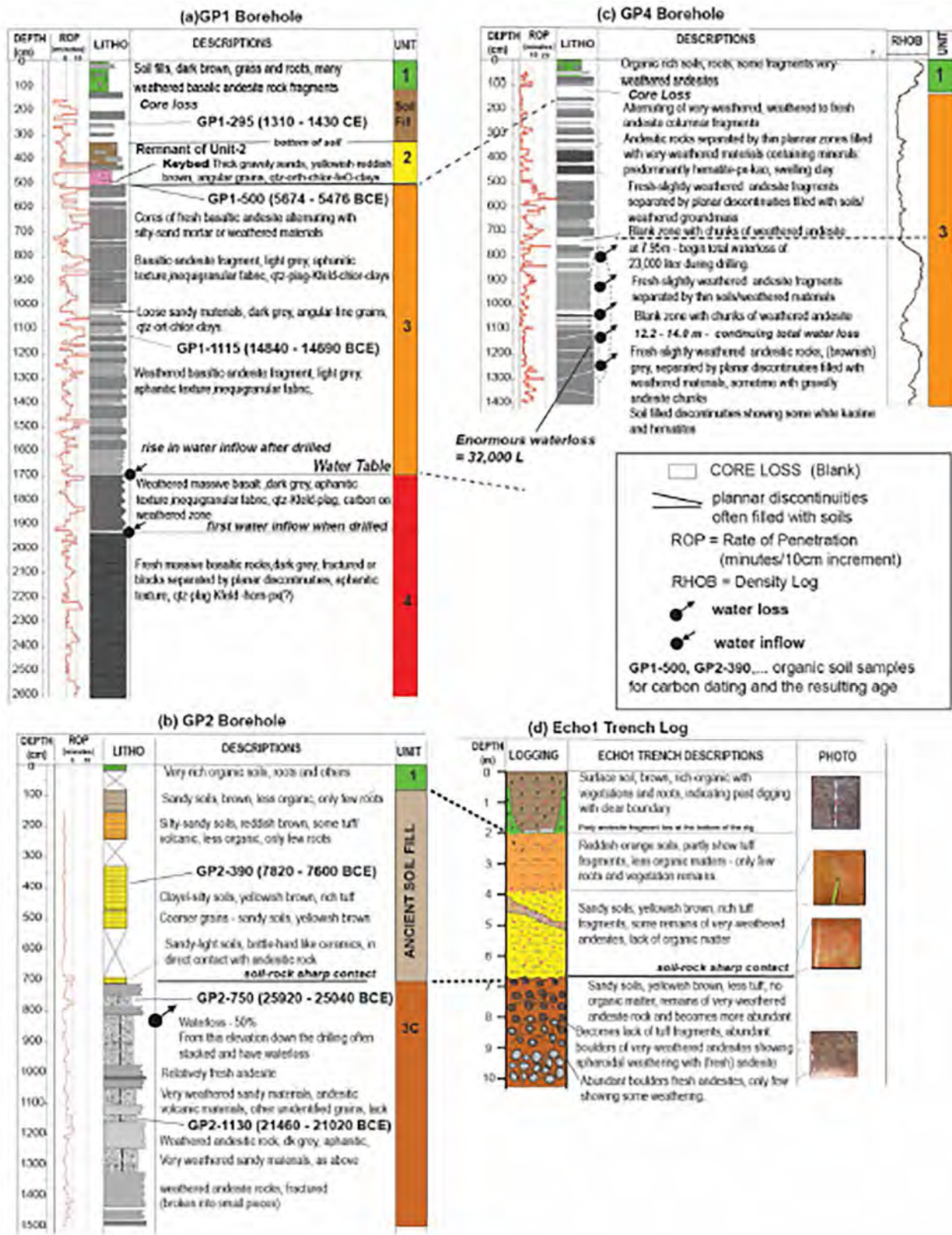


FIGURE 5 Borehole logs and interpreted stratigraphy units. (a) GP1 borehole. (b) GP2 borehole. (c) GP4 borehole. (d) Logging of the deep trenching Echo1. Figures SC.3-SC.6 provide detailed logging information for other boreholes. [Colour figure can be viewed at wileyonlinelibrary.com]

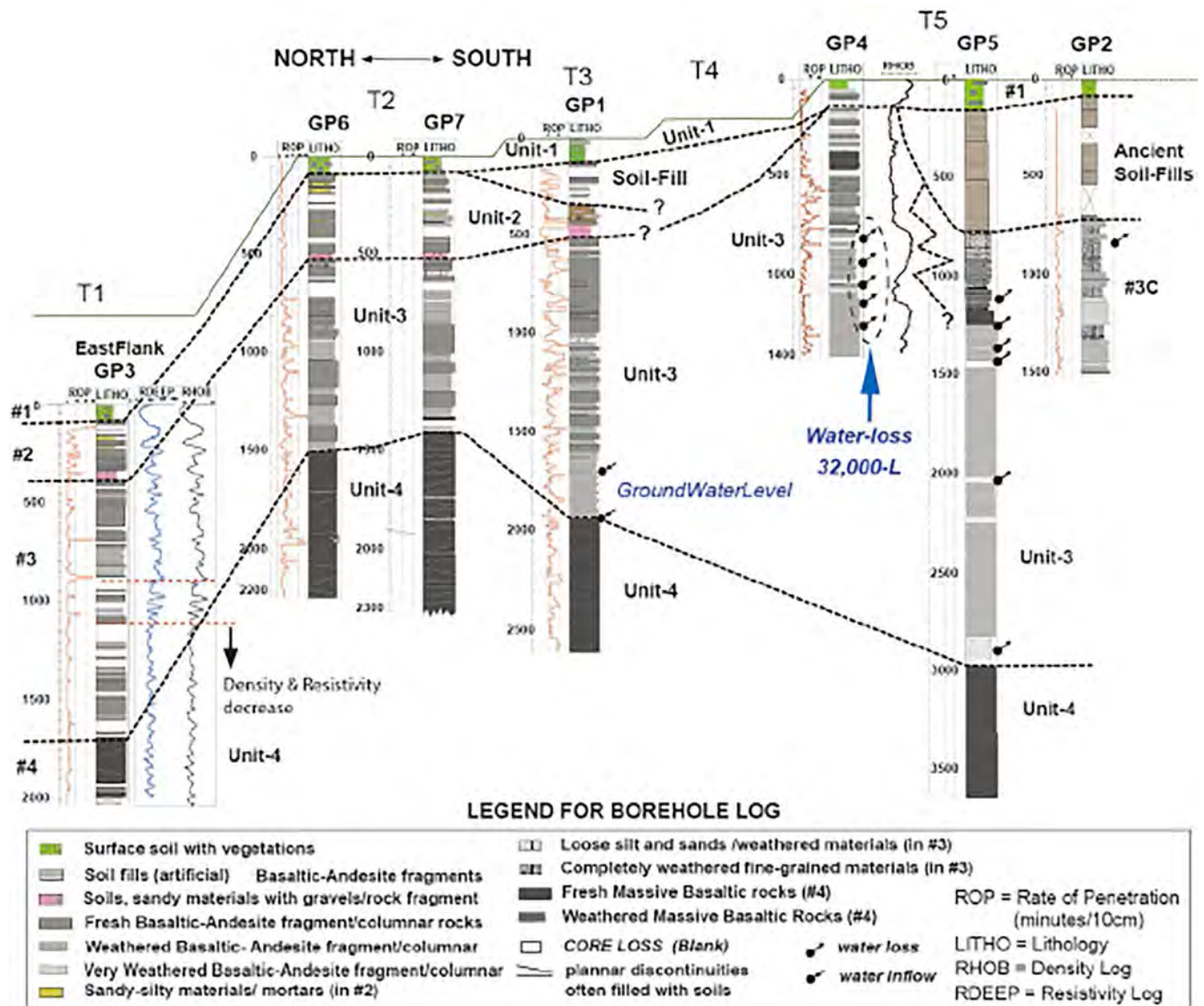


FIGURE 6 Summary of all core logs showing stratigraphic units and their correlations. Descriptions of each rock unit can be found in Table 1. It should be noted that Unit 2 does not extend to T5 and Unit 3 is buried by ancient soil fills at T5. During GP4 drilling, a significant water loss of 32 000 L (32 m³) was observed between 8- and 14-m depth. Evidence of groundwater level was observed through water inflow at a depth of 17 to 20 m in GP1. [Colour figure can be viewed at wileyonlinelibrary.com]

reaching up to 1.3 m in GP7, suggesting the presence of columnar rocks in oblique or vertical positions. However, Unit 3 also contains rounded rock fragments, referred to as #3C, encountered in GP2 or Echo1. The boundary between weathered columnar rocks and rounded rocks in Unit 3 remains unclear.

Unit 4, known as #4, is not exposed on the ground surface and consists of massive basaltic-andesite rocks with intensive fractures. This characteristic was observed in GP1, GP3, GP5, GP6 and GP7 boreholes (see Figure 6 and Figure SC.3–10). The rocks in Unit 4 are generally in a fresh state or exhibit minimal weathering. In GP1, the top of Unit 4 is identified by a heavily weathered, 2-m-high massive basaltic andesitic rock associated with fluctuations in groundwater levels, evident through water inflow during drilling (refer to Figure 5a).

Two distinct soil fills were encountered. The first type, referred to as ancient soil fills, was found in GP5 and GP2 boreholes and exposed in the Echo1 and Echo2 trenches. These fills have a thickness of up to 7 m and completely bury Unit 3, indicating no gradual in situ weathering (refer to Figures 4c, 5b and SC.8). The sharp contact between the soil fills and the top of Unit 3 suggests their human origin rather than natural soil formations. GP5 borehole revealed three different types of soils in the fills, further supporting their artificial nature. The second type of soil fill was found in T4, T3 and T2 on the west side of the columnar rock truncated line (see Figure 2h). The GP1 borehole on T2 revealed that Unit 2 had been almost entirely excavated before the soil fills covered the remaining structures.

TABLE 1 The classification of rock units based on comprehensive analysis and interpretation of the collected data obtained from boreholes, trenches and surface exposures.

Unit	Descriptions	Thickness (m)	Core loss	Water loss
Soil fill	Dark brown soils with many columnar rocks fragments encountered in GP-1	~3	—	—
Unit 1 (#1)	Surficial megalithic stone and underlying topsoil; dark brown with many grassroots and frequently contains many broken (columnar) basaltic-andesite rock fragments	1–2	—	None
Unit 2 (#2)	Horizontal columnar rocks intercalated with fine-grained mortar; identified in the cores as rock fragments bounded by planar surface and intercalated by mortar or soils; rock-core lengths are generally 20–30 cm. Not present in GP2, GP4 and GP5	2.5–4 m	Frequent	None
#2 soil base	Thick soils often mark the bottom of Unit 2, sometimes containing loose gravely sands, angular grains, yellowish-reddish brown colours, quartz, feldspar and some clays		—	—
Ancient soil fill	Thick soil fills, burying Unit 3 beneath T-5, showing some layering of brown, reddish-orange and yellowish-brown soils, some remnant of very weathered andesites and lack of organic matter. Encountered in GP2 (Echo-1) and GP5 and in Echo-2 trench	Up to 7 m	Frequent	—
Unit 3 (#3)	Weathered columnar and rounded rock fragments (#3B & 3C) showing spheroidal weathering, intercalated with soils or weathered materials; andesite-rock cores are generally 15–30 cm long, but occasionally longer, up to 1.3 m. present in all boreholes.	8–22 m	Frequent	Frequent in GP-2, GP-4 and GP-5; 32 m ³ at GP-4
Unit 4 (#4)	Massive basaltic-andesite rocks, generally fresh rocks, and many fractures. Encountered in GP1, GP3, GP5, GP and GP7	Not known	Rare	None

Drilling initially took place at GP2 to a depth of 15 m (Figure 5b). However, further excavation was carried out at this site, referred to as the Echo1 trench, reaching approximately 11 m (Figure 5d). This excavation exposed ancient soil deposits that buried extensively weathered rocks consisting of basaltic-andesitic rock boulders exhibiting exfoliation due to spheroidal weathering. These boulders were embedded in a highly weathered matrix (#3C). This excavation highlighted the challenge of identifying rock types based solely on core samples. Fresh basaltic-andesite boulders were observed at the bottom of the Echo1 trench, while weathering gradually intensified towards the surface. Notably, these rounded boulders are typically found in rivers, where they undergo transportation through rolling and abrasion by water streams. However, the presence of these boulders on top of the hill suggests that they were brought up to this location.

The GP4 borehole contains crucial data regarding the suspected presence of large cavities or chambers beneath the surface. During drilling, the penetration rate slowed down at a depth of 5 m. At 7 m, the drill encountered a ‘blank zone’ with no core samples. Subsequently, at 8 m, there was a sudden and significant water circulation loss exceeding 20 000 L. After this point, the drilling penetration accelerated and maintained a high speed. The water loss continued until the total unreturned water circulation reached approximately 32 000 L (32 m³) at a depth of 14 m, prompting us to halt the drilling. The substantial water loss strongly indicates the presence of a large underground cavity.

The GP5 borehole, strategically positioned near the centre of T5, was initially selected to investigate the suspected presence of a

significant cavity or chamber. However, during drilling, no such feature was encountered. To delve deeper into this possibility, we excavated in trench Echo2, situated between GP4 and GP5. Regrettably, the excavation only reached a depth of 4 m, which proved insufficient to confirm the existence of the cavity. Instead, we uncovered a steep rock wall. It is plausible that the large cavity does not extend beneath T5 but rather towards the east slope. Further exploration and excavation in this area are necessary to gather more conclusive evidence.

Boreholes GP7 were also conducted to investigate the presence of a significant primary chamber beneath the centre of the megalith site. However, drilling was halted at a depth of approximately 21–22 m without discovering any large cavities. Nevertheless, at a depth of 10 m in GP7, we encountered a lengthy andesitic rock core measuring 1.3 m. This core may indicate the presence of a vertical structure, such as a wall or gate, as supported by the ST profile discussed in the following section.

Considering our goal of drilling directly into the chamber, we contemplated drilling into the steep wall between T1 and T2. However, this task requires special permission since drilling without removing or disturbing the megalithic structures on the surface at this particular location is impossible.

Petrographic analysis of thin sections from the rock core samples obtained from the GP1 borehole was conducted to examine their mineralogical compositions and determine their rock types (Figure SJ). The results indicate that the mineralogical compositions of the rock cores from #1 to #4 units are similar, consisting of basaltic-andesite rocks. The visible minerals under a microscope include feldspars,

pyroxene, chlorite and opaque minerals. Based on visual estimates, the mineral constituents comprise 20%–30% feldspar, 15%–20% mafic minerals, 5% opaque minerals and 55% groundmass. The feldspars present include plagioclase varieties such as bytownite, labradorite and andesine. Mafic minerals are predominantly represented by clinopyroxene, specifically augite and hornblende, with scarce occurrences of olivine. Opaque minerals are primarily composed of magnetite.

The groundmass consists of microlite plagioclase feldspar, very fine-grained mafic minerals and a glassy matrix, which have undergone partial alteration to chlorite and sericite. The rocks show only slight alterations, and some display 5%–7% porosity due to the presence of vesicular holes. Based on the sizes of microscopically visible vesicular holes, ranging from 0.5 to 2 mm in diameter, these basaltic-andesite rocks are believed to be part of shallow lava intrusions. There are no significant changes in mineralogy from top to bottom, except that rocks from Unit 4 exhibit a slight increase in more basic minerals, indicating a transition towards more basaltic rocks. Therefore, in the core log, the rocks from Unit 4 are referred to as basaltic rocks for brevity in the descriptions (Figure 5a).

3.4 | Results of carbon dating analysis

We collected a total of 12 organic soil samples, with six obtained from borehole core samples and the remaining six from trenches. Out of these samples, eight underwent analysis using the AMS radiocarbon method at BETA Analytic Lab (www.radiocarbon.com), while the other four were analysed using the conventional radiocarbon method at the Geochronology Lab in BATAN. To calibrate the carbon dating results, we employed the OxCal modelling approach (Ramsey, 2007, 2016), which utilizes Bayesian statistics and considers factors such as the material being dated, the calibration curve used (in this case, SHCAL20), and the stratigraphical and archaeological context of the dated object. Additionally, prior information and assumptions about age can be incorporated into the analysis. The detailed results of the carbon dating analysis are presented in Table 2, with further information provided in Figure SD.

The comprehensive OxCal analysis, as illustrated in Figure 7, provides invaluable insights into the chronological sequence of the constructions at Gunung Padang. According to the analysis, Unit 3 is estimated to have been constructed during the remarkable timeframe

TABLE 2 The results of carbon dating analysis conducted as part of the study. The conventional ^{14}C ages obtained from the samples have been calibrated to calendar ages using the OxCal software. The table provides an overview of the calibrated ages for the analysed samples, allowing for a more accurate understanding of the chronological timeline associated with the studied materials. For additional information and details regarding the carbon dating analysis, please refer to Figure SD.

Sample no.	Lab. no.	Loc.	Depth (cm)	Material	Layer	Conventional ^{14}C age	Calendar age (2 σ)
FC5	BETA# 423691	Fanta Tr.	130	Organic soil	Soil fill	480 \pm 30 BP	1419–1499 CE, 1601–1611 CE
GP1-295	BETA# 331493	GP-1	295	Organic soil	Soil fill	560 \pm 30 BP	1393–1449 CE
CH1-3	–	Charlie-1 Tr.	55	Organic soil	Unit 1	3025 \pm 30 BP	1383–1341 BCE, 1311–1107 BCE, 1096–1079 BCE, 1069–1056 BCE
CH1-4	–	Charlie-1 Tr.	82	Organic soil	Unit 1	3630 \pm 40 BP	2131–2087 BCE, 2047–1872 BCE, 1847–1814 BCE, 1805–1775 BCE
EM4	BETA# 423689	Echo-2 Tr.	150	Organic soil	Bottom of Unit 1	3630 \pm 30 BP	2121–2095 BCE, 2040–1876 BCE, 1843–1822 BCE, 1795–1780 BCE
CH1-5	–	Charlie-1 Tr.	121	Organic soil	Unit 2	7095 \pm 60 BP	6061–5793 BCE
GP1-500	–	GP-1	500	Organic soil	Soils beneath Unit 2	6700 \pm 70 BP	5713–583 BCE, 5675–5478 BCE
GP2-390	BETA# 331495	GP-2	390	Organic soil	Ancient soil fill	8710 \pm 40 BP	7931–7924 BCE, 7816–7588 BCE
ES1	BETA# 423690	Echo-2 Tr.	350	Organic soil	Ancient soil fill	7400 \pm 30 BP	6371–6296 BCE, 6269–6081 BCE
GP1-1115	BETA# 331494	GP-1	1115	Organic soil	Unit 3	13 510 \pm 50 BP	14 468–14 086 BCE
GP2-750	BETA# 331496	GP-2	750	Organic soil	Unit 3	22 750 \pm 120 BP	25 337–24 941 BCE, 24 772–24 525 BCE
GP2-1130	BETA# 331498	GP-2	1130	Organic soil	Unit 3	19 400 \pm 80 BP	21 789–21 577 BCE, 21 487–21 090 BCE

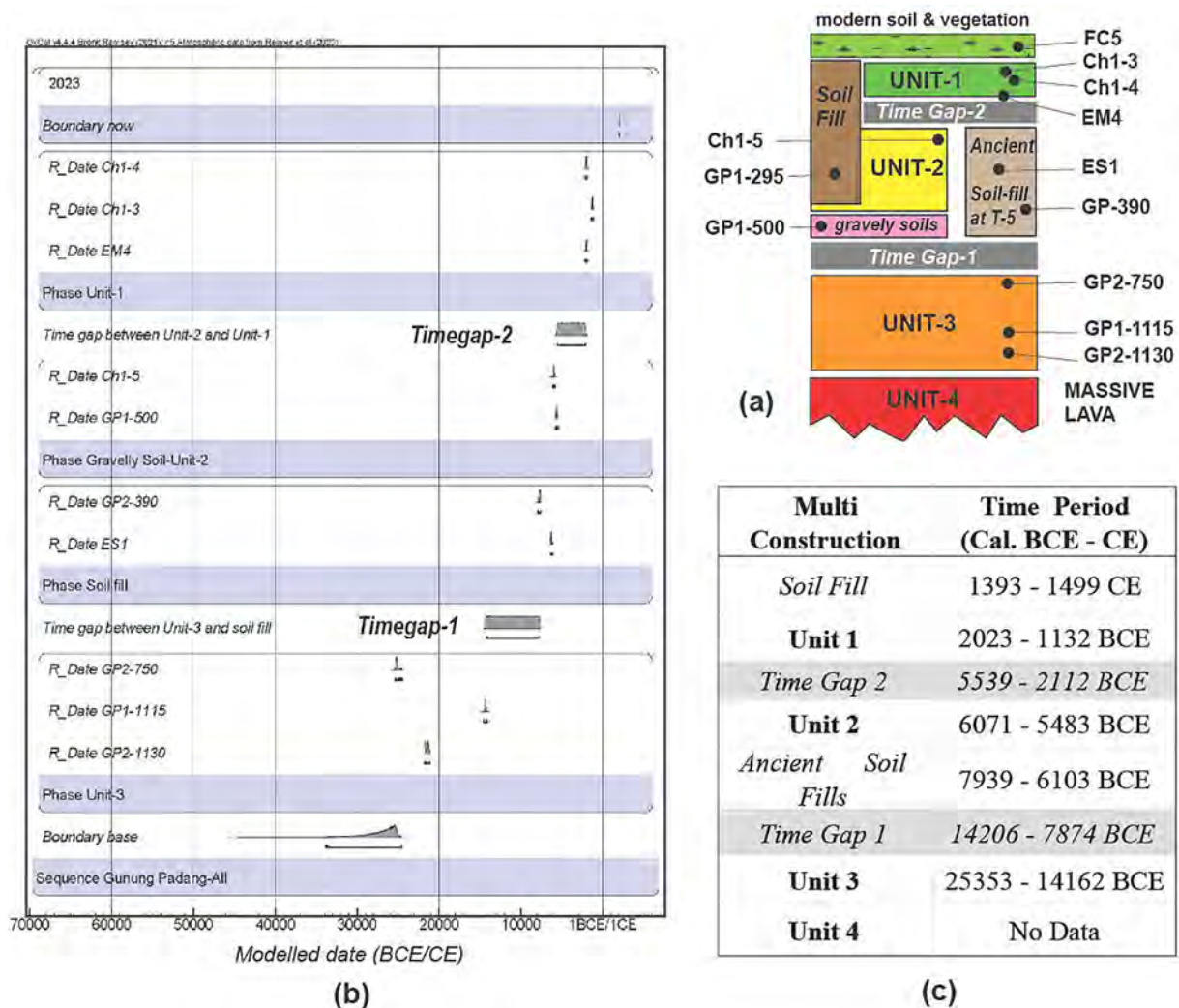


FIGURE 7 The OxCal analysis of the multi-construction histories of the Gunung Padang pyramid, including soil-fill burials and time gaps between constructions. (a) Stratigraphic model and carbon-dating samples associated with each layer. (b) Results of the OxCal modelling, showing the estimated dates for each construction phase. (c) Summary of the OxCal analysis results, providing an overview of the chronology of the constructions. [Colour figure can be viewed at [wileyonlinelibrary.com](https://onlinelibrary.wiley.com/doi/10.1002/arp.1912)]

of 25 000 to 14 000 BCE. Following this period, there was a hiatus spanning from 14 000 to 7900 BCE before Unit 3 was ultimately buried between 7900 and 6100 BCE. Remarkably, approximately two millennia later, the construction of Unit 2 took place between 6000 and 5500 BCE. Another significant hiatus occurred from 5500 to 2100 BCE, followed by the construction of Unit 1 between 2000 and 1100 BCE. Lastly, an intriguing excavation of Unit 2 and subsequent soil fills transpired between 1393 and 1499 CE. These refined chronological estimates provide a deeper understanding of the temporal development and evolution of the structures at Gunung Padang throughout its extensive history.

The estimated ages of the units align with their respective degrees of weathering. Unit 1, characterized by relatively fresh columnar basaltic-andesite rock, is estimated to be around 4000–3000 years old, consistent with previous studies (Bintarti, 1982; Tim-Peneliti, 2003). Unit 2, which exhibits significantly more

weathered columnar rocks than Unit 1, aligns well with the estimated age of 7500–8000 years. The estimated age of Unit 3, at least 16 000 years old, corresponds to the extensive decay and exfoliations observed in its rocks due to spheroidal weathering.

3.5 | Results of GPR survey

We conducted more than 30 survey lines using the MLF 40-MHz antenna, including the long continuous survey through the megalithic site's longitudinal axis (Figure 8b, Figure SE.2). The main findings of the survey are presented in Figure 9, where radargram stratifications are classified into distinct GPR facies based on established analysis methods (Ékes & Hickin, 2001; Lanzarone et al., 2019; Lee et al., 2005). These facies exhibit unique textures, patterns, amplitudes, frequencies and reflector-geometrical shapes. The boundaries

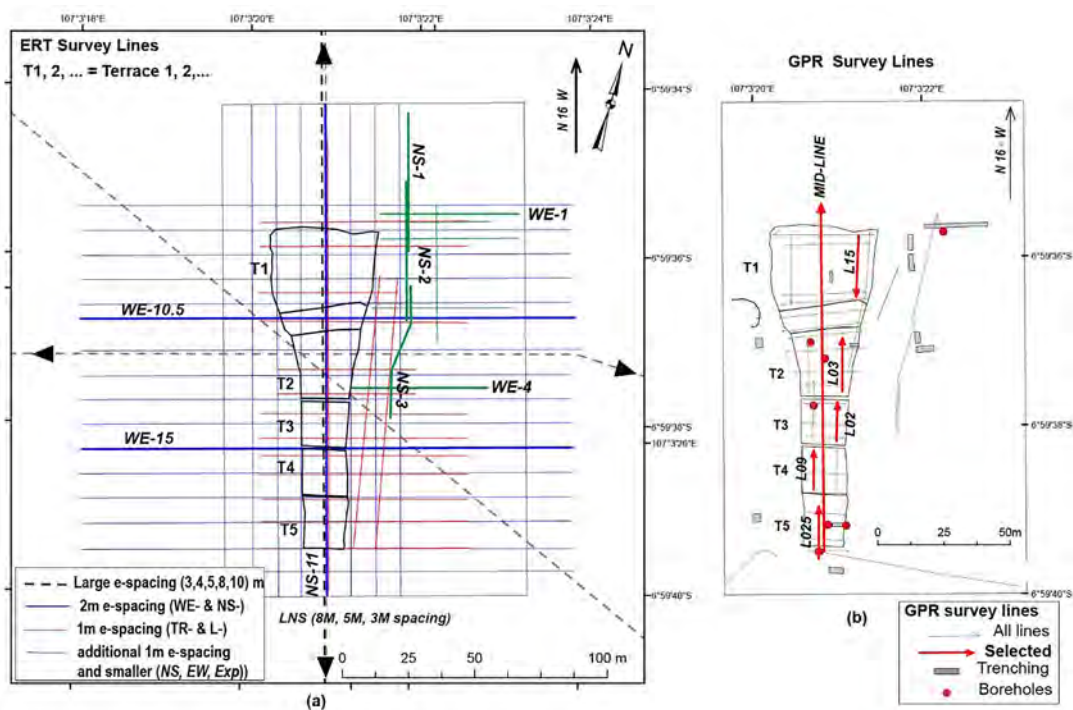


FIGURE 8 Index map for shallow geophysical surveys. (a) Electrical resistivity tomography (ERT) survey lines with various electrode spacing, including 1, 2, 3, 4, 5, 8 and 10 m. The bold blue and green lines indicate the selected survey lines presented in Figure 10. (b) Ground-penetrating radar (GPR) survey lines using a 40-MHz MLF antenna, with the selected survey lines for Figure 9. [Colour figure can be viewed at wileyonlinelibrary.com]

between facies are often marked by strong negative or positive reflectors (Table 3, Figure 9). For further details, refer to Table 3 and Figure SD.

Facies A exhibits strong amplitudes of parallel reflectors extending to a depth of approximately 5 m. Within Facies A, two subfacies can be identified. Facies A-1, found in the upper 1–2 m, are characterized by continuous and parallel solid reflectors. At a depth of 2–5 m, Facies A-2 displays more irregular and wavy reflector patterns. However, on radargrams, it may be challenging to distinguish between Facies A-1 and A-2. Strong thick negative reflectors often underlie Facies A, serving as its boundary.

Facies B, spanning from 5 to at least 15 m in depth, exhibits low amplitudes and indicates smooth textures. Within Facies B, there are two subfacies. Facies B-1 is characterized by a homogenized low-amplitude smooth texture, occasionally adorned by slightly stronger, discontinuous low-frequency reflectors. As we descend, Facies B-2 becomes dominated by discontinuous wavy bands of higher-amplitude reflectors. The presence of strong positive and negative reflectors often demarcates the boundary between Facies B-1 and B-2.

Facies C is distinguished by its parallel and discontinuous reflector pattern, ranging from weak to strong. Within this facies, strong reflectors occasionally denote its upper boundary.

The primary south–north cross-sectional radargram along the long axis of the megalith reveals that the subsurface layering generally

mirrors the topographic profile of the ground surface (Figure 9). In simpler terms, the underground layers appear horizontal beneath the flat ground surface and inclined beneath sloping surfaces, such as the ramp between T1 and T2. The overall geometry of the subsurface structures along the long axis is depicted in Figure 9b, with the more detailed information provided by short survey lines conducted on each terrace, as illustrated in Figure 9a. Additional radargrams can be found in the supplementary data (Figure SE.3–8).

The radar facies exhibit a strong correlation with the stratification of rock units (Figure 13, Figures SE2–7 and SH4). Facies A-1 and A-2 align well with the layers of Unit 1 and Unit 2. The presence of solid and parallel reflectors in Facies A may indicate the horizontal layering of columnar rocks. Facies B corresponds to Unit 3. Facies B-1 is associated with the upper portion of Unit 3, which consists of heavily weathered rocks, as exposed in Beta2. These homogeneously weathered rocks tend to display smooth textures and low amplitudes on radargrams. Facies B-2 correlates with the lower part of Unit 3 (#3B, #3C) in terms of depth and characteristics. The radargram exhibits a smooth, low-amplitude background with discontinuous wavy reflectors, likely representing intensively decayed rock fragments and mortars. The presence of strong, thick negative reflectors separating Facies A and B is likely to correspond to the thick soils underlying Unit 2, as observed in the cores (indicated by the pink layer in Figure 6, Figure 13). Starting from a depth of approximately 15–20 m, Facies C correlates with Unit 4, consisting of massive basaltic andesites.

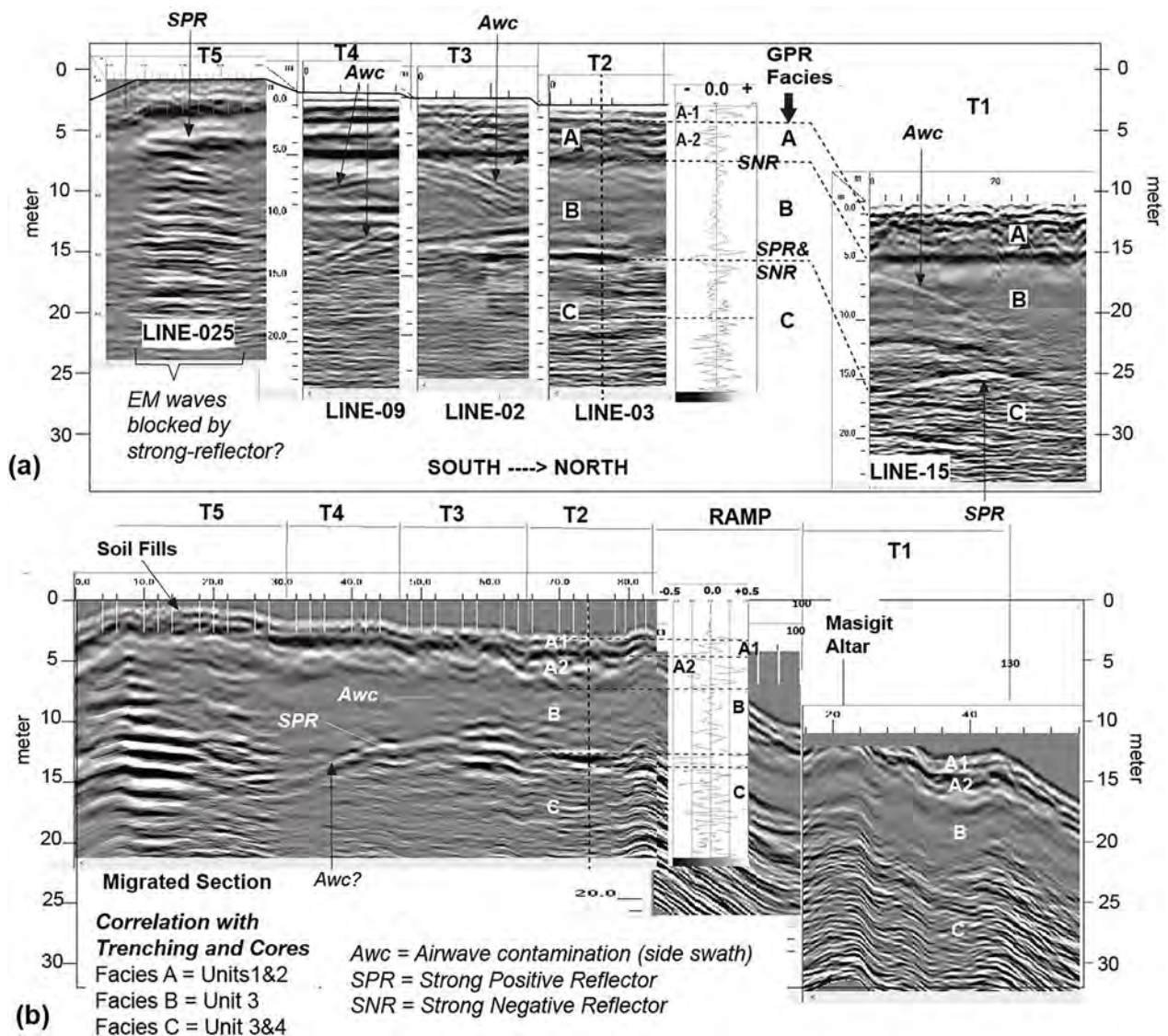


FIGURE 9 Summary of GPR prospecting. (a) Selected short-line radargrams on terraces displaying detailed textures, patterns, polarities, GPR facies analysis and their correlations. (b) The mid-line, a principal radargram of the continuous longitudinal survey line that traverses the stone terraces. All radargrams have undergone filtering, convolution and migration processes. [Colour figure can be viewed at [wileyonlinelibrary.com](https://onlinelibrary.wiley.com/doi/10.1002/arp.1912)]

3.6 | Results of ERT survey

3.6.1 | 2D ERT survey



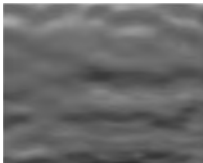
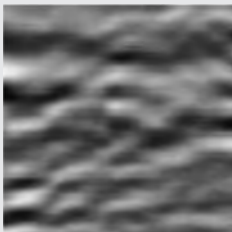
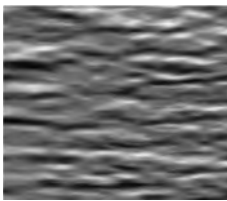
The robust 2D ERT survey lines provide extensive and detailed data on the subsurface structures of the megalithic site (Figure 8a, Figures SF.3–SF.5). Similar to radargrams, the inverted-model sections of the ERT 2D data display parallel layers that replicate the topographic profile of the ground surface (Figure 10). It is important to note that an ERT section does not directly reflect the true resistivity structures of the subsurface, but rather represents the result of an inversion modelling process using the acquired resistivity data (see Figure SF.2). Therefore, like other geophysical methods, it does not yield a unique, single-solution model. Different initial conditions and variations in resistivity inversion settings result in ERT sections with

varying geometric details. However, high-quality data will exhibit similar general structural patterns.

The ERT images obtained from the 2.5D gridline surveys, employing 1 and 2-m electrode spacings, generally display consistency and can be cross-correlated (Figures SF.14 and SF.15). Furthermore, the findings of this study demonstrate that the ERT resistivity structures remain consistent at various resolutions using different electrode spacing ranging from 1 to 10 m in both the west–east and south–north directions (Figure 10, Figures SF.7–SF.13).

Mt Gunung Padang is surrounded by pyroclastic and epiclastic volcanic rocks with low resistivity values. Consequently, on ERT surveys with wider electrode spacings, Gunung Padang appears as a high-resistive anomaly (Figures SF.7 and SF.8). However, at finer scales, the upper part of this high-resistive anomaly is enveloped by significantly lower-resistive layers. The ERT resistivity structures can

TABLE 3 The results of the radar facies analysis conducted on the radargrams obtained from the GPR survey using the MLF 40-MHz antenna. The table provides a classification and description of the various radar facies identified in the radargrams. Each radar facies is characterized by distinct textures, patterns and structures, allowing for a better understanding of the subsurface features and their interpretations. The table serves as a reference for the interpretation and analysis of the GPR data.

Radar facies	Description	Example	Correlation
Facies A1	High amplitude, moderate frequency, strong continuous horizontal reflectors, sometimes have a sigmoid pattern		Unit 1
Facies A2	High amplitude, low frequency of sigmoid to irregular reflectors, often underlying by a solid negative reflector		Unit 2
Facies B1	The smooth texture of low-amplitude reflectors with horizontal to discontinuous dipping reflectors of low to medium amplitude		Unit 3A Upper part
Facies B2	Low amplitude, smooth background, interspersed with a discontinued horizontal and dipping reflector of medium-high amplitude. Downward becomes smoother texture and higher frequency		Unit 3B, 3C Lower part
Facies C	High frequency and low to high reflectors with horizontal but discontinued patterns, sometimes irregular or chaotic		Unit 4 (massive andesite)

be categorized into four layers, designated as Layer-a, Layer-b, Layer-c and Layer-d (Figure 10). This layering consistently appears in all ERT sections conducted with 2-m electrode spacing (Figures SF.9 and SF.10). Moreover, this stratification pattern remains visible even with electrode spacing of up to 5 m (Figures SF.7 and SF.8).

Starting from the top, Layer-a represents an intermediate resistivity layer, which can be further divided into a1 and a2. The a1 layer is thin and exhibits moderate resistance (mostly depicted in green on the figures). The a2 layer is thicker and displays higher resistance (ranging from yellow to red). Layer-b (depicted in green) shows significantly lower resistance compared to (the lower part of) Layer-a. Layer-c is a high-resistive layer, typically measuring over 700–1000 Ω -m. It often exhibits a distinct and smooth top surface. Layer-d, located beneath Layer-c, exhibits low resistance.

In correlation with the rock units, Layer-a roughly corresponds to Unit 1 or Unit 1 and Unit 2 (Figure 13, Figure SH). Layer-b correlates with the upper part of Unit 3 (#3A). The top of Layer-c, the high-resistive layer, aligns with the Lower part of Unit 3 (#3B and #3C). Notably, the top of the high-resistive layer does not coincide with that of the massive andesite (Unit 4) as typically expected. Various factors, especially water content, can cause a decrease in resistivity values (e.g. Park et al., 2016).

The observed correlations between resistivity and the massive andesite body below T3, T4 and T5 reveal striking discrepancies. In the case of T3, the top of the massive andesite encountered at a depth of approximately 20 m in the GP1 borehole corresponds to the bottom part of Layer-c or the upper part of Layer-d in the ERT sections, which are characterized by low resistivity. The absence of the high-resistive body beneath T5 is evident in the north-south cross sections of the ERT, indicating that Layer-c wedges out under T4 (Figure 10a, Figure SF.7).

Interestingly, the expected high-resistivity anomaly of the massive andesite is not visible in the ERT sections at T5. Instead, a moderate- to low-resistivity zone is observed from 5 m down to over 30 m. In contrast, during the GP5 drilling, the massive andesite was encountered at a depth of 30 m. We propose that this discrepancy is due to a hydrological anomaly where high-pressure artesian water from below has fully saturated the highly fractured andesite lava. This saturation has transformed the andesite into a conductive or low-resistivity layer, thus obscuring the anticipated high-resistivity anomaly in the ERT sections (Park et al., 2016). The water inflow observed during the GP1 drilling, specifically between 17 and 20 m deep within the weathered upper part of the massive andesite (Unit 3), supports this hypothesis. Additionally, the presence of a

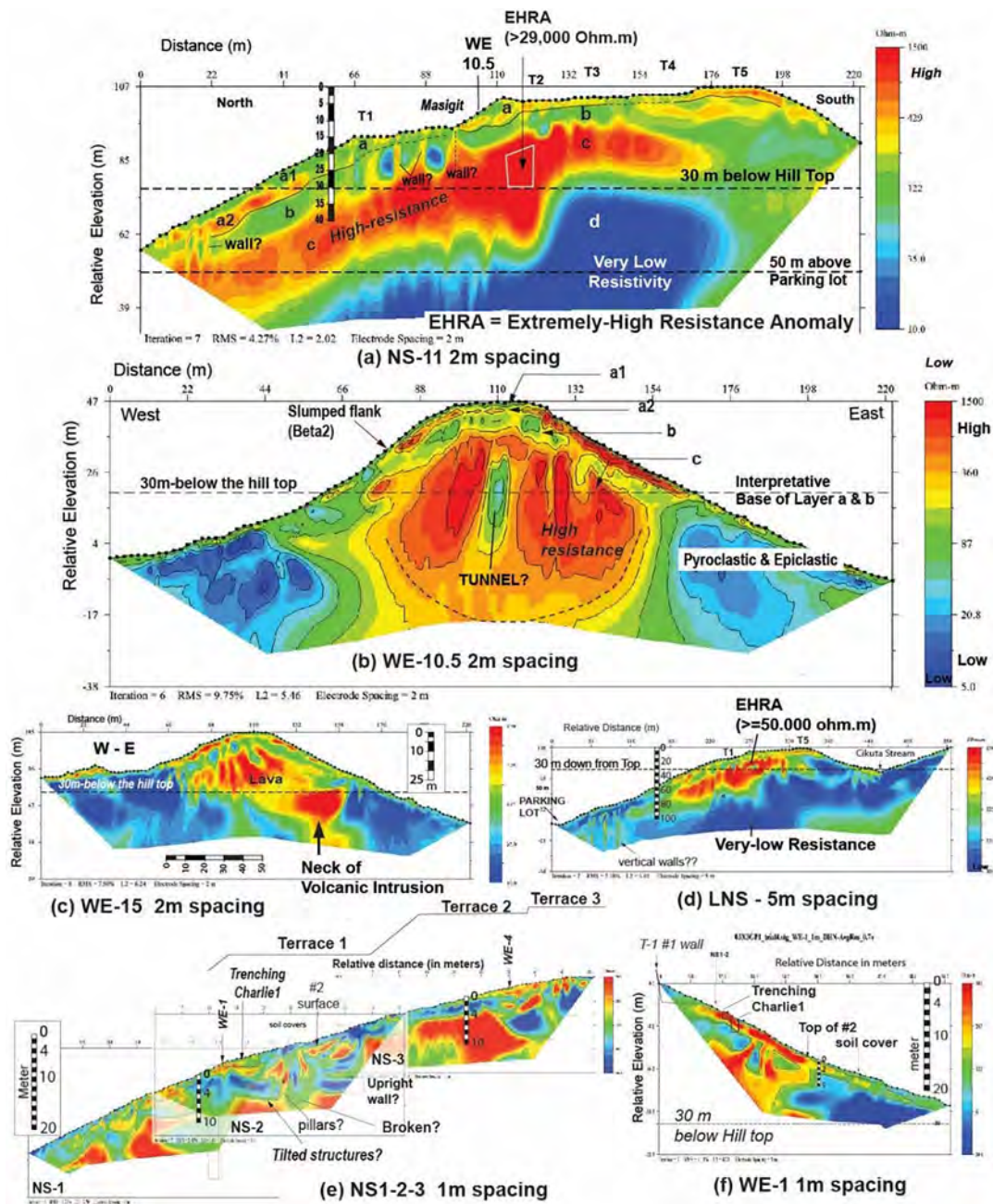


FIGURE 10 Summary of ERT prospecting. (a) Selected north–south longitudinal section with 2-m spacing electrodes, revealing resistivity-layer stratification and the presence of an extremely high resistive anomaly (EHRA) beneath T2. (b) Selected west–east section with 2-m spacing electrodes, illustrating the pyramidal shape of layers, the interpretative base of Layers a and b and a low-velocity zone in the centre, potentially indicating a soil-filled tunnel. (c) West–east section indicating the presence of neck volcanic intrusions of the massive andesite lava. (d) 2D line with 5-m spacing electrodes, providing an overview of the entire longitudinal section of Gunung Padang. (e) Combined profile of NS1, NS2 and NS3 survey lines on the east slope, parallel to the areas behind T-1, T-2 and T-3. (f) Examples of 1-m spacing ERT on the east slope, showcasing detailed subsurface structures. Complete datasets can be found in Figure SF. [Colour figure can be viewed at [wileyonlinelibrary.com](https://onlinelibrary.wiley.com)]

perennial ‘sacred’ water spring near the base of the megalithic stairway further underscores the unique hydrological conditions present. Further investigation is required to fully comprehend this hydrological anomaly.

The E-W ERT sections, utilizing 2-m-spacing electrode configurations, reveal the pyramidal shape of Layers a and b with symmetrical east and west flanks. These layers appear to be horizontally truncated

at a consistent elevation base, approximately 30 m below the top (Figure 10b, Figure SF.10). This base is interpreted as a possible construction foundation for Units 1, 2 and 3A, clearly visible in all E-W ERT sections and gradually rising 5 m southward towards T5 (Figure SF.10b–o). Moreover, The ERT sections also provide imagery suggestive of tunnels, including a central tunnel within the pyramid structure (Figure 10b). The high-resolution ERT surveys reveal roof-

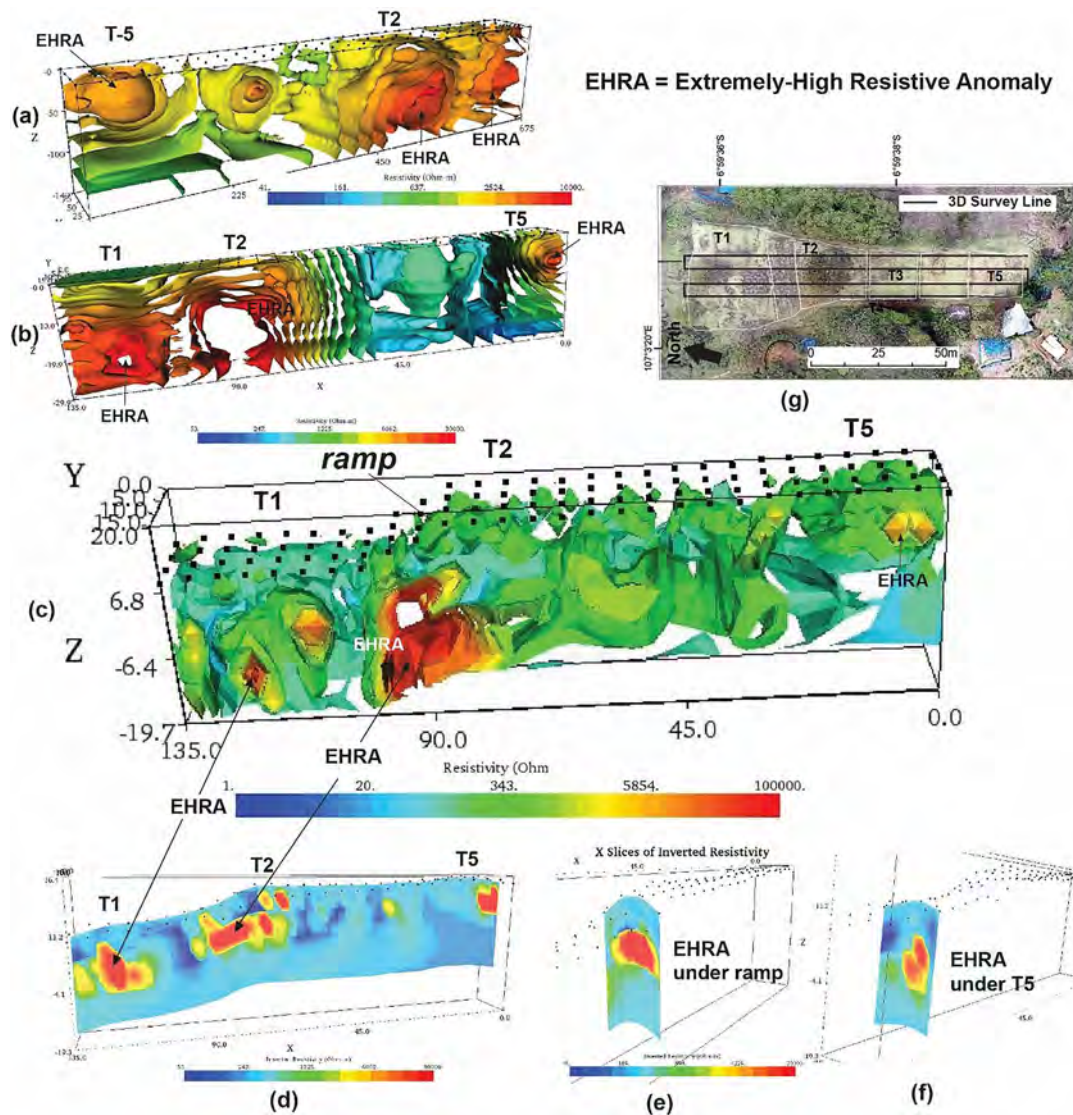


FIGURE 11 The underground chambers revealed by the extremely high-resistive anomaly (EHRA) in the 3D ERT survey. (a,b) 3D ERT imaging before topographic correction. (c) 3D ERT imaging after topographic correction. (d–f) Examples of 2D slices showcasing the EHRA and the corresponding underground chambers. (g) Index map illustrating the survey line of the 3D ERT survey. [Colour figure can be viewed at wileyonlinelibrary.com]

wall-and-floor-like shapes (Figure 10e,f). The presence of a long narrow passage is suggested (Figure 10f, Figure SF.13). The use of 2-m and 1-m grid spacing in the ERT survey provides further insights into the subsurface structure geometry. Beneath the high-resistive layer, notable large vertical structures are observed (Figure 10c, Figure SF.10h–k), interpreted as the neck of a volcanic intrusion that flowed northward along the pre-existing slope of the ancient extinct volcano. The extruded magma, characterized by its thick and viscous nature, rapidly solidified, forming a lava tongue. The most intriguing feature is the presence of extremely high resistance anomalies (EHRA), exceeding 20 000 $\Omega\cdot\text{m}$ and even reaching beyond 100 000 $\Omega\cdot\text{m}$. The most prominent EHRA is found beneath the ramp and T2 (Figure 10a, Figures SF.7, SF.8 and SF.11), providing solid evidence of a large cavity or chamber.

3.6.2 | 3D ERT survey prospecting underground chambers

To further investigate the extremely high-resistive anomaly (EHRA) identified in the 2D ERT sections, a 3D ERT survey was conducted, covering the entire expanse of the megalithic terraces on the hilltop. The survey employed 112 steel electrodes, strategically arranged in four parallel lines with a 5-m spacing between both electrodes and lines, resulting in a rectangular survey area measuring 15 × 135 m (Figure 11g). By conducting a 3D survey, we were able to gather data with significantly higher density compared to the 2D survey, as the 3D approach captured volumetric information rather than just a 2D section. Consequently, the acquisition time for the 3D survey was significantly longer, spanning the entirety of the day, in contrast to the

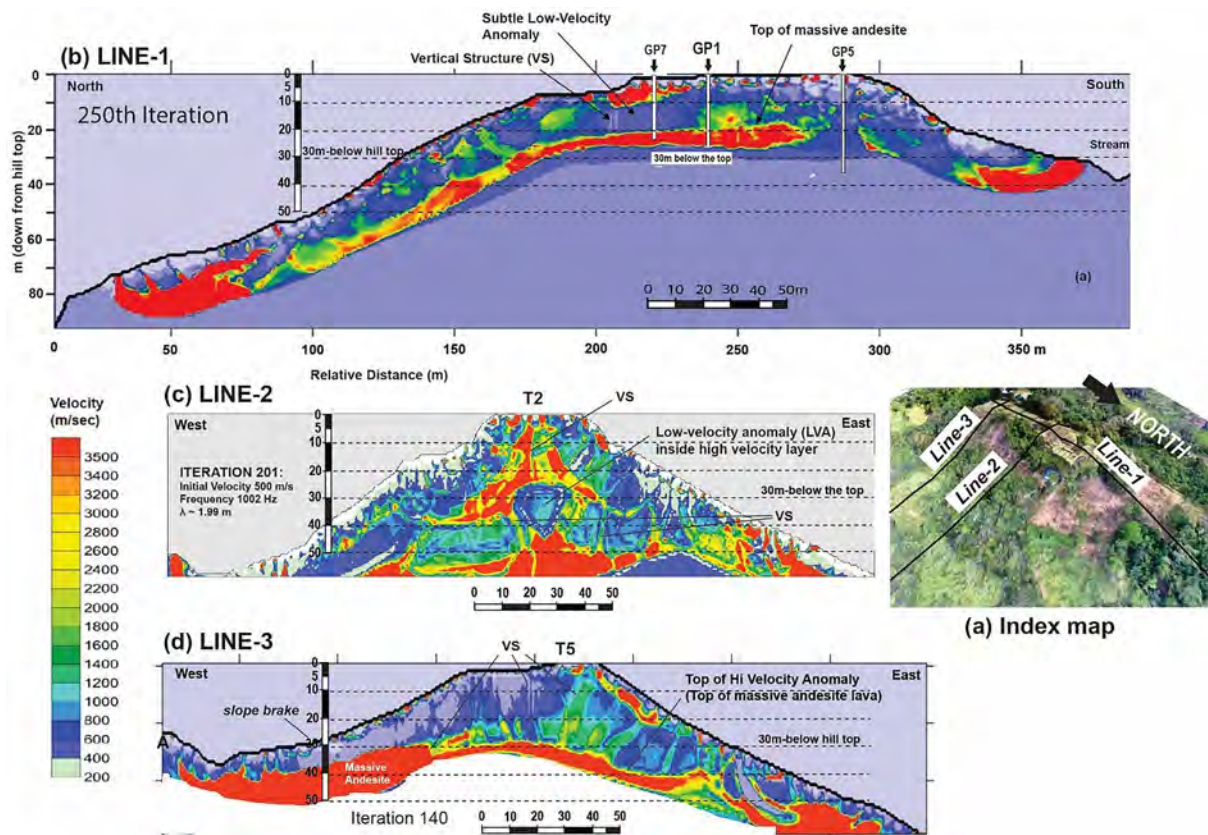


FIGURE 12 Seismic tomography (ST) prospecting. (a) Index map illustrating the ST survey lines. (b) Line-1: north-south longitudinal section passing through the megalithic site. (c) Line-2: east-west section crossing the centre of the site (crest of T2) and revealing a chamber through its low-seismic velocity anomaly (LVA) within the high-seismic velocity zone. (d) Line-3: east-west ST section crossing T5. The top of the high-velocity layer marks the boundary of the massive basaltic andesite. Numerous vertical structures are detected in the ST sections. [Colour figure can be viewed at [wileyonlinelibrary.com](https://onlinelibrary.wiley.com)]

relatively shorter duration of the 2D survey, which only took a few hours for a single run.

The results of the 3D survey provided successful visualization of the suspected large cavities in three dimensions, as depicted in Figure 10. Similar to the 2D imaging, these large cavities or chambers were distinguished by the EHRA but in 3D (Figure 11a-c). The presence of EHRA, accompanied by surrounding layers of low resistivity, clearly outlined the chambers. The main chamber beneath the ramp between T1 and T2 was estimated to have dimensions of approximately $10 \times 10 \times 15$ m (width \times height \times length). Moreover, EHRA was also observed beneath T1 and T5, further supporting the presence of additional chambers (Figure 11c-f).

3.7 | Results of ST survey

We conducted three survey lines (Figure 12a). The initial purpose of the ST survey is to further investigate the large cavities the ERT imaged. However, the results also revealed other significant findings. The ST sections exhibited stratifications that correlated with the ERT and GPR imaging. The upper layer displayed a low velocity measuring below 400 m/s. The intermediate layer exhibited a background velocity

ranging from approximately 400 to 800 m/s, with occasional higher velocity zones (1000–2000 m/s). Finally, the bottom layer constituted a high-velocity layer, measuring above 2000 m/s. Regarding lithology correlations, the upper layer aligns with Units 1 and 2. The intermediate layer corresponds to Unit 3, and the high-velocity layer at the bottom matches Unit 4, which is the massive andesite lava (Figure 13).

The ST Line-1 provides a clear N-S cross-sectional view of the pyramid mound (Figure 12b, Figure SG.3). It reveals a subtle low-velocity anomaly (LVA) situated between the upper and lower high-velocity layers. The LVA is bounded by two vertical strips of low-velocity media, resembling an entrance gate. Line-2, the west-east survey line passing through the centre (T2), exhibits a distinct contrast with an LVA surrounded by high-velocity materials (Figure 12c, Figure SG.4). It may also indicate possible large tunnels. This LVA corresponds to a location similar to the prominent EHRA observed in the 2D and 3D ERT surveys. All lines of source-receiver configurations are adequate to capture the objects of interest. Specifically, for Line-2 and Line-3, the aperture angles of the configurations are sufficiently large, enabling effective imaging of the targeted LVA within the high-velocity Layer.

The top of the high-velocity layer sharply defines the surface of the massive andesite, which lies at an approximate depth of 17 m

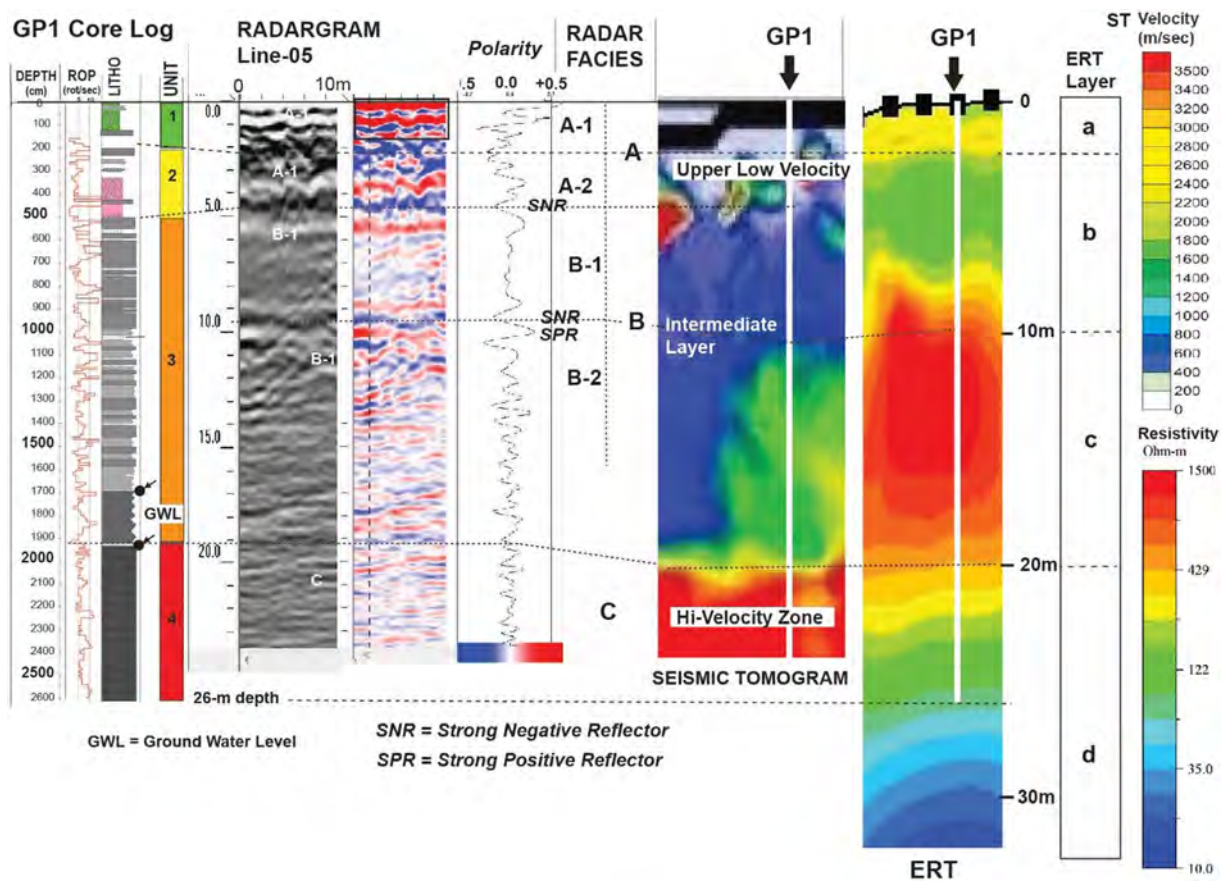


FIGURE 13 Data correlations of borehole log–ground-penetrating radar (GPR)–seismic tomogram (ST)–electric resistivity tomogram (ERT). The core log is obtained from GP1. The radargram is taken from Line-05 in close proximity. The ST profile is derived from Line-1 (Figure 12b), and the ERT profile is based on Line NS-11 (Figure 10a). Unit 1 and Unit 2 are correlated with Radar Facies A and ST’s upper low-seismic layer. Unit 3 is correlated with Radar Facies B and ST’s intermediate-velocity layer. Unit 4 is correlated with Radar Facies C and ST’s high-velocity anomaly (LVA). The top of ERT’s high-resistive anomaly (Layer-c) is aligned with the top of Unit 3’s lower part (#3B and #3C) and the top of Facies B-2. [Colour figure can be viewed at wileyonlinelibrary.com]

below T1, 20 m below T2 and T3, as revealed by Line-1 (Figures 12a and 13), and at 30 m depth below T5, as shown by Line-3 (Figure 12c, Figure SG.5). Another prominent feature in ST sections is the presence of multiple vertical structures, including the two stripes bounding the LVA in Line-1. These features are not artefacts resulting from processing, noises or interferences but represent subsurface features that likely possess vertical boundaries of density contrasts. Therefore, these vertical structures may correspond to walls or columns of the constructions. Similar vertical features are also frequently observed in the ERT sections, and upright features are visible as the rock pillars on the Beta2 scarp and the steep rock wall in the Echo2 trench.

3.8 | Integrating data

This study demonstrates the effective utilization and integration of multiple techniques to explore the complex, multi-layered and extensive ancient constructions at Gunung Padang. The combination of

surface observations, trenching, core drillings and geophysical surveys, including GPR, ERT and ST, has not only confirmed but also complemented each other, providing a comprehensive understanding of the site. The multi-layered nature of the constructions aligns well with the profiles of GPR facies, the layering identified in ERT and the stratifications revealed by ST (Figure 13), strengthening the overall interpretation.

Specifically, Unit 1 and Unit 2 correspond to GPR Facies A1 and A2, reflected in the upper low-velocity layers observed in ST and roughly correlate with Layers a and b in the ERT sections. The presence of Unit 3 is strongly supported by GPR Facies B, the intermediate seismic velocity layer and Layers b and c in ERT. Remarkably, the top of Unit 3B, located at a depth of approximately 9–11 m, closely aligns with the top of GPR Facies B2 and the top of the high-resistivity Layer c in ERT. Unit 4, composed of massive basaltic andesite, strongly correlates with the high-seismic velocity layer observed in ST and the GPR Facies C. The top of the high-seismic velocity layer accurately reflects the top of Unit 4, further validating its presence and characteristics.

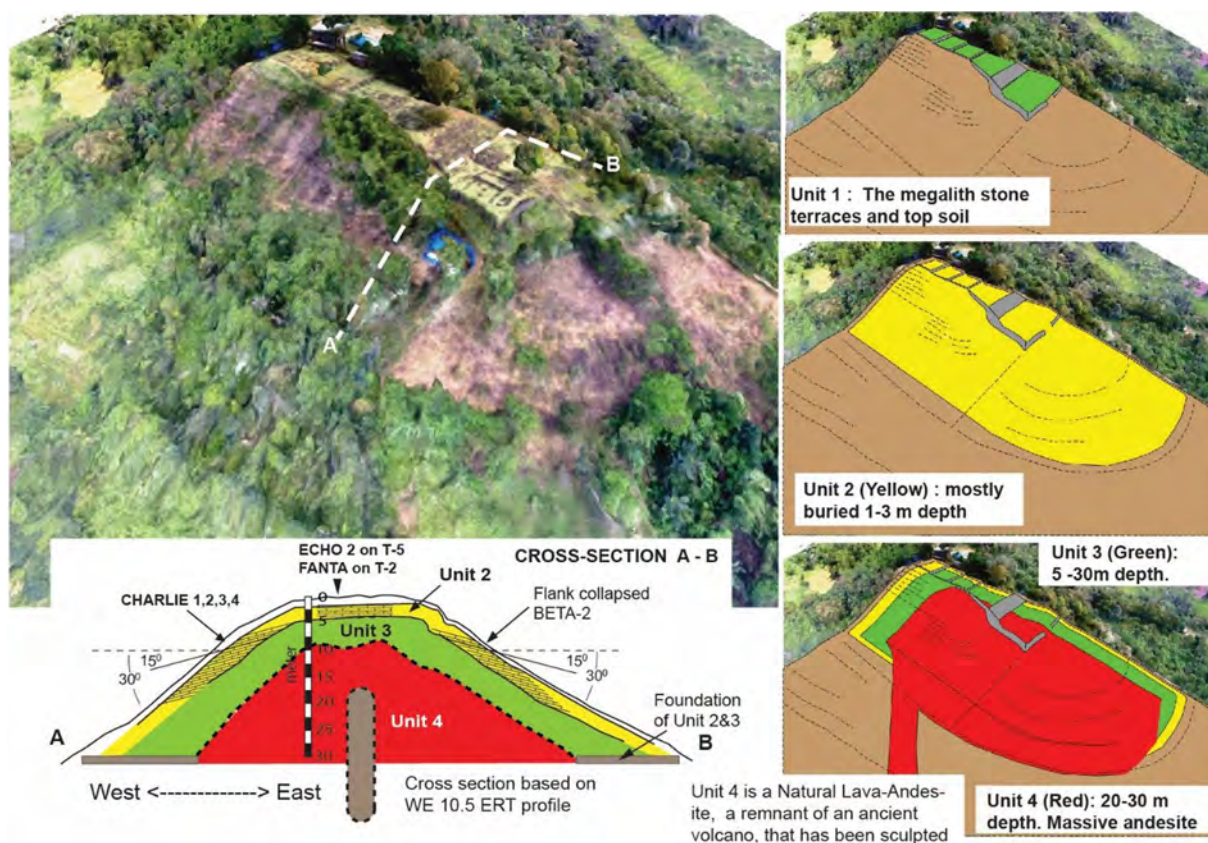


FIGURE 14 Simplified reconstruction of Gunung Padang. Unit 1 represents the surficial stone terraces constructed between 2000 and 1100 BCE or more recently. Unit 2 (highlighted in yellow) corresponds to a buried pyramidal-shaped layer composed of columnar rocks and was built around 6000–5500 BCE. Unit 3 (shown in green) dates back to 25 000–14 000 BCE. Unit 4 represents the sculpted massive basaltic-andesite lava. [Colour figure can be viewed at [wileyonlinelibrary.com](https://onlinelibrary.wiley.com/doi/10.1002/arp.1912)]

3.9 | Uncertainty of geophysical measurements

The geophysical measurements conducted at Gunung Padang provide valuable insights into the subsurface structures and ancient constructions. However, it is crucial to acknowledge the inherent uncertainties associated with the measurements. Complex 3D features, groundwater levels, moisture content and equipment limitations can introduce uncertainties in interpreting geophysical subsurface structures and predicting their depths. For example, this study demonstrates that the geophysical layers do not necessarily align with the lithological stratigraphy as depicted from borehole data. The discrepancies highlight the need for caution when interpreting the results and emphasize the importance of considering multiple factors and approaches in the analysis.

Additionally, 2D acquisition methods, compared to 3D, can introduce limitations in interpreting geophysical data. 2D surveys provide valuable insights into the subsurface but represent a simplified representation of the complex 3D subsurface structures, leading to ambiguities in the characterization of subsurface features. The adoption of 3D survey and 2.5 D (2D on gridded lines) surveys, as conducted in this study, offers a better representation of the subsurface, reducing some of the uncertainties associated with 2D acquisition.

The GPR survey in this study employed a simplified approach by assuming a single average electromagnetic (EM) velocity for all subsurface layers due to the limitations of the software. This assumption introduces uncertainties in accurately characterizing and distinguishing subsurface features and boundaries based solely on the GPR data. Using a single average EM velocity also limits the resolution and accuracy of the imaging results. More sophisticated approaches are required to capture the complexity of subsurface structures.

The ERT method is also subject to uncertainties, particularly in interpreting resistivity data. The relationship between resistivity and subsurface properties is complex, influenced by various factors as described above. Assumptions made during inversion algorithms and the homogeneity of subsurface properties can also introduce uncertainties in accurately characterizing subsurface structures based on resistivity values. As observed in this study, the absence of a high-resistive layer of the massive basaltic andesite body beneath certain areas exemplifies the challenges in accurately interpreting resistivity data.

Although powerful for subsurface imaging, the ST method is also associated with uncertainties. The inherent complexity of the subsurface, such as variations in lithology, fluid content and fractures, can introduce challenges in accurately estimating seismic velocities and

imaging subsurface structures. Factors such as sensor coverage, frequency and quality of seismic waves and assumptions made in inversion algorithms further contribute to uncertainties in the derived velocity models.

As demonstrated in this study, integrating multiple geophysical methods in a comprehensive survey helps mitigate the uncertainties associated with individual techniques. By comparing and confirming the results from different methods, the accuracy and certainty of the interpretations are enhanced. This comprehensive approach and integration of geophysical methods contribute to a more robust understanding of the subsurface structures, minimizing uncertainties and providing a reliable basis for further analysis. Finally, it is important to note that the borehole core logs and trenching data are superior for calibrating the subsurface geophysical interpretation, adding further confidence to the findings.

4 | CONCLUSION

4.1 | Gunung Padang is a multi-layered prehistoric pyramid

This study strongly suggests that Gunung Padang is not a natural hill but a pyramid-like construction. The pyramid's core consists of meticulously sculpted massive andesite lava (Unit 4), enveloped by layers of rock constructions (Unit 3, Unit 2 and Unit 1). The carbon dating analysis further supports the multi-layer construction's long history, spanning successive periods.

The oldest construction, Unit 4, likely originated as a natural lava hill before being sculpted and then architecturally enveloped during the last glacial period between 25 000 and 14 000 BCE. (Figure 14). Afterward, Gunung Padang was abandoned by the first builders for thousands of years, leading to significant weathering. Around 7900–6100 BCE, Unit 3 was deliberately buried with substantial soil fills. Approximately a millennium later, between 6000 and 5500 BCE, a subsequent builder arrived at Gunung Padang and constructed Unit 2. Lastly, the final builder arrived between 2000 and 1100 BCE, constructing Unit 1.

It is intriguing to note that during the construction of Unit 1, Unit 2 likely remained relatively intact and well preserved. However, in a peculiar turn of events, Unit 2 was subsequently buried, possibly to conceal its true identity for preservation purposes. As a result, Unit 2 now lies concealed beneath Unit 1, which comprises simple superficial stone terraces or *punden berundak* representing the latest visible manifestation of Gunung Padang.

4.2 | Concluding remarks and further studies

This study sheds light on advanced masonry skills dating back to the last glacial period. This finding challenges the conventional belief that human civilization and the development of advanced construction techniques emerged only during the warm period of the early

Holocene or the beginning of the Neolithic, with the advent of agriculture approximately 11 000 years ago (Harari, 2014). However, evidence from Gunung Padang and other sites, such as Gobekli Tepe, suggests that advanced construction practices were already present when agriculture had, perhaps, not yet been invented.

The builders of Unit 3 and Unit 2 at Gunung Padang must have possessed remarkable masonry capabilities, which do not align with the traditional hunter-gatherer cultures. The burial of these structures around 9000 years ago adds further intrigue for reasons not fully understood. Given the long and continuous occupation of Gunung Padang, it is reasonable to speculate that this site held significant importance, attracting ancient people to repeatedly occupy and modify it.

To further advance our knowledge of Gunung Padang, it is essential for future research to undertake comprehensive and systematic excavations that delve into the characteristics of Unit 2, Unit 3 and Unit 4, as well as their cultural significance. Employing advanced geophysical imaging techniques and directional drilling can prove instrumental in exploring underground structures, including potential chambers. In the event of encountering a chamber during drilling operations, the use of downhole cameras can provide valuable visual documentation. Furthermore, conducting more extensive radiometric dating studies will contribute to obtaining precise age estimates for the constructions, enhancing our understanding of their historical timelines.

Gunung Padang stands as a remarkable testament, potentially being the oldest pyramid in the world. Further investigation and interdisciplinary research will uncover its hidden secrets and shed more light on the ancient civilizations that thrived in this enigmatic site.

ACKNOWLEDGEMENTS

We sincerely thank the individuals and organizations who have made this study possible. Special thanks go to Mr. Andi Arief for his unwavering support and encouragement throughout the research. We are also grateful to General Army Dr. Soesilo Bambang Yudhoyono, former President of Indonesia (2004–2014), as well as Gen. Gatot Nurmantyo, Admiral Dr. Ade Sopandi, Mr. Dedy Mizwar (former Vice Governor of West Java) and Prof M. Nuh (former Ministry of Education and Culture) for their valuable supports. We extend our appreciation to GDA (Geosains Delta Andalan) Consulting, the Rock Fluids Imaging Lab, the drone-photography team of the University of Pasundan, Aero-Geosurvey and Zona-Spasia Co. for their assistance and support throughout the project. Our heartfelt thanks also go to the dedicated field crews and local residents whose enthusiasm and cooperation were instrumental in the success of this study. We acknowledge Mr Graham Hancock for kindly proofreading the manuscript and his team for shedding light on Gunung Padang in Netflix's *Ancient Apocalypse*. We are also indebted to Mr Peter Lanzarone for his thorough review and valuable suggestions that significantly improved the manuscript. Additionally, we would like to thank all our friends and countless others who have provided support and assistance throughout this research. This research received no specific grant from government, public, commercial or not-for-profit funding

agencies. Finally, the Competitive RISPRO Program of the Indonesia Endowment Funds for Education (LPDP) of the Ministry of Finance, granted to Dr. Bagus E. B. Nurhandoko for his research in developing the subsurface imaging equipments, supported the publication.

CONFLICT OF INTEREST STATEMENT

The authors declare no conflict of interest.

DATA AVAILABILITY STATEMENT

The data that supports the findings of this study are available in the supplementary material of this article.

ORCID

Danny Hilman Natawidjaja  <https://orcid.org/0000-0002-3870-9184>

REFERENCES

- Akbar, A. (2013). *Situs Gunung Padang: Misteri dan Arkeologi (Gunung Padang site: Mystery and archeology)*. Change Publication. 266 p.
- Bingham, H. (1930). *Machu Pichu, a citadel of Incas*. Yale University Press. 244 p.
- Bintarti, D. D. (1982). *Punden berundak di Gunung Padang*. Berkala Arkeologi, Pusat Penelitian Arkeologi Nasional.
- Bronk Ramsey, C. (2016). Development of the radiocarbon calibration program. *Radiocarbon*, 43(2A), 355–363. <https://doi.org/10.1017/S0033822200038212>
- Ékes, C., & Hickin, E. J. (2001). Ground penetrating radar facies of the paraglacial Cheekye fan, southwestern British Columbia, Canada. *Sedimentary Geology*, 143(3), 199–217. [https://doi.org/10.1016/S0037-0738\(01\)00059-8](https://doi.org/10.1016/S0037-0738(01)00059-8)
- Forte, E., & Pipan, M. (2008). Integrated seismic tomography and ground-penetrating radar (GPR) for the high-resolution study of burial mounds (tumuli). *Journal of Archaeological Science*, 35(9), 2614–2623. <https://doi.org/10.1016/j.jas.2008.04.024>
- Harari, Y. N. (2014). *Sapiens: A brief history of humankind* (p. 498). London, Vintage Book.
- Irsyam, M., Cummins, P. R., Asrurifak, M., Faizal, L., Natawidjaja, D. H., Widiyantoro, S., Meilano, I., Triyoso, W., Rudiyanto, A., Hidayati, S., Ridwan, M., Hanifa, N. R., & Syahbana, A. J. (2020). Development of the 2017 national seismic hazard maps of Indonesia. *Earthquake Spectra*, 36, 112–136. <https://doi.org/10.1177/8755293020951206>
- Kim, B.-M. (1982). *Megalithic cultures in Asia*. Hanyang University Press. 204 p.
- Krom, N. J. (1915). *Rapporten van den Oudheidkundigen dients in Nederlandsch 1914*.
- Lanzarone, P., Seidel, M., Brandt, S., Garrison, E., & Fisher, E. C. (2019). Ground-penetrating radar and electrical resistivity tomography reveal a deep stratigraphic sequence at Mochena Borago Rockshelter, southwestern Ethiopia. *Journal of Archaeological Science: Reports*, 26, 101915. <https://doi.org/10.1016/j.jasrep.2019.101915>
- Lee, K., Zeng, X., McMechan, G. A., Howell, C. D. Jr., Bhattacharya, J. P., Marcy, F., & Olariu, C. (2005). A ground-penetrating radar survey of a delta-front reservoir analog in the Wall Creek member, frontier formation, Wyoming. *AAPG Bulletin*, 89(9), 1139–1155. <https://doi.org/10.1306/042705040106>
- Marliyani, G. I., Arrowsmith, J. R., & Whipple, K. X. (2016). Characterization of slow slip rate faults in humid areas: Cimandiri fault zone, Indonesia. *Journal of Geophysical Research - Earth Surface*, 121(12), 2287–2308. <https://doi.org/10.1002/2016JF003846>
- McCoy, M. D., Alderson, H. A., Hemi, R., Cheng, H., & Edwards, R. L. (2016). Earliest direct evidence of monument building at the archaeological site of Nan Madol (Pohnpei, Micronesia) identified using ²³⁰Th/U coral dating and geochemical sourcing of megalithic architectural stone. *Quaternary Research*, 86(3), 295–303. <https://doi.org/10.1016/j.yqres.2016.08.002>
- McCoy, M. D., & Athens, J. S. (2012). Sourcing the megalithic stones of Nan Madol: An XRF study of architectural basalt stone from Pohnpei, Federated States of Micronesia. *Journal of Pacific Archeology*, 3(1), 105–114.
- Natawidjaja, D. H. (2015). *Piramid Gunung Padang: Bukti peradaban Sundaland dari Zaman Es? (Gunung Padang pyramid: Evidence of Sundaland civilization in the Ice Age), Mitos dan Bencana di Nusantara (Myth of Dissasters in Nusantara): Yogyakarta*. A paper was presented in the Meeting of “Borobudur Writer and Cultural Festival”, 17 November 2015, Ombak Dua (www.penerbitombak.com).
- Natawidjaja, D. H., Bachtiar, A., Endar, B., Daryono, M., & Subandrio, A. (2018). Evidence of large pyramid-like structure predating 10,000 year BP at Mount Padang, West Java, Indonesia: Applications of geological-geophysical methods to explore buried man-made structures. In *Proceedings American Geophysical Union Fall Meeting, Washington DC, 2018, Proceeding AGU EOS Transaction*. <https://www.essoar.org/doi/abs/10.1002/essoar.10500119.1>
- Natawidjaja, D. H., Bachtiar, A., Endar, B., & Subandrio, A. (2016). Archeological and geophysical studies of the Gunung Padang megalith in Cianjur, Indonesia implies lost advanced civilizations in Sundaland before Holocene. *GEOSEA XIV Congress and 45th IAGI Annual Convention 2016*: Bandung, IAGI.
- Natawidjaja, D. H., Bradley, K., Daryono, M. R., Aribowo, S., & Herrin, J. S. (2017). Late Quaternary eruption of the Ranau caldera and new geological slip rates of the Sumatran fault zone in southern Sumatra, Indonesia. *Geoscience Letters*, 4(21), 21. <https://doi.org/10.1186/s40562-017-0087-2>
- Nurhandoko, B. E., & Ashida, Y. (1998). Fresnel zone wavepath tomography - Theory. In *Proceedings The 3rd International Symposium on Recent Advances in Exploration Geophysics (RAEG 1998)*, Kyoto, Japan.
- Nurhandoko, B. E. B. (2000). *Fresnel Zone Seismic Tomography [Dr-Eng Disertation]*: Kyoto University.
- Nurhandoko, B. E. B. (2016). Imaging subsurface fracture and void using wide-band inversion of Fresnel interpolated Wavepath seismic tomography. *Indonesian Journal of Physics*, 20(3), 71–74.
- Nurhandoko, B. E. B., Ambia, F., Triyoso, K., Choliq, M. T., Budi, M. L., Suhendi, A., & Abdianto, W. E. (2016). Marine seismic tomography for detecting fracture and void of subsurface seabed: A theoretical framework development and application of wide-band Fresnel tomography. *Indonesian Journal of Physics*, 19(4), 103–110. <https://doi.org/10.5614/itb.i.jp.2008.19.4.2>
- Nurhandoko, B. E. B., Matsuoka, T., Watanabe, T., & Ashida, Y. (1999). Land seismic refraction tomography using homogeneous velocity as initial model. *SEG Technical Program Expanded Abstracts 1999, Society of Exploration Geophysicists*, p. 1481–1484.
- Papadopoulos, N. G., Yi, M.-J., Kim, J.-H., Tsourlos, P., & Tsokas, G. N. (2010). Geophysical investigation of tumuli by means of surface 3D electrical resistivity tomography. *Journal of Applied Geophysics*, 70(3), 192–205. <https://doi.org/10.1016/j.jappgeo.2009.12.001>
- Park, S., Shin, S., Lee, D. K., Kim, C. R., & Son, J.-S. (2016). Relationship between electrical resistivity and physical properties of rocks. *Near Surface Geoscience 2016 - First Conference on Geophysics for Mineral Exploration and Mining, Volume 2016, European Association of Geoscientist & Engineer*, p. 1–5.
- Purwanto, H., Tirtasari, C. P., & Sumerata, I. W. (2017). Candi Kethek: Karakter dan Latar Belakang Agama (in Indonesian). *Forum Arkeologi*, 30(2), 101–112. <https://doi.org/10.24832/fa.v30i2.226>
- Ramadina, S. P. (2010). Analisis perupaian situs megalitik Gunung Padang di Cianjur, Jawa Barat. *J.Vis.Art & des. ITB*, 4(1), 51–66. <https://doi.org/10.5614/itbj.vad.2013.4.1.7>

- Ramsey, B. (2007). OxCal program. <https://c14.arch.ox.ac.uk/oxcal.html>, Radiocarbon Accelerator Unit, University of Oxford.
- Sarris, A., Dunn, R. K., Rife, J. L., Papadopoulos, N., Kokkinou, E., & Mundigler, C. (2007). Geological and geophysical investigations in the Roman cemetery at Kenchreai (Korinthia), Greece. *Archaeological Prospection*, 14(1), 1–23. <https://doi.org/10.1002/arp.280>
- Sathiamurthy, E., & Voris, H. K. (2006). Maps of Holocene sea level transgression and submerged lakes on the Sunda shelf. *The Natural History Journal of Chulalongkorn University, Supplement 2*, 1–44.
- Shi, Z., Yu, T., & Shi, M. (2020). Investigate the layout and age of a large-scale mausoleum in Hangzhou, China using combined geophysical technologies and archaeological documents. *Archaeological Prospection*, 27(4), 301–313. <https://doi.org/10.1002/arp.1774>
- Soeria-Atmadja, R., Maury, R. C., Bellon, H., Pringgoprawiro, H., Polve, M., & Priadi, B. (1994). Tertiary magmatic belts in Java. *Journal of Southeast Asian Earth Sciences*, 9(1), 13–27. [https://doi.org/10.1016/0743-9547\(94\)90062-0](https://doi.org/10.1016/0743-9547(94)90062-0)
- Sudjatmiko (1972). Peta Geologi Lembar Cianjur, Jawa Barat (Geological Map of the Cianjur Quadrangle, West Java), 1:100 000 scale. Pusat Penelitian dan Pengembangan Geologi, ESDM (the Ministry of Energy and Natural Resources).
- Sukendar, H. (1985). *Tinggalan tradisi megalitik di daerah Cianjur*. Laporan Pusat Penelitian Arkeologi Nasional.
- Takashi, S. (2014). The monumental origin of Borobudur - a study for buildings in the relief panels. *Journal of Southeast Asian Archeology*, 34, 31–46.
- Tejero-Andrade, A., Argote-Espino, D. L., Cifuentes-Nava, G., Hernández-Quintero, E., Chávez, R. E., & García-Serrano, A. (2018). 'Illuminating' the interior of Kukulkan's pyramid, Chichén Itzá, Mexico, by means of a non-conventional ERT geophysical survey. *Journal of Archaeological Science*, 90, 1–11. <https://doi.org/10.1016/j.jas.2017.12.006>
- Tim-Peneliti (2003). *Laporan hasil penelitian arkeologi di Situs Megalitik Gunung Padang*. Balai Arkeologi Bandung.
- Tsokas, G. N., Giannopoulos, A., Tsourlos, P., Vargemezis, G., Tealby, J. M., Sarris, A., Papazachos, C. B., & Savopoulou, T. (1994). A large scale geophysical survey in the archaeological site of Europos (northern Greece). *Journal of Applied Geophysics*, 32(1), 85–98. [https://doi.org/10.1016/0926-9851\(94\)90011-6](https://doi.org/10.1016/0926-9851(94)90011-6)
- Vasco, D. W., Peterson, J. E., & Majer, E. L. (1995). Beyond ray tomography: Wavepaths and Fresnel volumes. *Geophysics*, 60(6), 1790–1804. <https://doi.org/10.1190/1.1443912>
- Veeerbek, R. D. M. (1896). *Geologische beschrijving van Java en Madoera*. Deel I en II.
- Voris, H. K. (2000). Maps of Pleistocene Sea levels in Southeast Asia: Shorelines, river systems, and time durations. *Journal of Biogeography*, 27, 1153–1167. <https://doi.org/10.1046/j.1365-2699.2000.00489.x>
- Yondri, L. (2017). *Situs Gunung Padang: Kebudayaan, manusia, dan lingkungan (Gunung Padang Site: Culture, human, and environment)* (p. 337). PT Semiotika.

SUPPORTING INFORMATION

Additional supporting information can be found online in the Supporting Information section at the end of this article.

How to cite this article: Natawidjaja, D. H., Bachtiar, A., Nurhandoko, B. E. B., Akbar, A., Purajatnika, P., Daryono, M. R., Wardhana, D. D., Subandriyo, A. S., Krisyuniyanto, A., Tagyuddin, Ontowiryo, B., & Maulana, Y. (2023). Geo-archaeological prospecting of Gunung Padang buried prehistoric pyramid in West Java, Indonesia. *Archaeological Prospection*, 1–25. <https://doi.org/10.1002/arp.1912>

Natawidjaja et al (2023, Archaeological Prospecting) – Supplementary Materials/Figures.

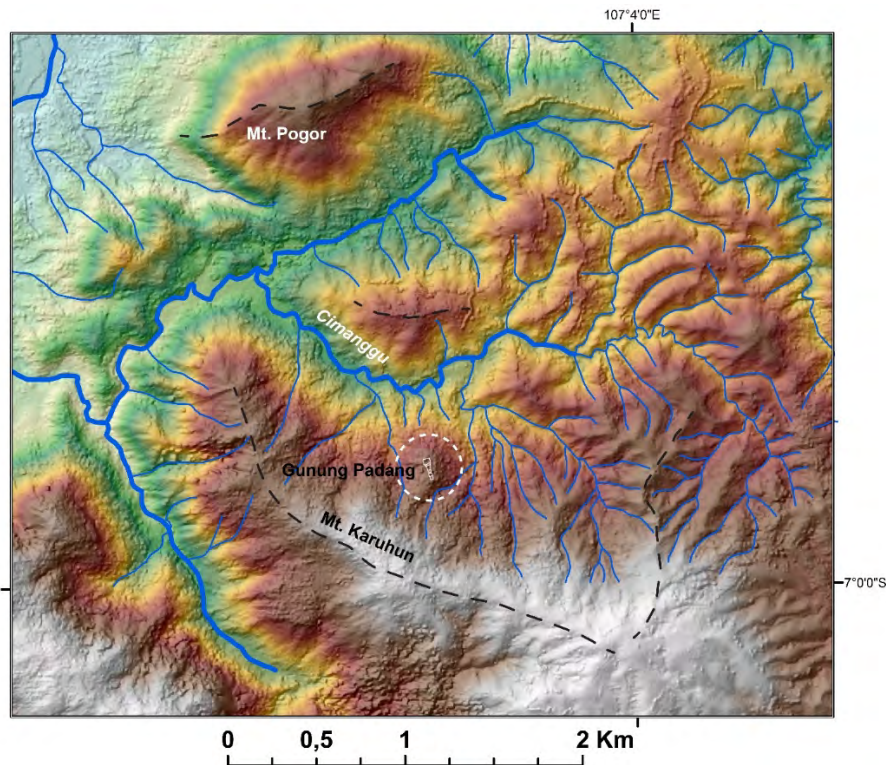
<https://...>

Geo-archaeological prospecting of Gunung Padang buried prehistoric pyramid in West Java, Indonesia

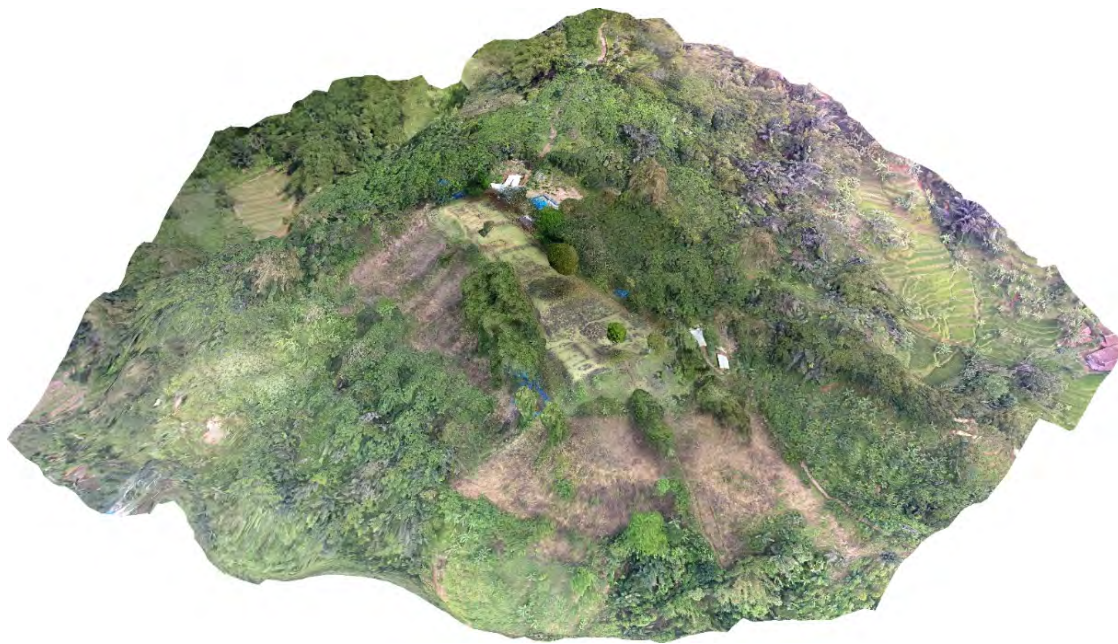
Danny Hilman Natawidjaja, Andang Bachtiar, Bagus Endar B. Nurhandoko, Ali Akbar, Pon Purajatnika, Mudrik R. Daryono, Dadan D. Wardhana, Andri S. Subandriyo, Andi Krisyuniyanto, Tagyuddin, Budianto Ontowiryo, Yusuf Maulana

Contents	Pages
SUPPLEMENTARY FIGURE – A. Site Maps	1 - 2
SUPPLEMENTARY FIGURE – B. Geo-Archaeological Trenching	3 - 10
SUPPLEMENTARY FIGURE – C. Core Drilling	11 – 16
SUPPLEMENTARY FIGURE – D. Radiocarbon Dating Analysis	17 – 24
SUPPLEMENTARY FIGURE – E. Ground Penetrating Radar	25 – 33
SUPPLEMENTARY FIGURE – F. Electrical Resistivity Tomography	34 – 47
SUPPLEMENTARY FIGURE – G. Seismic Tomography	48 – 56
SUPPLEMENTARY FIGURE – H. Data Integration and Analysis	57 – 60
SUPPLEMENTARY FIGURE – I. Gunung Padang Stone Artefacts	61 – 63
SUPPLEMENTARY FIGURE – J. Selected Petrography Analysis	64 – 69
SUPPLEMENTARY FIGURE – J. Imaginary Architectures	70 – 71
SUPPLEMENTARY FIGURE – L. Selected Photos of Events and People	72 - 74

SUPPLEMENTARY FIGURE – A. Site Maps



Sup.Figure A.1. Digital Surface Map of IFSAR –5m grid. Gunung Padang is a small hill in front of the higher Gunung Karuhun U-shape hill ridge.



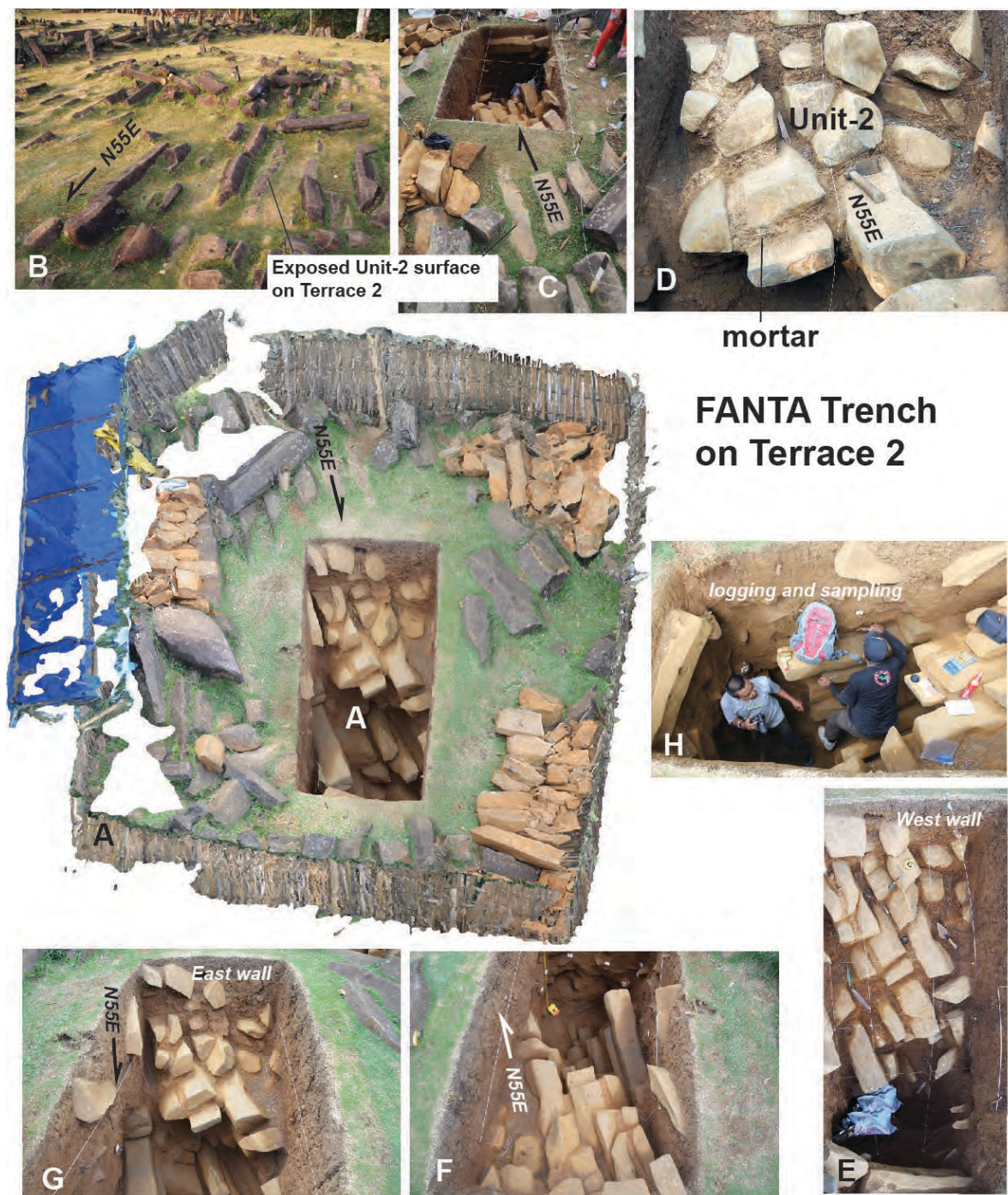
Sup.Figure A.2. The 3D Orthophoto of Gunung Padang, created from the drone-photos in 2014 with the Photography Team of the University of Pasundan, Bandung, Indonesia.



Sup. Figure A.3. Thematic Maps: (a) The Orthophoto developed from the drone survey in 2014 in collaboration with the Photographic Team of the University of Pasundan, Bandung, West Java. Contour elevations are from the geodetic survey; (b) Drone Orthophoto developed the Aero Geosurvey Surveying Co in 2019; (c) Orthophoto map, developed from by Zona Spasial Co in 2020.

SUPPLEMENTARY FIGURE – B. GEO-ARCHEOLOGICAL TRENCHING

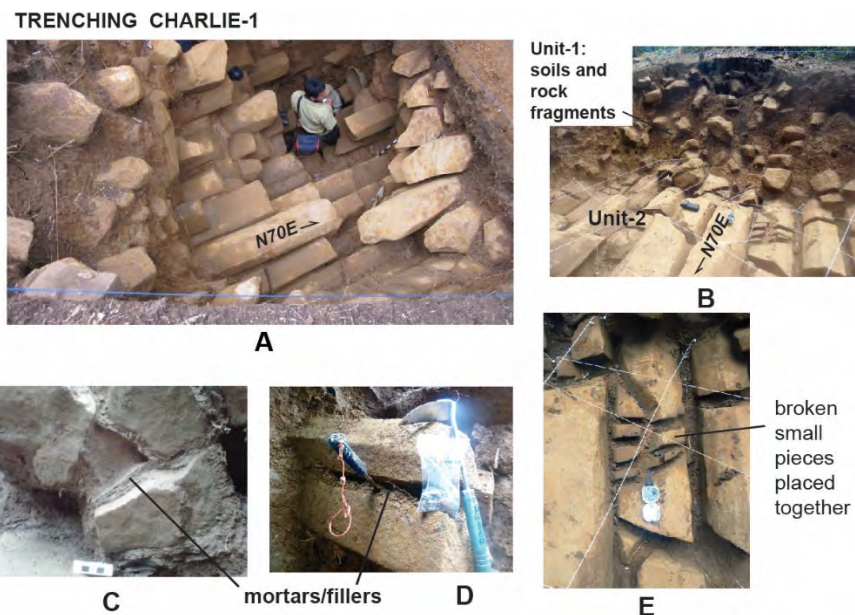
Sup.Figure B.1. Trenching Tango at Terrace 1 for a display of buried Unit 2 during the Indonesian President's visit in 2014. This trench had been previously opened by ARKENAS (National Archeological Institute) in 2005, but the revealed rock layer has been thought to be natural rocks.



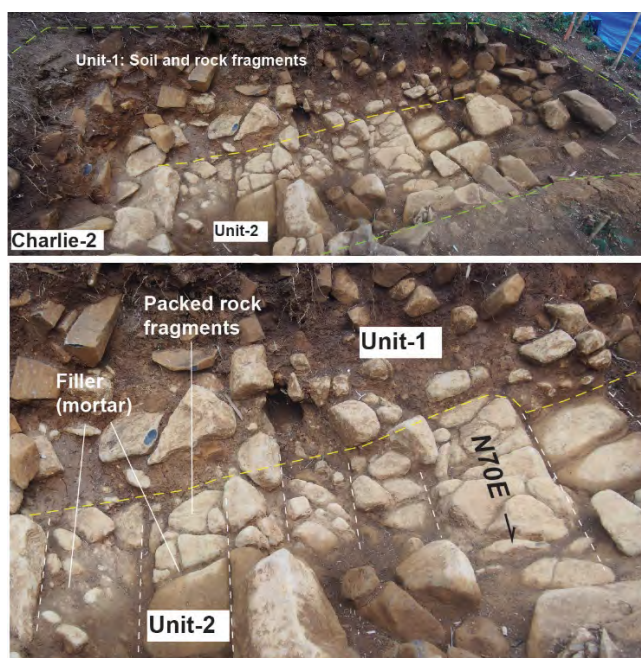
Sup. Figure B.2. Fanta trench on Terrace-2. A. Showing underground stacks of columnar basaltic andesite rocks oriented N55°E (Unit 2); B. Top of Unit 2 is exposed as the floor of Terrace-2 and Terrace-3; C. Showing that the columnar rock alignment on the surface continues underground; D. Relatively fresh Columnar rocks are surrounded by clay-silt-sand mortar; E. Fanta Trench was dug down to 3.5 m depth but still had not reached the bottom of Unit 2; F. Planview of the columnar rocks. Columnar rocks are cut laterally about 1-2m in average; E-F-G. Exposures from different angles.



Sup. Figure B.3. Echo2 trench on Terrace 5 was dug 4m down beneath the surface. The exposed steep wall of columnar rocks parallel to the ground surface continued down. A. Facing the east side of the trench face; The top of the columnar rocks (Unit 3) was buried by soil fills containing some columnar-rock fragments; B. Looking down on the trench. It shows a peculiar soil-filled gap on the rock mass; C. Columnar rocks on this trench have been significantly much weathered, showing intensive spheroidal weathering; D1-3 Shows peculiar rock fragments from inside the trench with artificial sharp-tool marks.



Sup. Figure B.4. Trenching Charlie-1 on the east slope, down from Terrace 1. A. Showing buried columnar basaltic rocks oriented N70°E similar to those exposed in T1; B. West face of trench wall showing a thin layer of surface soils with lots of basaltic andesite rock fragments, C. Looking north, C&D. Showing mortars/fillers wrapping columnar rocks. The groundmass becomes very sticky like glue when immersed in water; E Shows broken small pieces of columnar rocks that have been carefully placed together (during construction)



Sup. Figure B.5. Trenching Charlie2 is located next to Charlie1. It shows irregular or non-columnar rock fragments that were carefully stacked together as part of the Unit 2 constructions.

Looking East/down



Trench Charlie-3

Looking West/up



T

Sup. Figure B.6. Charlie3 trench on the east slope down from Terrace 2. A&B The buried columnar rocks show smaller sizes than those like in the Charlie1 trench; C. showing a small piece of rectangular rocks that was taken between the larger columnar rocks, probably served as rock pegs to strengthen the structure; D. E showing an artistically shaped rock fragment from the trench like a *KUJANG* shape, a traditional – sacred weapon in Sundanese culture, E. showing a columnar rock with a triangular shape on its end. A bowl dent was covered by clayed-silt crust, possibly used to strengthen the columnar-rock stacks.

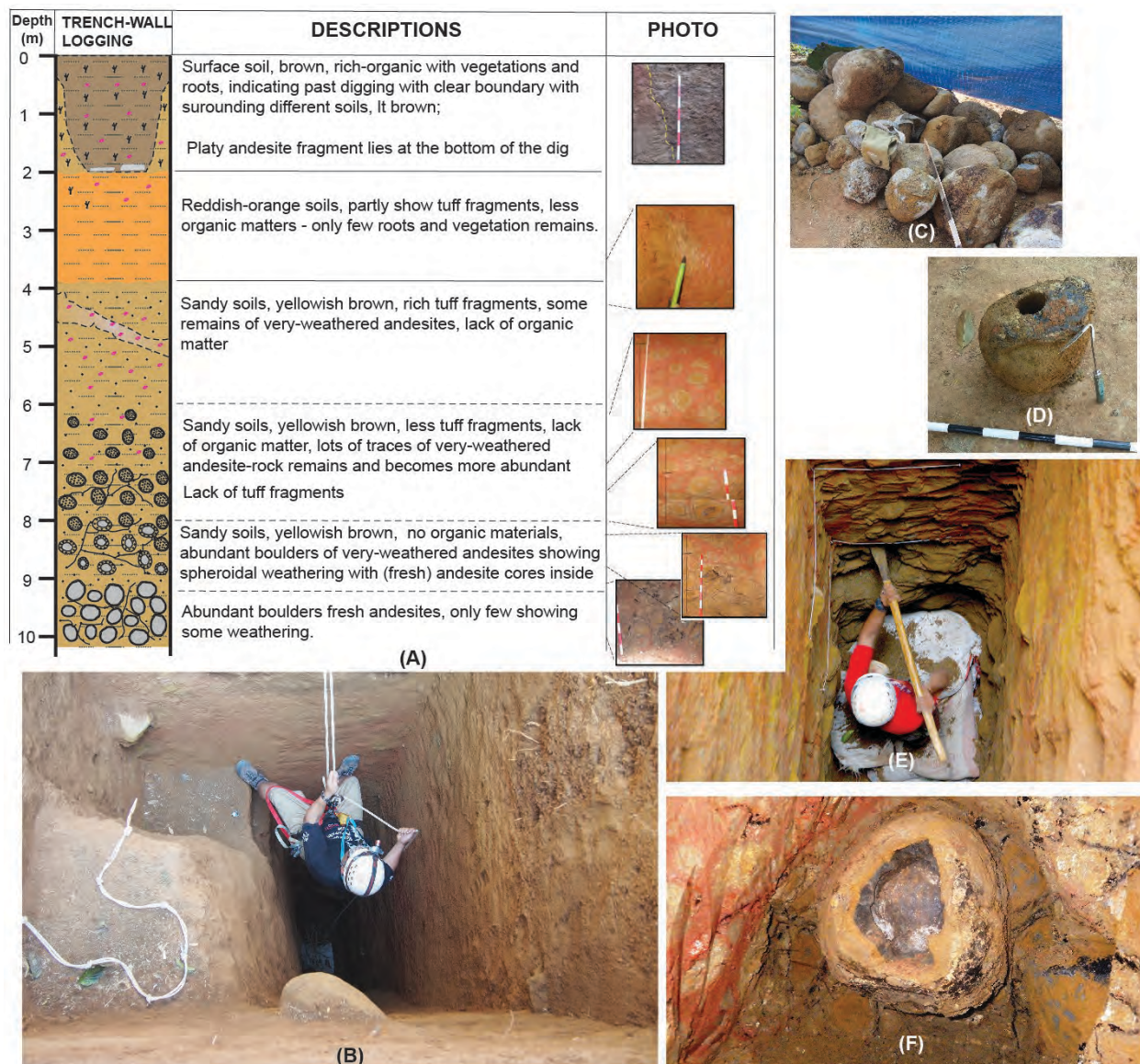


Sup. Figure B.7. Trenching Charlie4 is located next to Charlie3 on the east slope. A. Looking west upslope; B shows a lateral arrangement of columnar basaltic rocks that were regularly cut about 1-2 meters long on average and neatly stacked together; C shows an example of an artificial hole in between columnar rocks, which purpose is not clear; D. Columnar rock sticking on the wall; E showing a small artificial-shaped rock, probably serve as a strengthening pole between stacks of columnar rocks, showing another similar shape of the rock.

Trench Charlie-5

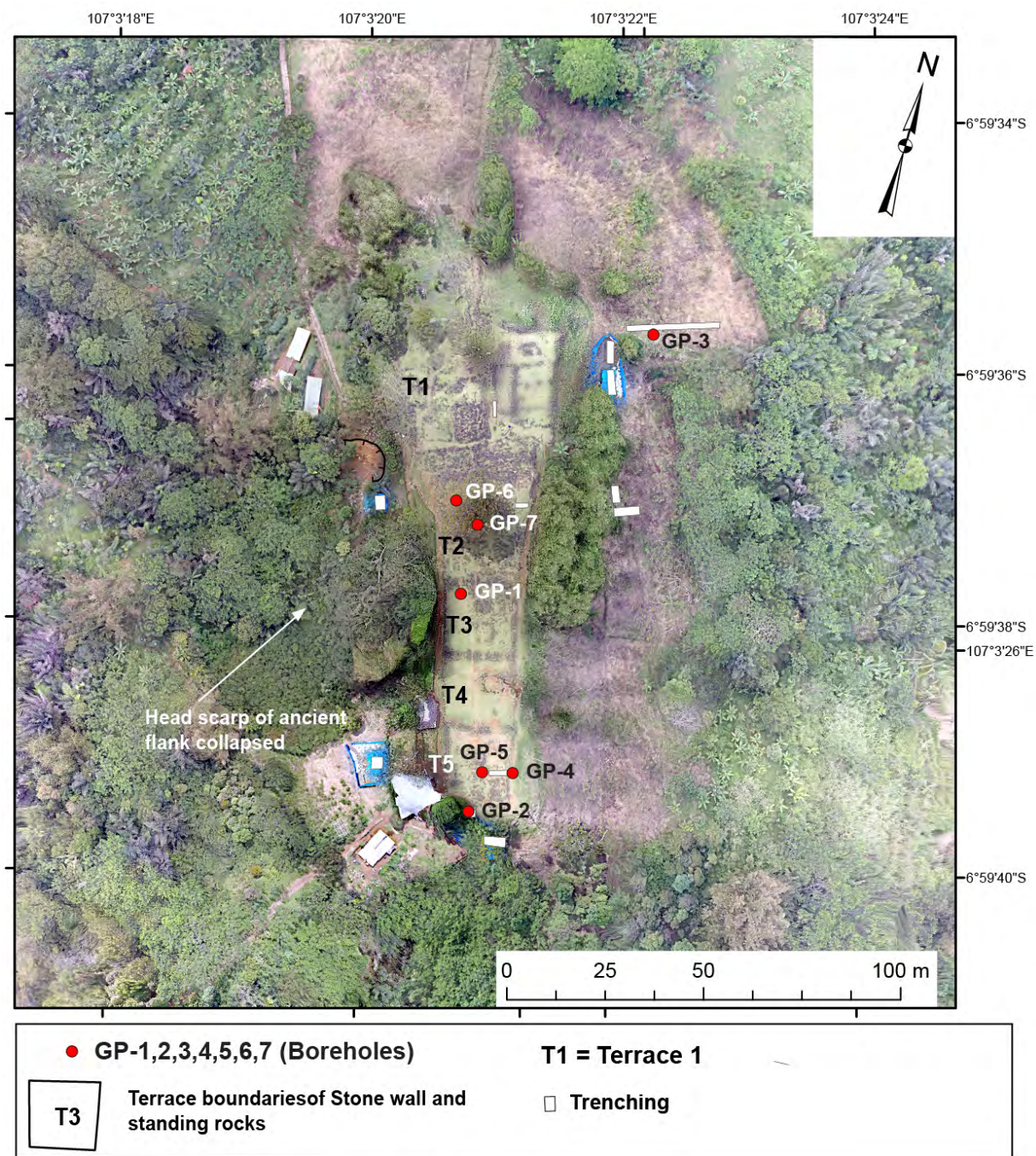


Sup. Figure B.8. Charlie5 trench on the east slope on the north side of Charlie1. The trench was excavated to explore the continuation of the buried Unit 2 down the slope. A. looking east up the slope; B – G showing various exposures of the buried columnar rock structures; H. Columnar rocks become suddenly less at the down end of the long trench.

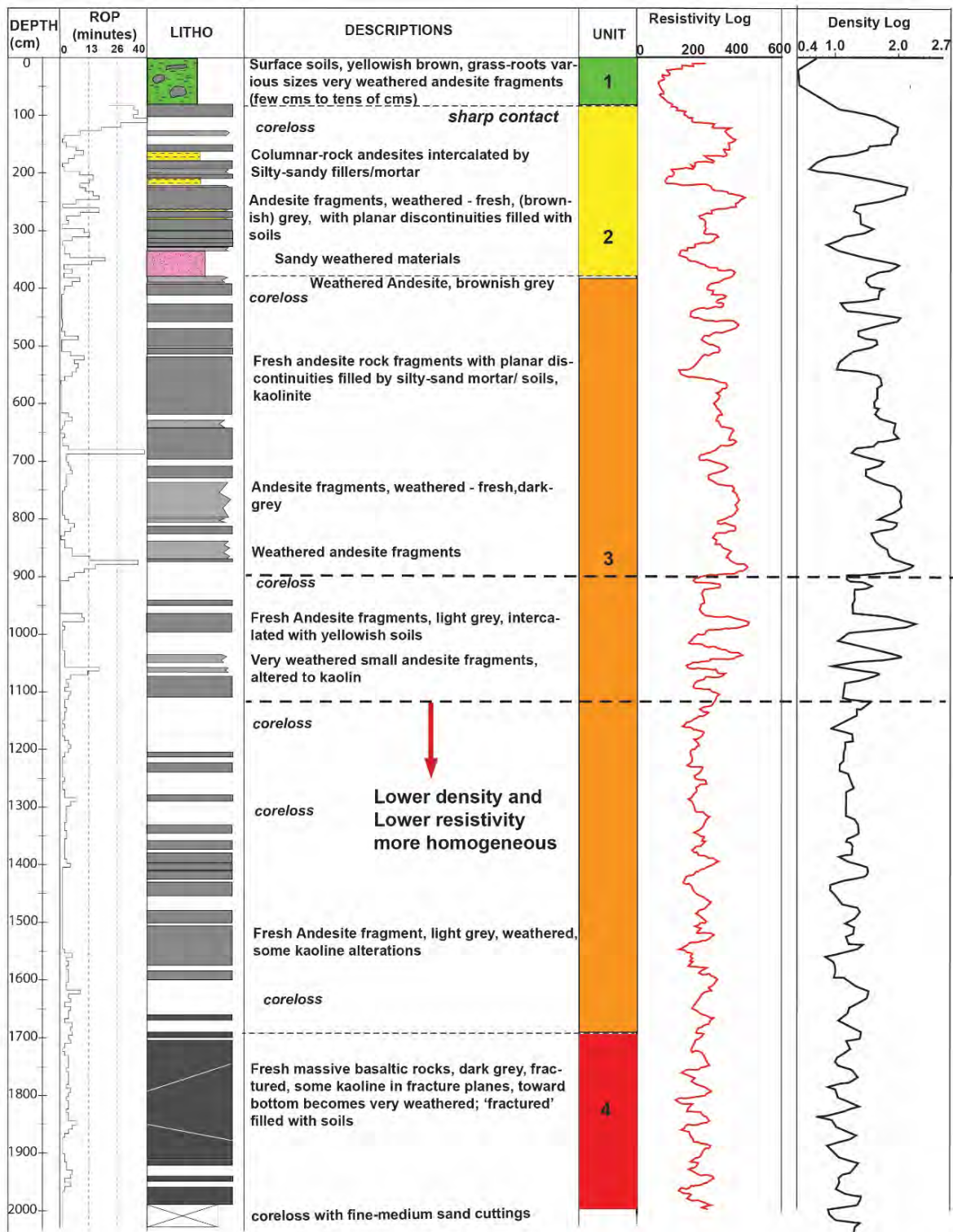


Sup. Figure B.9. (A) Stratigraphy of the Echo-1 deep trench wall; (B) Climbing down the trench; (C) Rounded basaltic-andesite boulders from the lower part of the trench; (D) The rock boulder that was drilled during the GP-2 drilling; (E)-(D) Taking the 'rolling stone' rock.

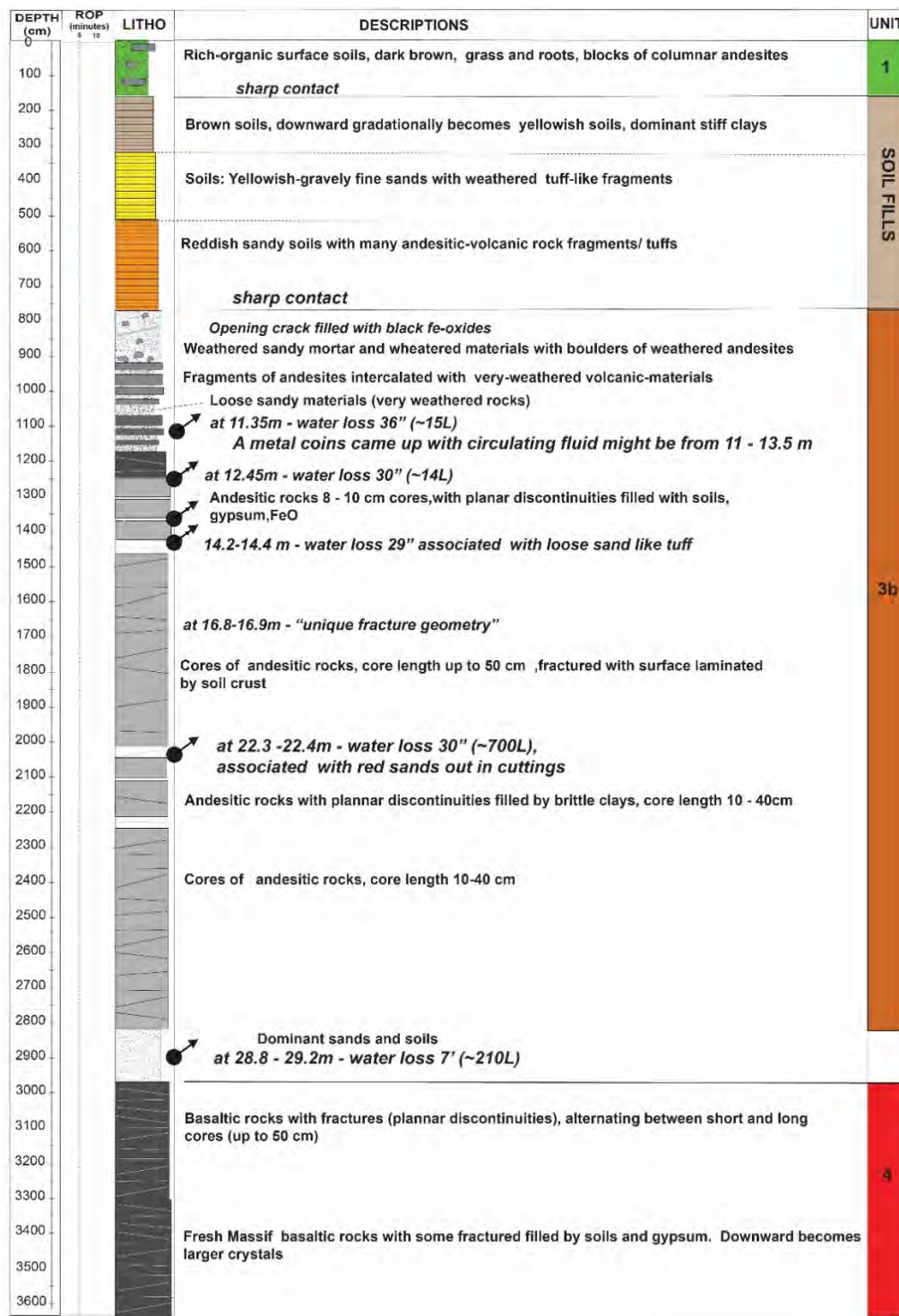
SUPPLEMENTARY FIGURE – C. CORE DRILLING



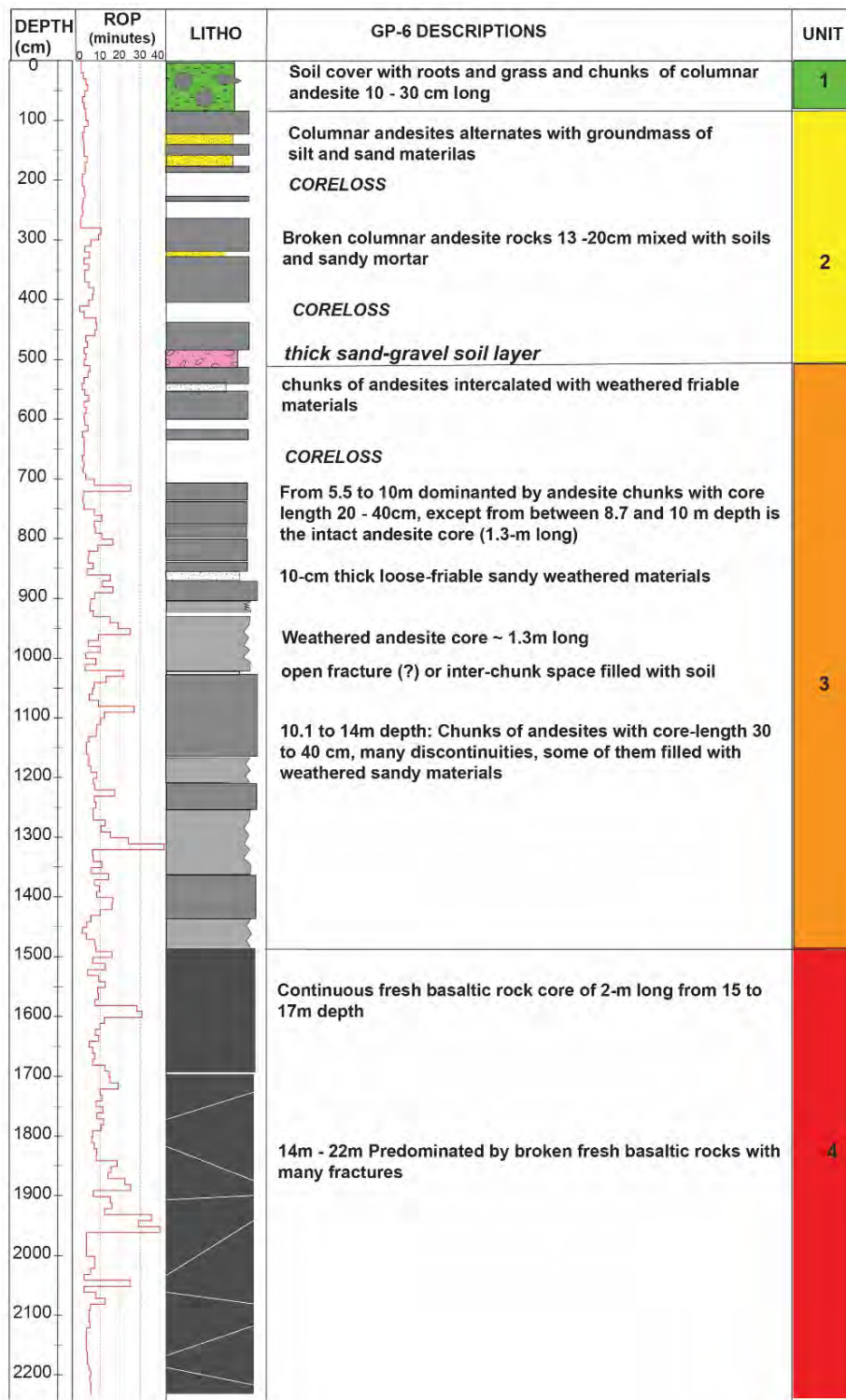
Sup.Figure-C.1. Index map of the borehole and the trenching sites, plotted on the orthophoto map.



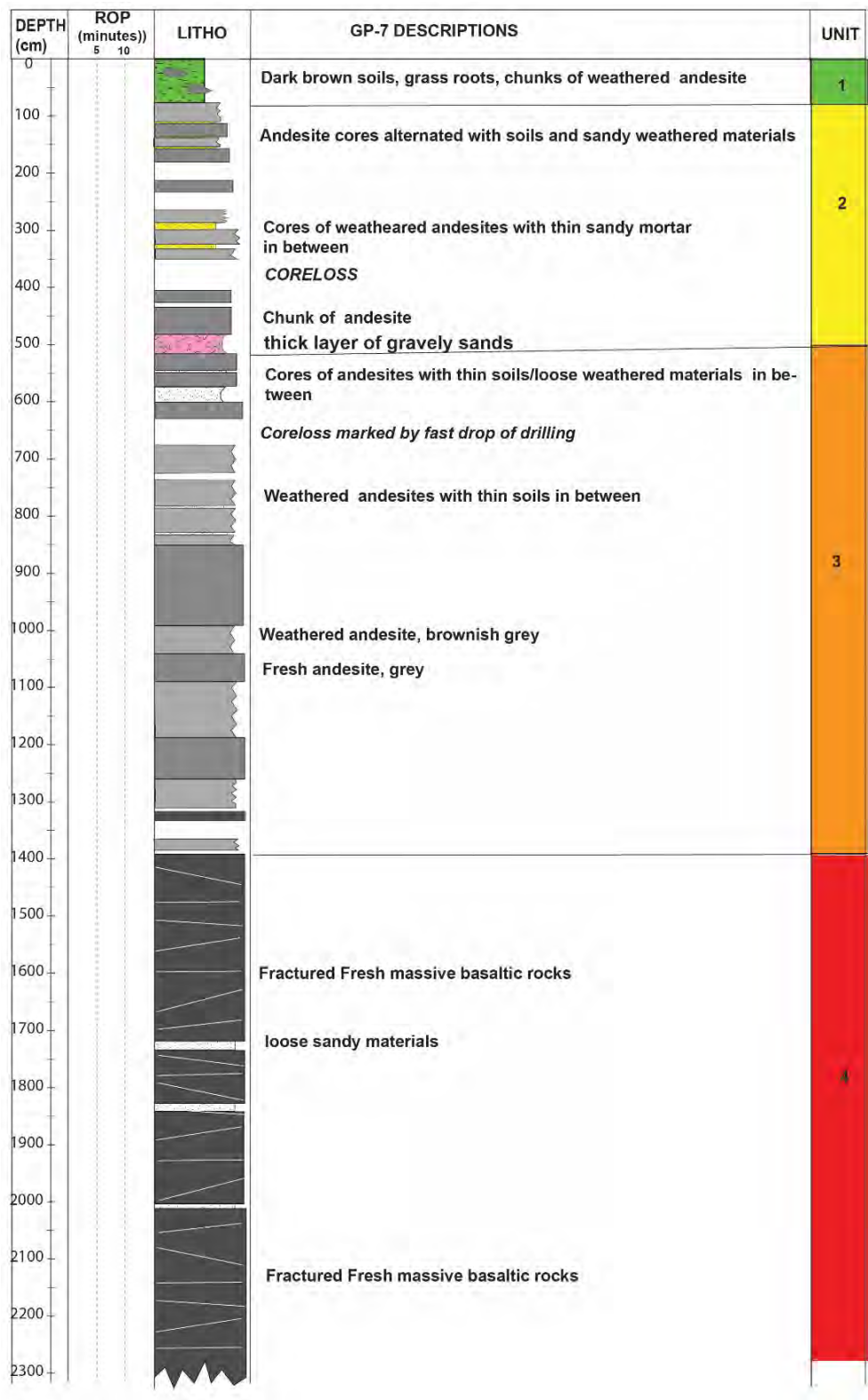
Sup.Figure-C.2. Borehole Log of core-drilling GP3 at the east slope. From 9 to 11 m depth resistivity and density decrease and becomes more homogeneous indicating different lithology (from the upper to the lower parts of Unit 3).



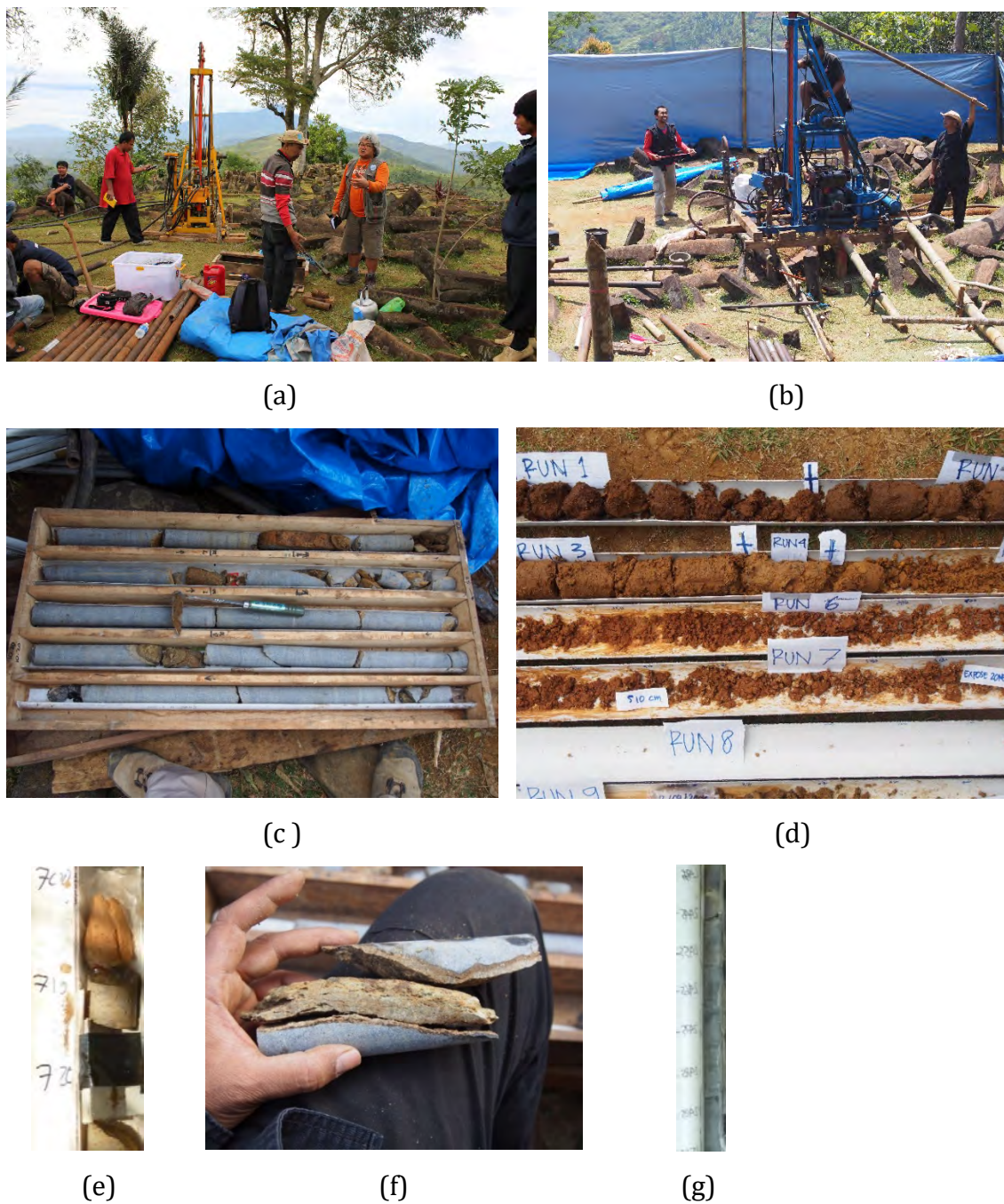
Sup.Figure-C.3. The Core-drilling Log of the GP5 at T5. From 1.5 to ~8m depth is the ancient soil fills that has a sharp contact with the underlying Unit 3 rocks. Regular waterloss and coreloss akin to the weak, weathered rocks. Massive basaltic rocks were encountered at about 30-m depth.



Sup.Figure-C.4. The core-drilling Log of the GP6 at T2. Core loss frequently occurred between 2 to 7 m depth. At approximately 10-m depth, it is the 1.3-m long-continuous andesite rock core possibly indicating an up-right columnar rock. Massive basaltic andesite was drilled at about 15-m depth.



Sup.Figure-C.5. The core-drilling Log of the GP7, similar to GP6 core loss frequently occurred between 2 to 7 m depth.



Sup. Figure-C.6. Core drilling activities: (a) Drilling equipment using JACRO-100 with diamond bit NQ 2" diameter and 5 feet core barrels, (b) GP5 site drilling used the wood-construction base to elevated the equipment from the megalithic stones, (c) Drill cores from GP7, (d) filled soil cores from GP5, (e) GP2 at 7m depth showing sharp contact between filled soil and rocks, (f) typical soil fillings between basaltic-andesitic rocks, (g) cores of fractured, massif basaltic rocks from GP1.

SUPPLEMENTARY FIGURE -D RADIOCARBON DATING ANALYSIS



Sup.Figure-D.1. Locations of samples for carbon-dating analysis from the trenches: (a) Charlie1, (b)Fanta, and (c). Echo2.

	BETA ANALYTIC INC.	4985 S.W. 74 COURT MIAMI, FLORIDA, USA 33155 PH: 305-667-5167 FAX:305-663-0964 beta@radiocarbon.com
	DR. M.A. TAMERS and MR. D.G. HOOD	

REPORT OF RADIOCARBON DATING ANALYSES

Dr. Danny Hilman Natawidjaja

Report Date: 10/23/2012

Indonesian Institute of Sciences (LIPI)

Material Received: 9/26/2012

Sample Data	Measured Radiocarbon Age	13C/12C Ratio	Conventional Radiocarbon Age(*)
Beta - 331493 SAMPLE : GP1-295 ANALYSIS : AMS-Standard delivery MATERIAL/PRETREATMENT : (organic sediment): acid washes 2 SIGMA CALIBRATION : Cal AD 1310 to 1360 (Cal BP 640 to 590) AND Cal AD 1390 to 1430 (Cal BP 560 to 520)	540 +/- 30 BP	-23.8 o/oo	560 +/- 30 BP
Beta - 331494 SAMPLE : GP1-1115 ANALYSIS : AMS-Standard delivery MATERIAL/PRETREATMENT : (organic sediment): acid washes 2 SIGMA CALIBRATION : Cal BC 14840 to 14690 (Cal BP 16790 to 16640)	13530 +/- 50 BP	-26.4 o/oo	13510 +/- 50 BP
Beta - 331495 SAMPLE : GP2-390 ANALYSIS : AMS-Standard delivery MATERIAL/PRETREATMENT : (organic sediment): acid washes 2 SIGMA CALIBRATION : Cal BC 7820 to 7600 (Cal BP 9770 to 9550)	8700 +/- 40 BP	-24.5 o/oo	8710 +/- 40 BP
Beta - 331496 SAMPLE : GP2-750 ANALYSIS : AMS-Standard delivery MATERIAL/PRETREATMENT : (organic sediment): acid washes 2 SIGMA CALIBRATION : Cal BC 25920 to 25040 (Cal BP 27870 to 26990)	22770 +/- 120 BP	-26.0 o/oo	22750 +/- 120 BP
Beta - 331497 SAMPLE : GP2-800 ANALYSIS : AMS-Standard delivery MATERIAL/PRETREATMENT : (organic sediment): acid washes 2 SIGMA CALIBRATION : Cal AD 1650 to 1680 (Cal BP 300 to 260) AND Cal AD 1730 to 1810 (Cal BP 220 to 140) Cal AD 1930 to post 1950 (Cal BP 20 to post 1950)	160 +/- 30 BP	-22.8 o/oo	200 +/- 30 BP
Beta - 331498 SAMPLE : GP2-1130 ANALYSIS : AMS-Standard delivery MATERIAL/PRETREATMENT : (organic sediment): acid washes 2 SIGMA CALIBRATION : Cal BC 21460 to 21020 (Cal BP 23410 to 22970)	19410 +/- 80 BP	-25.9 o/oo	19400 +/- 80 BP
Beta - 331499 SAMPLE : LIA-01 ANALYSIS : AMS-Standard delivery MATERIAL/PRETREATMENT : (charred material): acid/alkali/acid 2 SIGMA CALIBRATION : Cal AD 690 to 880 (Cal BP 1260 to 1060)	1210 +/- 30 BP	-23.6 o/oo	1230 +/- 30 BP

Sup.Figure-D.2. Results of carbon dating – AMS – analysis for samples from boreholes (GP1 & GP2).

	BETA ANALYTIC INC.	4985 S.W. 74 COURT MIAMI, FLORIDA, USA 33155 PH: 305-667-5167 FAX: 305-663-0964 beta@radiocarbon.com
	DR. M.A. TAMERS and MR. D.G. HOOD	

REPORT OF RADIOCARBON DATING ANALYSES

Mr. Mudrik Daryono

Report Date: 12/8/2015

Indonesian Institute of Sciences

Material Received: 11/13/2015

Sample Data	Measured Radiocarbon Age	$\delta^{13}C$	Conventional Radiocarbon Age(*)
Beta - 423689 SAMPLE : HM4 ANALYSIS : AMS-Standard delivery MATERIAL/PRETREATMENT : (organic sediment): acid washes 2 SIGMA CALIBRATION : Cal BC 2025 to 1885 (Cal BP 3975 to 3835)	3610 \pm 30 BP	-23.8 ‰	3630 \pm 30 BP
Beta - 423690 SAMPLE : ES1 ANALYSIS : AMS-Standard delivery MATERIAL/PRETREATMENT : (organic sediment): acid washes 2 SIGMA CALIBRATION : Cal BC 6325 to 6315 (Cal BP 8275 to 8265) and Cal BC 6250 to 6210 (Cal BP 8200 to 8160) and Cal BC 6135 to 6115 (Cal BP 8085 to 8065)	7370 \pm 30 BP	-23.3 ‰	7400 \pm 30 BP
Beta - 423691 SAMPLE : FC5 ANALYSIS : AMS-Standard delivery MATERIAL/PRETREATMENT : (charred material): acid/alkali/acid 2 SIGMA CALIBRATION : Cal AD 1425 to 1475 (Cal BP 525 to 475)	490 \pm 30 BP	-25.9 ‰	480 \pm 30 BP

Sup.Figure-D.3. Results of carbon dating – AMS – analysis for samples from trenches.



BADAN TENAGA NUKLIR NASIONAL
(NATIONAL NUCLEAR ENERGY AGENCY)
PUSAT APLIKASI TEKNOLOGI ISOTOP DAN RADIASI
CENTER FOR THE APPLICATION OF ISOTOPES AND RADIATION TECHNOLOGY
Jalan Lebak Bulus Raya Kotak Pos 7002 JKSKL, Jakarta 12070 Indonesia
Telp. 62-021-7690709, Fax. 62-021-7691607, 7513270, Home page : www.batan.go.id/patir, E-mail : patir@batan.go.id

RESULTS OF ^{14}C ANALYSIS, 19 APRIL 2013.

Sample name	Percent Modern Carbon (PMC)	Conventional C-14 Age years BP
CH1-3	69,38 \pm 0,95	3025 \pm 30
CH1-4	64,47 \pm 0,80	3630 \pm 40

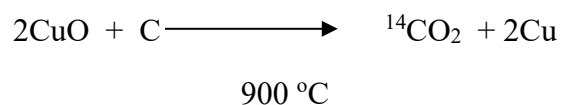
CH1-5	42,40 ± 0,60	7095 ± 60
GP1-500	45.2 ± 0,70	6700 ± 70

Sup.Figure-D.4. Results of radiocarbon dating analysis at BATAN-INA. All samples are organic soil. CH1-3, CH1-4, and CH1-5 Samples were taken from Charlie-1 Trench. GP1-500 is from GP1 cores at 5m depth. The method of analysis is given below.

Method of Carbon Dating analysis in BATAN-INA

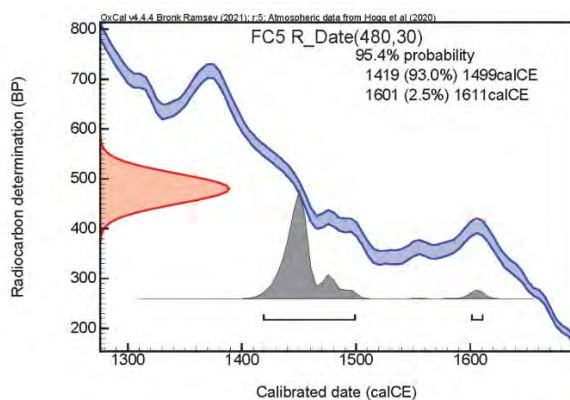
Flow-chart: Soil Sample → Pre-Treatment → Burning → $^{14}\text{CO}_2$ → Counting ^{14}C → Carbon Age

The burning is conducted in the burning tube, which is connected to the CO_2 line. Before burning, samples were heated at 200 °C for one night to vaporize water and contaminated agents. The burning requires strong oxidator CuO. Hence, soil samples and CuO are mixed evenly with ratio 100 : 1 (for every 100 gram soil sample 1 gram CuO is added). This mixture is burned in the burning tube at 900 °C in vacuum condition for about 2-3 hours. The burning produces CO_2 :

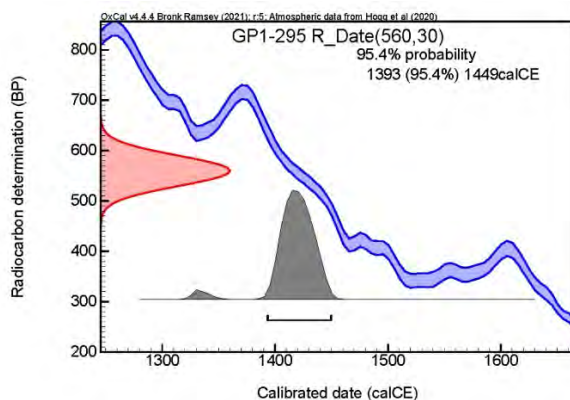


$^{14}\text{CO}_2$ from the burning is collected in the flask at -180 °C. Then, $^{14}\text{CO}_2$ was absorbed by Carbosorb, and then its ^{14}C activity is measured using Liquid Scintillation Counter.

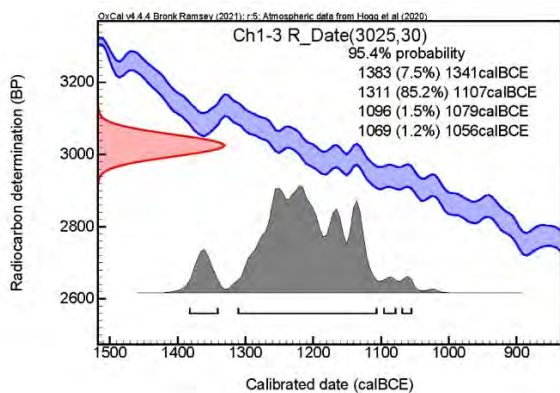
The method for carbon dating analysis uses the Oxalic Acid Standard SRM 4990-C from the National Bureau of Standard, Washington DC, USA.



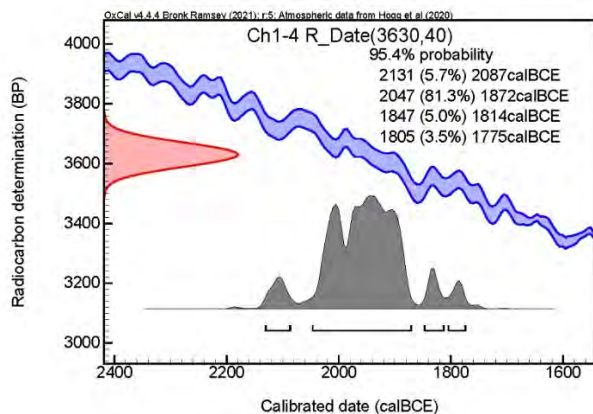
Sup.Figure-D.5. OxCal Calibration for FC5 carbon dating from conventional C age to Calendar Age.



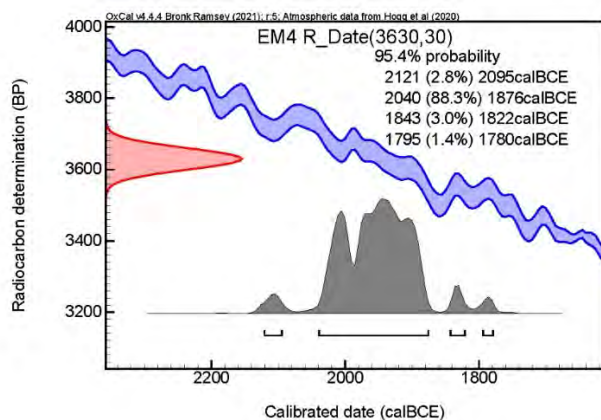
Sup.Figure-D.6. OxCal Calibration for the GP1-295 carbon dating from the conventional ^{14}C age to the Calendar Age.



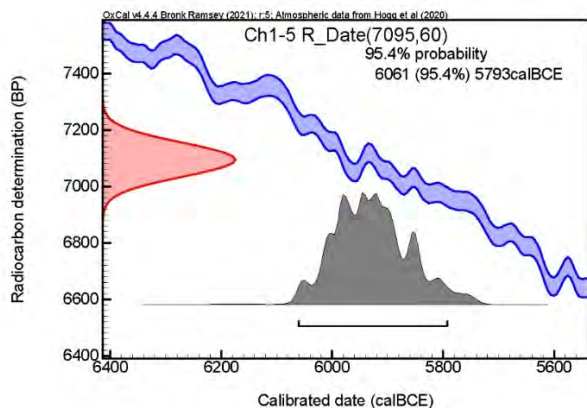
Sup.Figure-D.7. OxCal Calibration for the CH1-3 carbon dating from the conventional ^{14}C age to the Calendar Age.



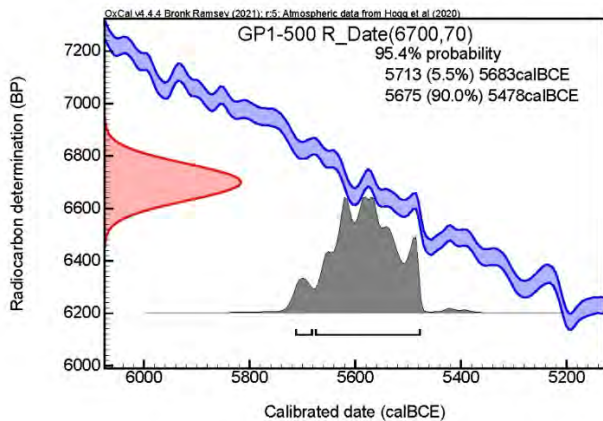
Sup.Figure-D.8. OxCal Calibration for the CH1-4 carbon dating from the conventional ^{14}C age to the Calendar Age.



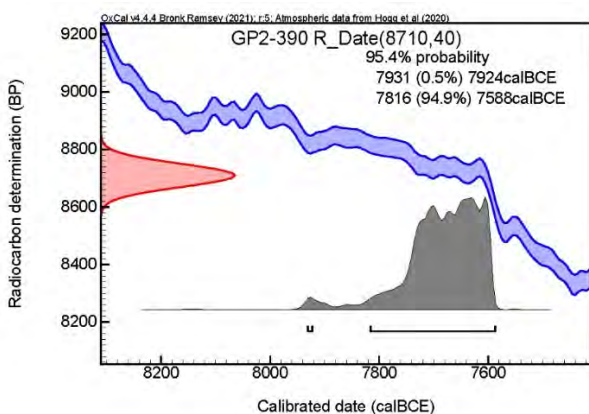
Sup.Figure-D.9. OxCal Calibration for the EM4 carbon dating from the conventional ^{14}C age to the Calendar Age



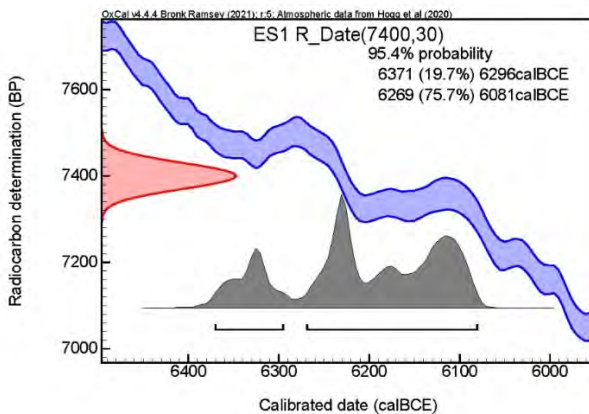
Sup.Figure-D.10. OxCal Calibration for the CH1-5 carbon dating from the conventional ^{14}C age to the Calendar Age



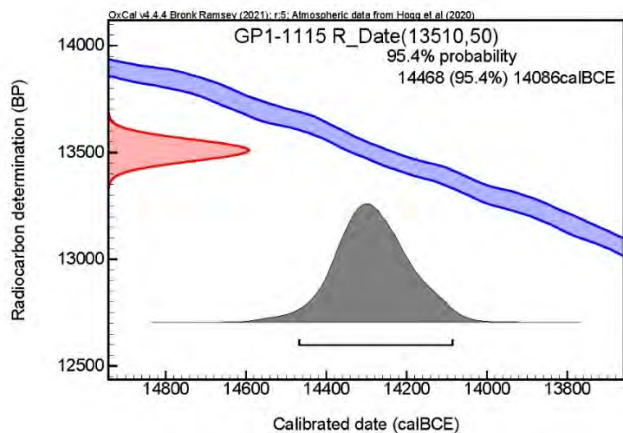
Sup.Figure-D.11. OxCal Calibration for the GP1-500 carbon dating from the conventional ^{14}C age to the Calendar Age



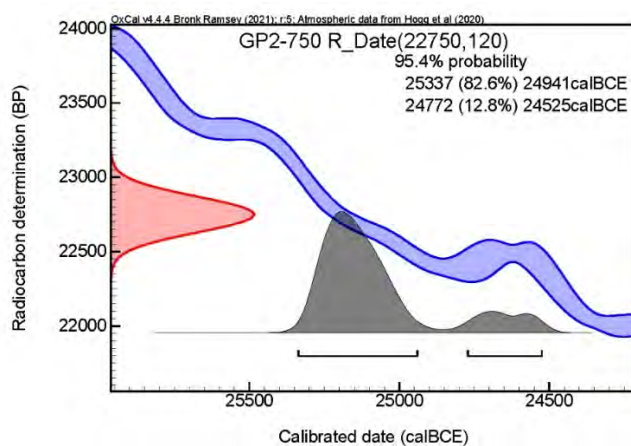
Sup.Figure-D.12. OxCal Calibration for the GP2-390 carbon dating from the conventional ^{14}C age to the Calendar Age.



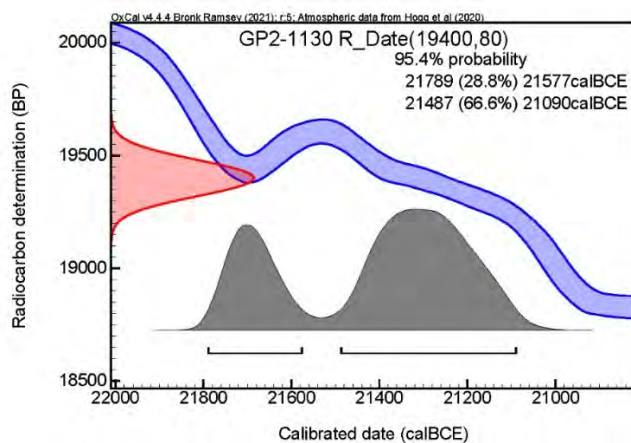
Sup.Figure-D.13. OxCal Calibration for the ES1 carbon dating from the conventional ^{14}C age to the Calendar Age.



Sup.Figure-D.14. OxCal Calibration for the GP1-1115 carbon dating from the conventional ^{14}C age to the Calendar Age.



Sup.Figure-D.15. OxCal Calibration for the GP2-750 carbon dating from the conventional ^{14}C age to the Calendar Age.



Sup.Figure-D.16. OxCal Calibration for the GP2-1130 carbon dating from the conventional ^{14}C age to the Calendar Age.

SUPPLEMENTARY FIGURE – E GROUND PENETRATING RADAR (GPR)

GPR METHOD IN THIS STUDY

The GPR survey at Gunung Padang utilized GSSI GPR instruments with various antennae and frequencies, including the MLF 15MHz, 40 MHz, 80 MHz, 100 MHz Shielded antenna, and 240 MHz shielded antenna. However, this paper focuses on the results obtained from the GPR survey conducted with the MLF 40 MHz antenna.

The raw GPR data was processed using RADAN Software, following several steps:

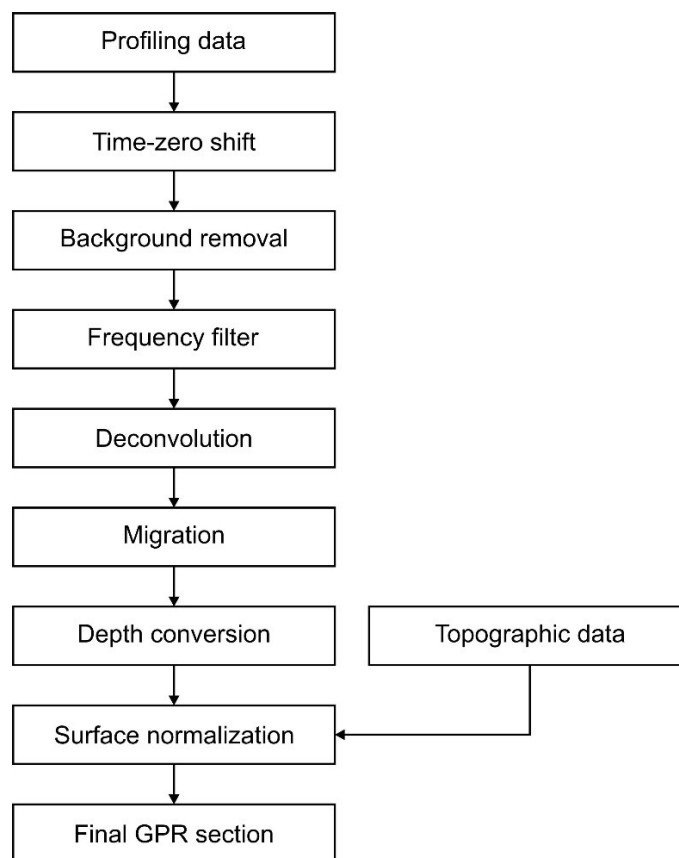
- Time Zero correction
- Filtering FIR, IIR, and background removal
- Migration and velocity analysis using the Common Depth Point (CDP) method
- Adjustment of scan parameters, including horizontal scaling and distance normalization
- Adjustment of surface parameters, such as surface normalization and topographic profile
- Gain adjustment, including range gain, gain restoration, and adaptive gain
- Waveform analysis, specifically deconvolution.

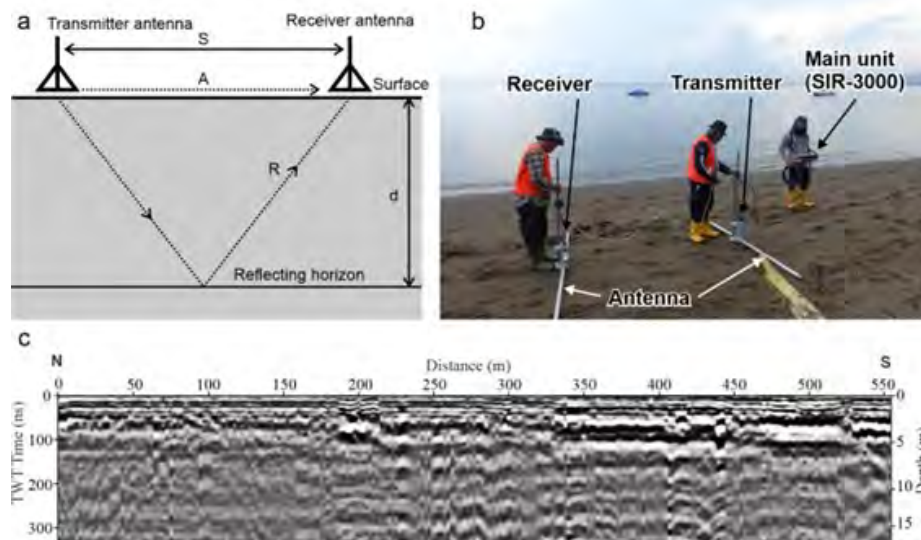
Velocity plays a crucial role in GPR surveys as it is used to convert the travel time of radar waves into depth. The velocity of radar waves in the subsurface can vary depending on the properties of the materials they pass through. In this study, the average electromagnetic (EM) velocity at Gunung Padang was estimated to be approximately 0.105 m/ns.

The CDP method was employed for velocity estimation. This method utilizes the travel time of reflected signals from common depth points, which are subsurface locations equidistant from the transmitting and receiving antennas. The reflection time for each CDP is measured from the recorded signals and converted to depth using the known propagation velocity of electromagnetic waves in the air. The CDP method is advantageous for velocity estimation as it is less sensitive to subsurface variations compared to other methods. By using common depth points, the impact of small-scale subsurface variations on velocity estimation is reduced.

Table E.1 GPR acquisition parameters and Flow Chart of GPR Processing

Instrument / Manufacturer	SIR-3000 / Geophysical Survey Systems, Inc. (GSSI), USA
Frequency	40 MHz
Transmitter-receiver spacing	2 m
Scan point interval	1–2 m
Number of channels	1
Sampling interval	16 ns
Number of samples per scan	512

Flow Chart:



(a)



(b)



(c)

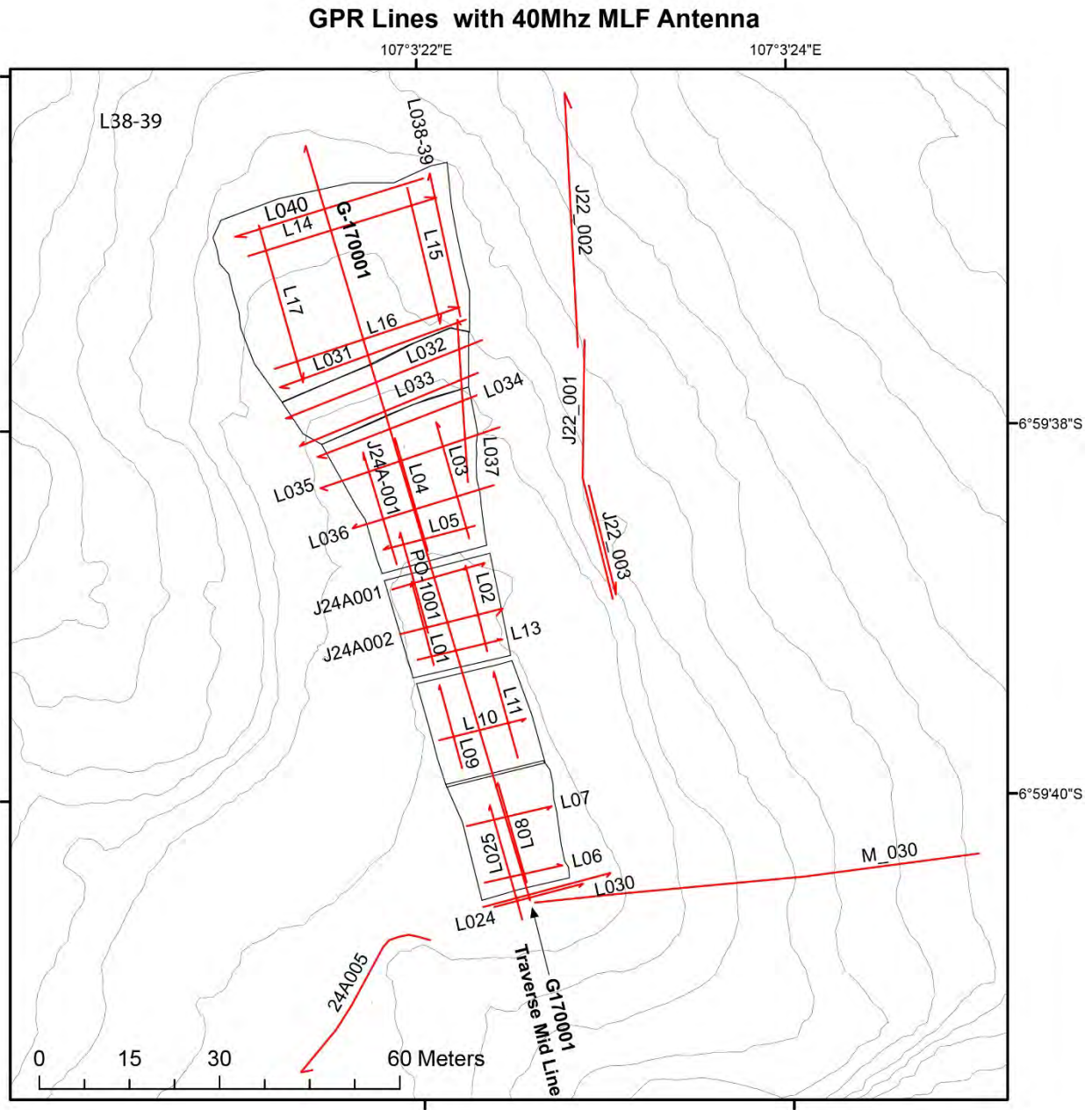


(d)

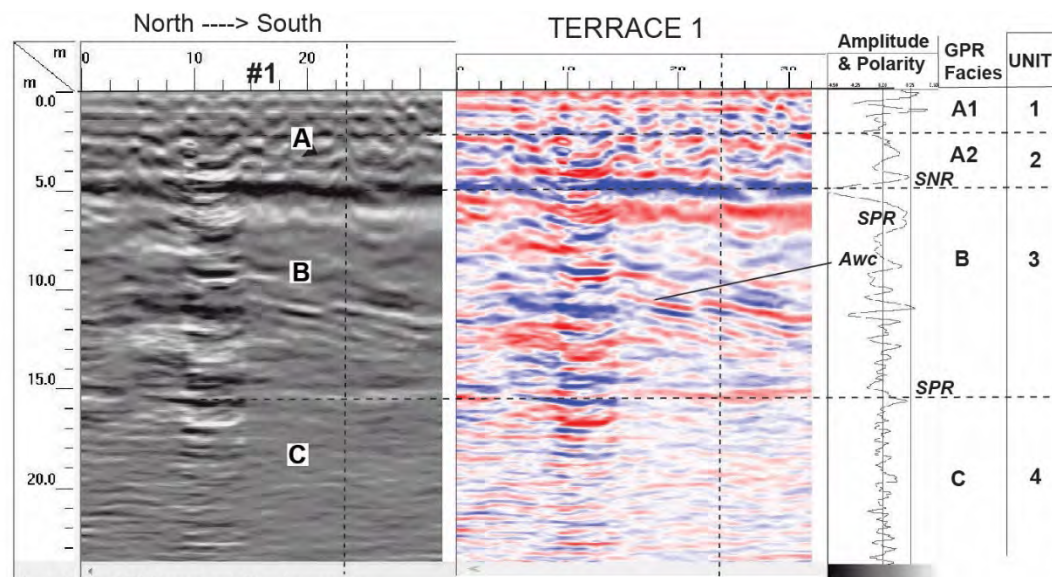


(e)

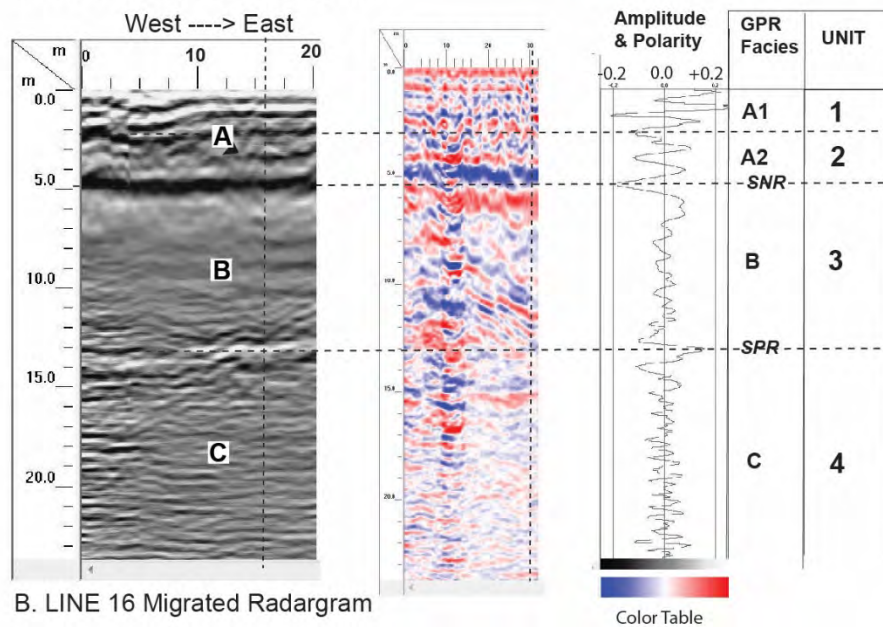
Sup.Figure-E.1. The GPR technique and surveys conducted at Gunung Padang: (a) GPR technique and principle illustrating the GPR antenna, which consists of a transmitter and receivers for electromagnetic waves. (b) GPR survey on T2&3 using MLF 40MHz. (c) GPR survey using high-res shielded antenna 400 MHz, combined with shallow excavations. (d) GPR survey using MLF 15 MHz on the high ramp between T1 and T2. (e) Down the hill.



Sup.Figure-E.2. displays the site index map indicating the GPR survey lines conducted using the MLF 40 MHz antenna. The map provides an overview of the specific locations and paths of the GPR surveys carried out at Gunung Padang.



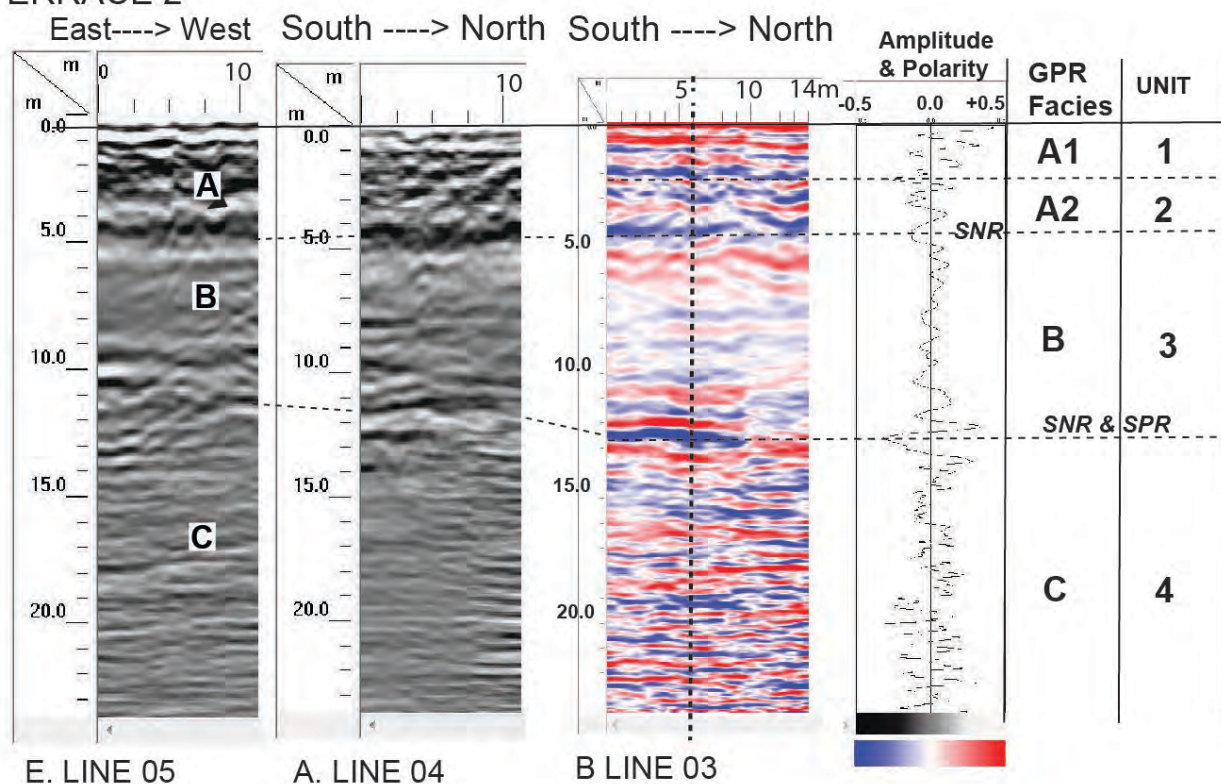
A. LINE 17 Migrated Radargram



B. LINE 16 Migrated Radargram

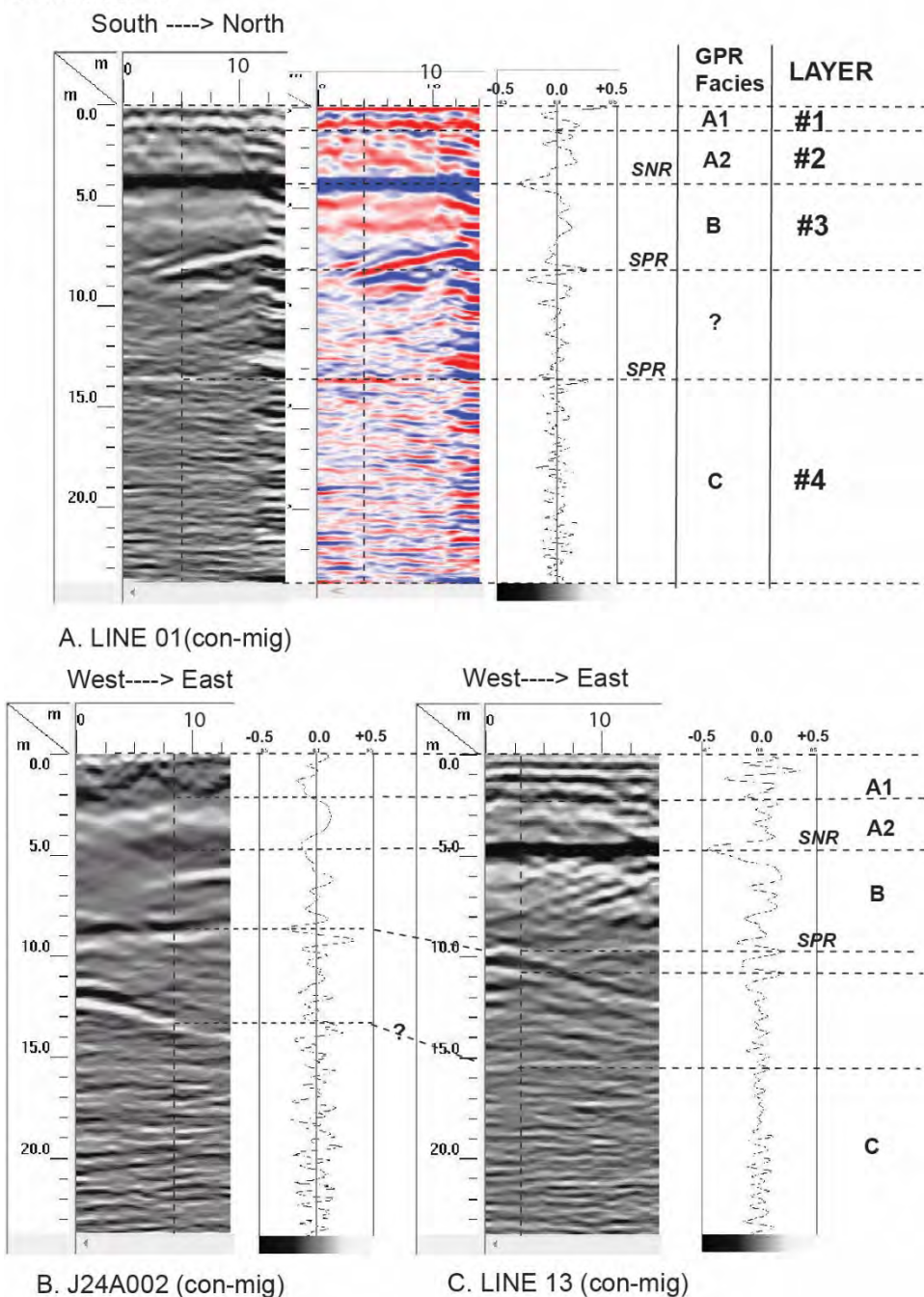
Sup.Figure-E.3. results of short GPR survey lines conducted on T1 using the MLF antenna at 40 MHz. The figure showcases the radargrams, amplitudes, and polarity of the GPR data, along with the interpretation of radar facies and their correlation with the rock units. The grey radargrams provide insights into the textures and structures observed, while the red and blue radargrams depict the polarities. Notably, the GPR facies are distinguished based on their textures, patterns, structures/geometries, amplitudes, and polarities. Strong Negative Refractor (SNR) and Strong Positive Refractor (SPR) often act as boundaries or markers within the GPR facies. All radargrams have undergone essential processing steps such as filtering, deconvolution, and migration to enhance their interpretability.

TERRACE 2

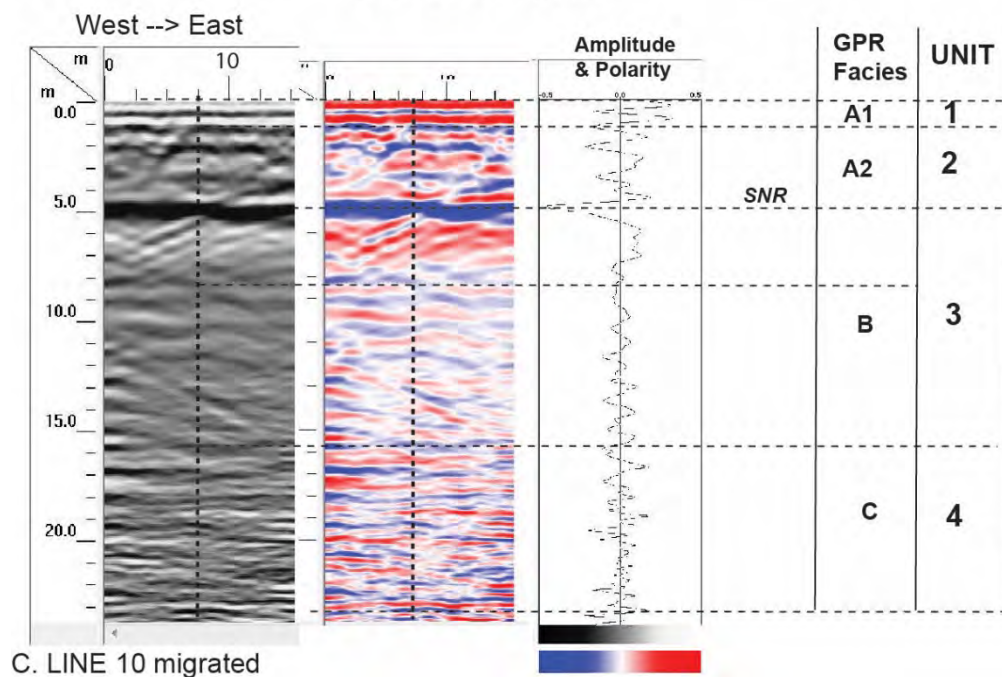
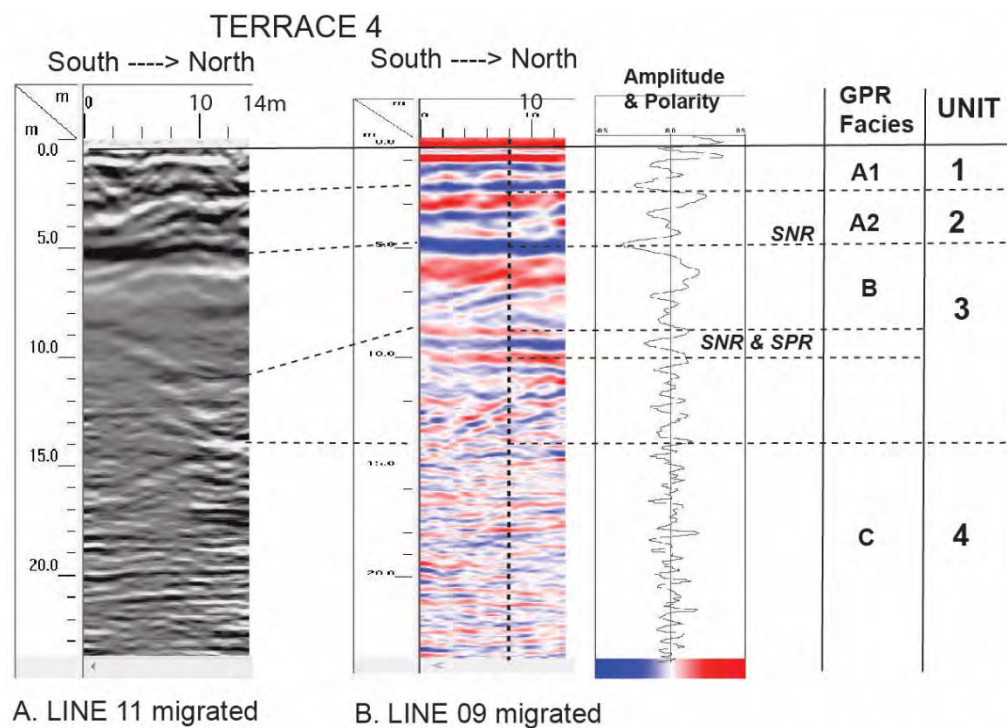


Sup. Figure-E.4. Showcases the results of short GPR survey lines conducted on T2 using the MLF antenna at 40 MHz. The figure provides further insights into the radargrams, amplitudes, and polarity of the GPR data, building upon the explanations provided in Supplementary Figure E.3. Notably, the boundary between Unit-2 and Unit-3 is demarcated by a strong/solid negative reflector (SNR), while strong reflectors frequently indicate the boundary between Unit-3 and Unit-4. Each radar facies is characterized by its distinct textures, patterns, and is also defined by its amplitude and polarity.

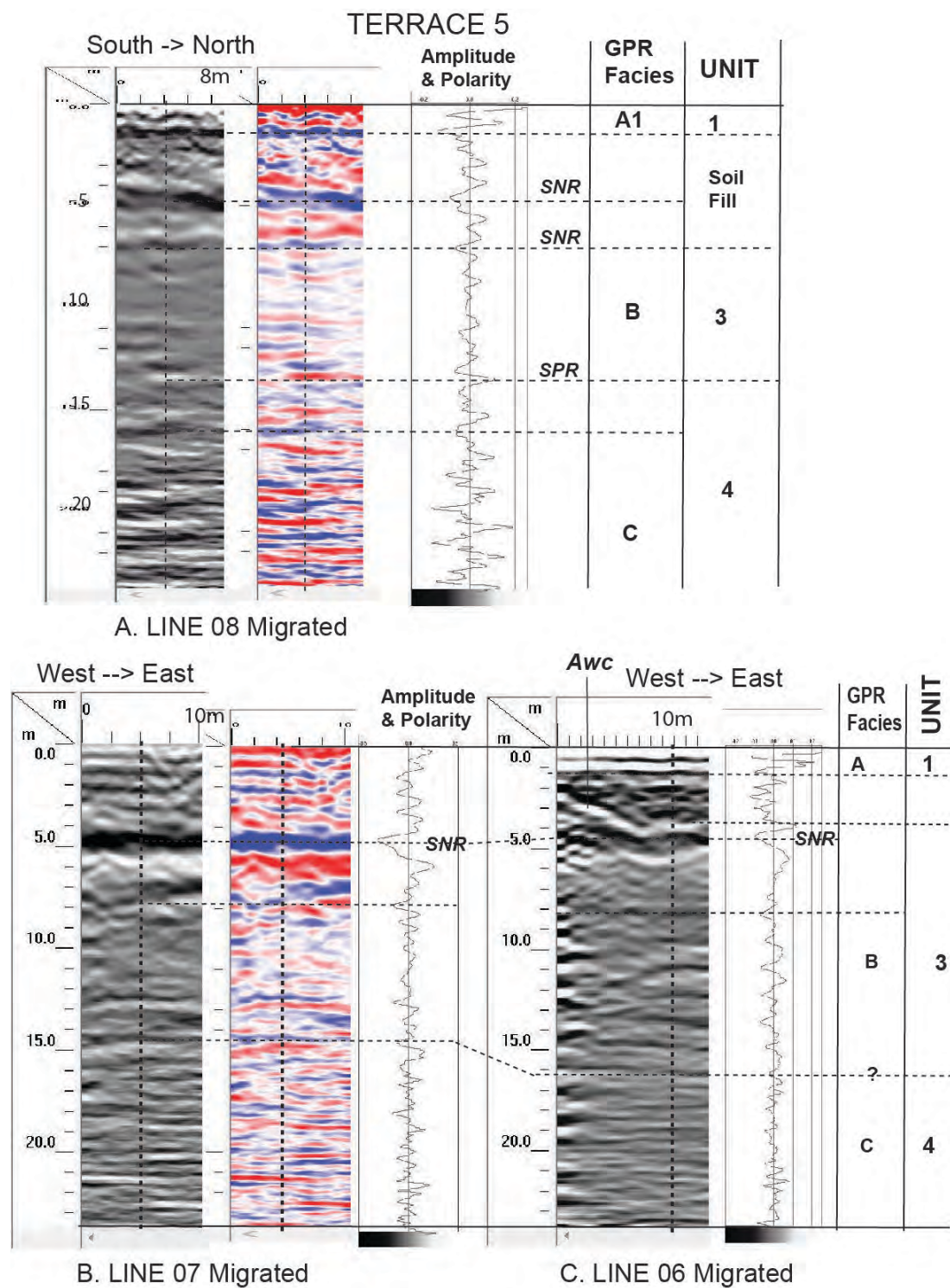
TERRACE 3



Sup.Figure-E.5. Presents the outcomes of short GPR survey lines carried out on T3 using the MLF antenna at 40 MHz. For detailed descriptions and explanations, please refer to Supplementary Figures E.3 and E.4. These figures provide insights into the radargrams, amplitudes, polarity, and interpretations of the GPR data collected on T3. By studying these figures collectively, a comprehensive understanding of the subsurface structures and features can be obtained.



Sup.Figure-E.6. showcases the results obtained from short GPR survey lines conducted on T-4 using the MLF antenna at 40 MHz. For detailed explanations and descriptions, please refer to Supplementary Figures E.3 and E.4.



Sup.Figure-E.7. illustrates the outcomes obtained from short GPR survey lines performed on T5 using the MLF antenna at 40 MHz. For detailed explanations and descriptions, please refer to Supplementary Figures E.3 and E.4.

SUPPLEMENTARY FIGURE – F. ELECTRICAL RESISTIVITY TOMOGRAPHY (ERT)

Equipment and Methods

For the geophysical surveys conducted in this study, two sets of the SuperSting R8-AGI System were utilized. One set included 56-electrode cables, while the other set had 112-electrode cables. The SuperSting system consists of several components, including the main unit, switchbox, cables, electrodes, and a car battery. Robust data processing was performed using the Earth Imager software.

The data processing workflow involved several steps. Initially, raw ERT data from the survey were prepared, and a topographic-profile file was created using ZipLevel measurements. In the Earth Imager software, data were fixed and insufficient data were deleted. Inversion parameters, including the initial setting, forward-modeling setting, and resistivity inversion setting, were set to obtain the best-fit model.

The initial setting included parameters such as minimum voltage, minimum V/I, maximum repeat error, minimum apparent resistivity, maximum apparent resistivity, maximum reciprocal error, and the choice of inversion method. The forward modeling utilized the finite element method, Cholesky decomposition for the forward equation solver, and Dirichlet boundary condition. The resistivity inversion settings involved the number of iterations, maximum RMS error, smoothness factor, damping factor, estimated noise, resolution factor, maximum resistivity, and horizontal/vertical roughness ratio.

The inversion modeling process aimed to minimize the data misfits between field measurements and the calculated data of the reconstructed model. The data misfit was evaluated using parameters such as root mean squares (RMS) and L2 norm. However, it is important to note that achieving a lower RMS or L2 norm does not necessarily indicate a better model. Lower RMS values can be obtained by eliminating data considered noise by the software, but such data may contain important signals. Hence, data removal was carefully considered.

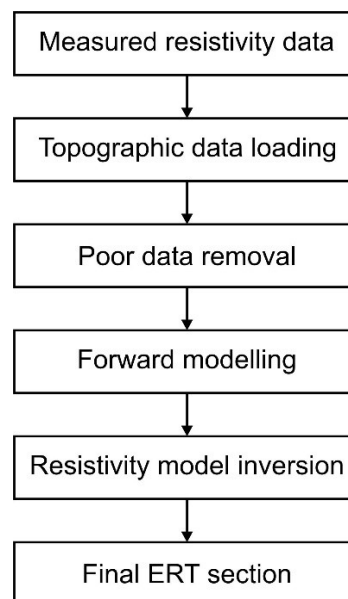
The inversion modeling was repeated multiple times until confidence was established in the constructed resistivity model's validity and reliability. The default "surface" model in Earth Imager was initially used and then adjusted by modifying the initial condition and inverse resistivity

setting parameters. The objective was to ensure that the resistivity model accurately represented the subsurface conditions and provided meaningful insights into the target structures

Table F.1 ERT measurement parameters & Flow chart of ERT data processing

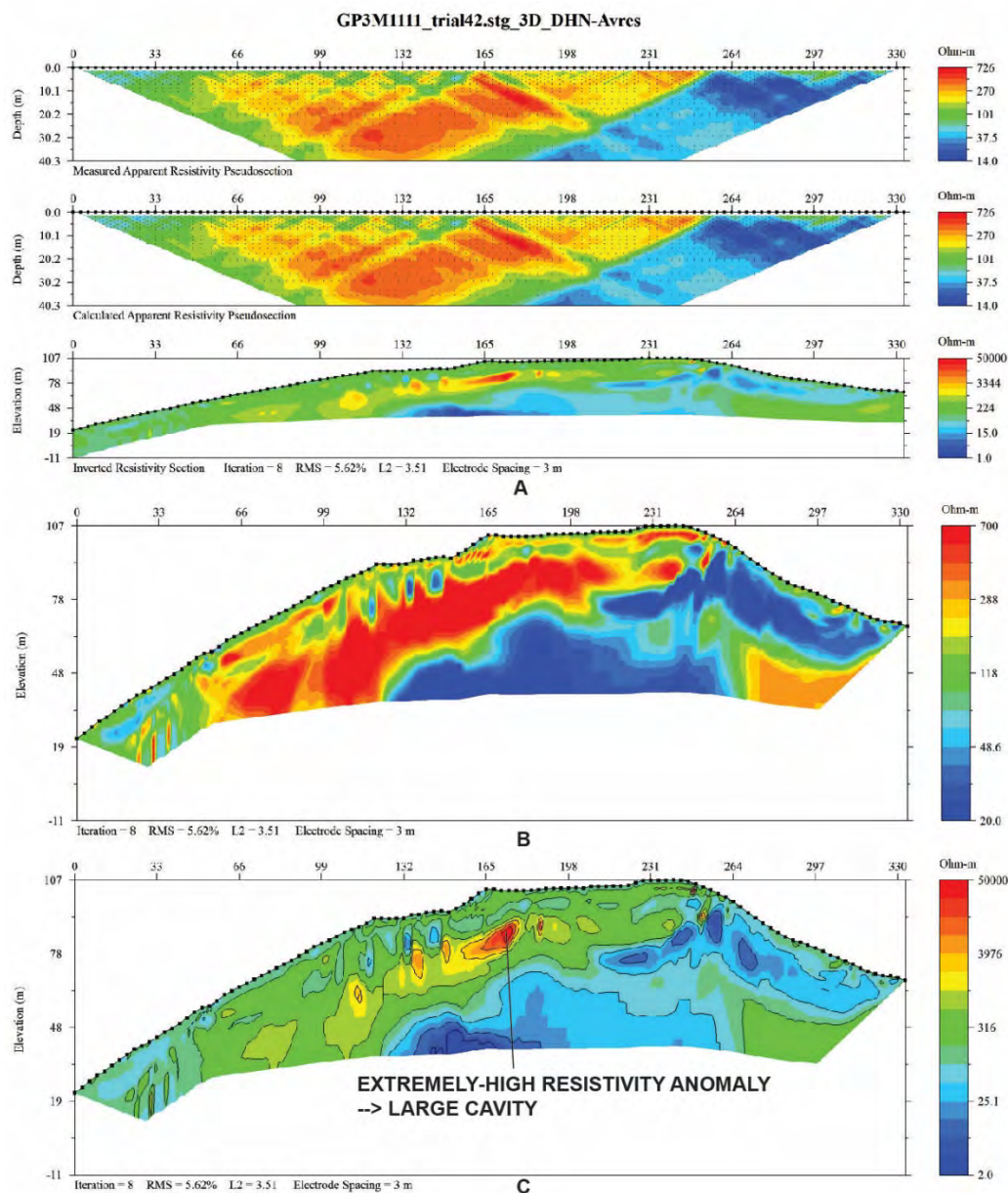
Instrument / Manufacturer	Supersting IP R8 / Advanced Geosciences Inc. (AGI), USA
Power supply	12V or 2x12V DC
Output current	1–2000 mA
Measuring resolution	Max 30 nV
Input channel	8 channels
No. electrode	112
Electrode spacing	1.5–5 m

Flowchart of ERT data processing

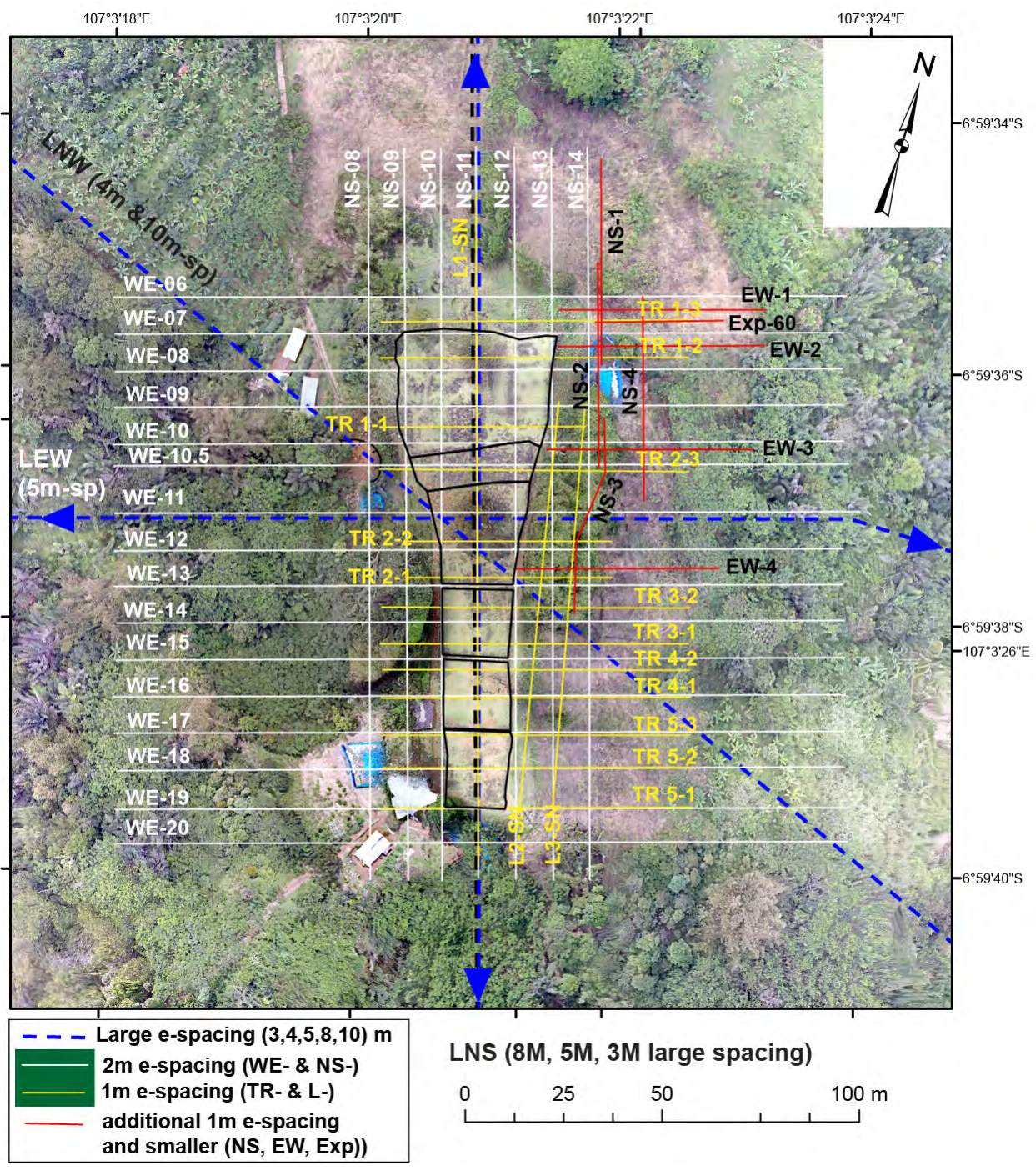




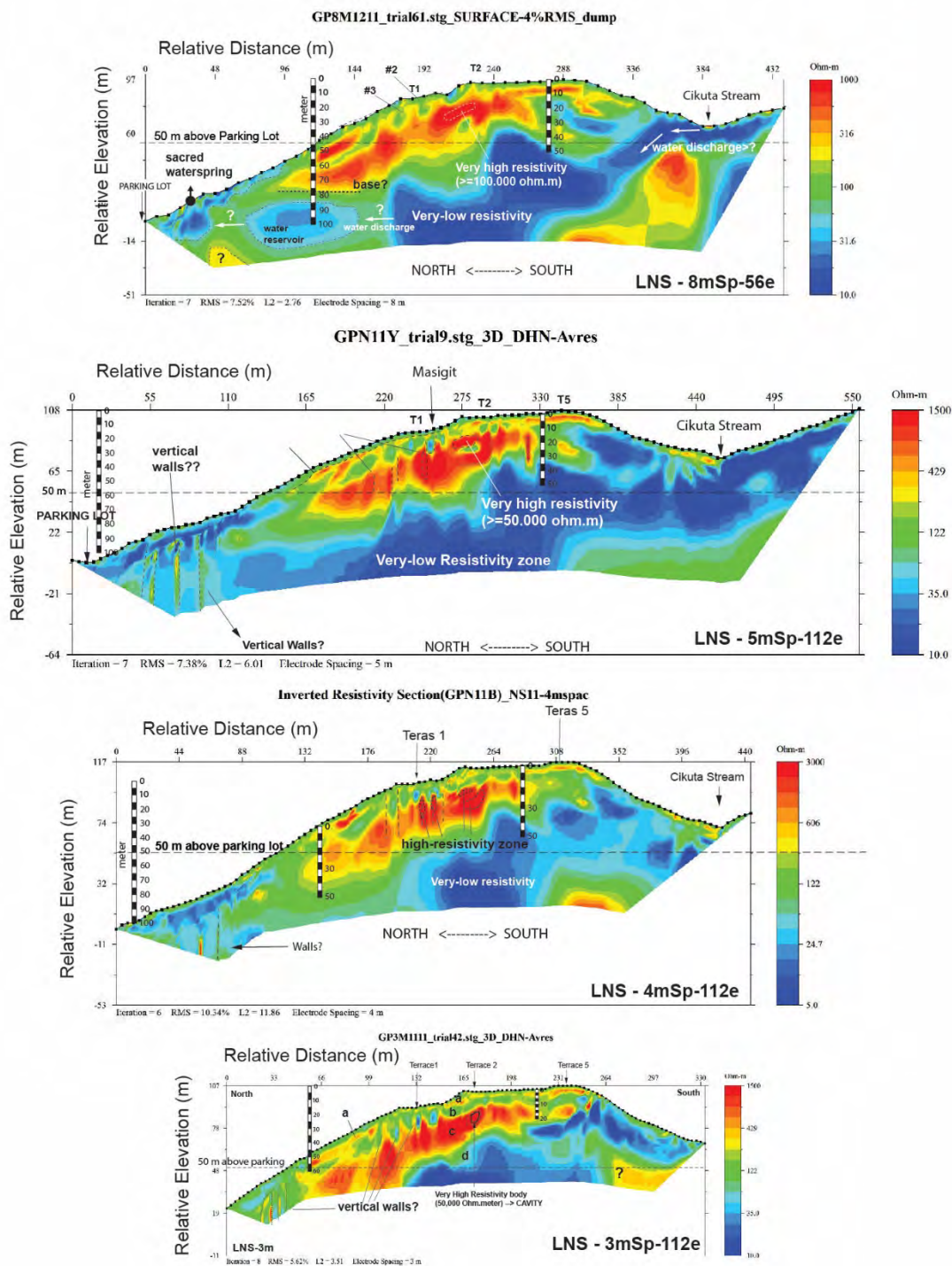
Sup.Figure-F.1. displays the ERT survey conducted using the SuperSting R8 system. (A) The main units of the SuperSting R8 system, along with the switchbox and battery used for powering the survey equipment. (B) The cables utilized for the 3D survey are shown, spread out in four lines. This configuration allowed for comprehensive data collection and imaging of the subsurface. (C) In the 2D survey setup, a cable line with specific spacing is depicted, along with electrode poles positioned at regular intervals.



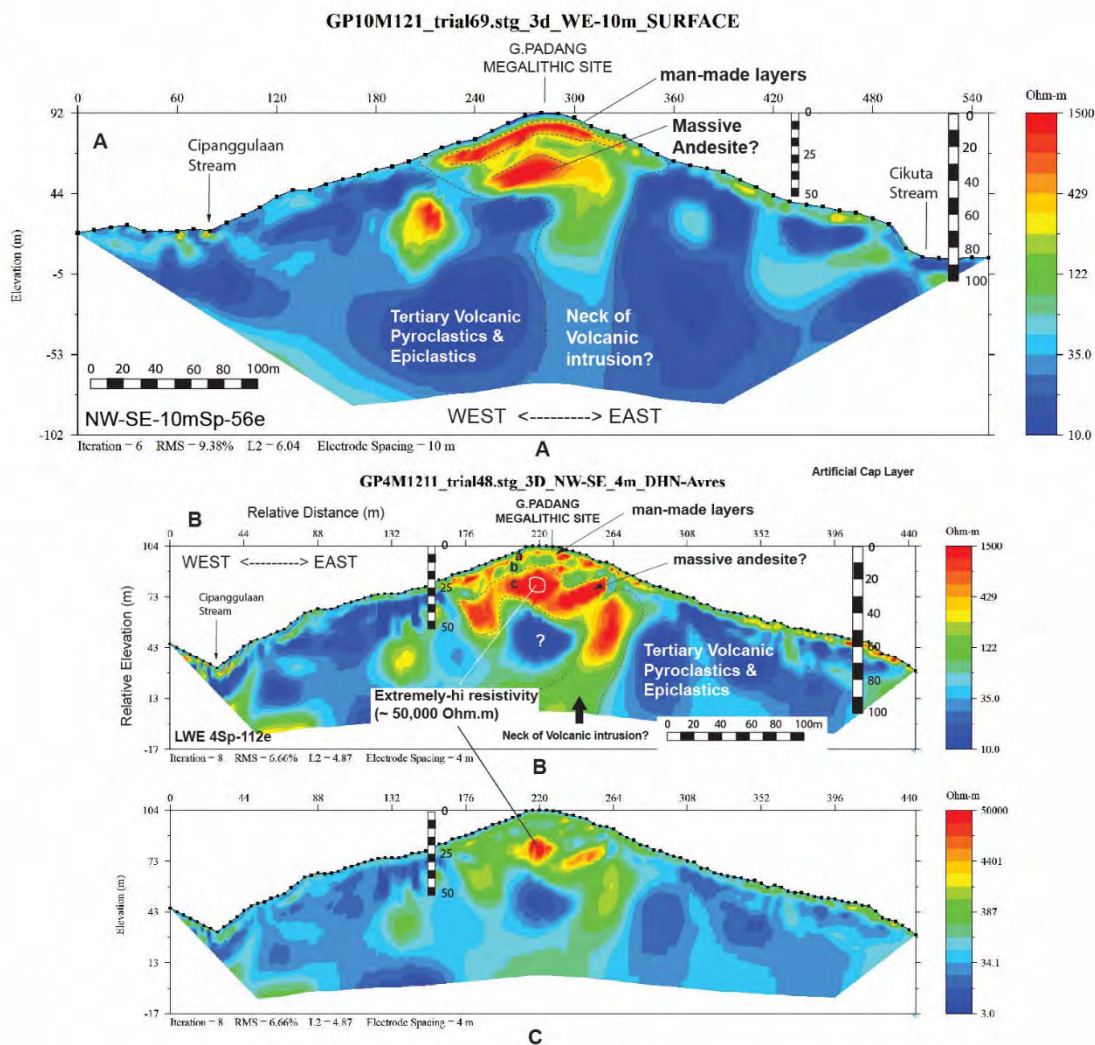
Sup.Figure-F.2. illustrates the principles of ERT processing and modeling: (A) The upper panel showcases the Apparent Resistivity Pseudo section (ARP), which is the result of the ERT 2D survey. In this particular case, a dipole-dipole configuration with a 3-meter spacing electrode was used. The lower panel presents the selected (best) inversion modeling, which represents the reconstructed resistivity model based on the collected data. The middle panel displays the calculated apparent resistivity pseudo section from the inversion model, allowing for a comparison with the actual data. (B) The figure demonstrates the process of setting the best color spectrum to visualize the resistivity structure. By assigning specific colors to different resistivity values, the structure can be effectively visualized, aiding in the interpretation of the subsurface features. (C) The color spectrum of resistivity values can be adjusted for specific purposes. In this example, the color spectrum is set to highlight the presence of an extremely high resistive body (EHRA), which serves as an indicator of a large underground cavity.



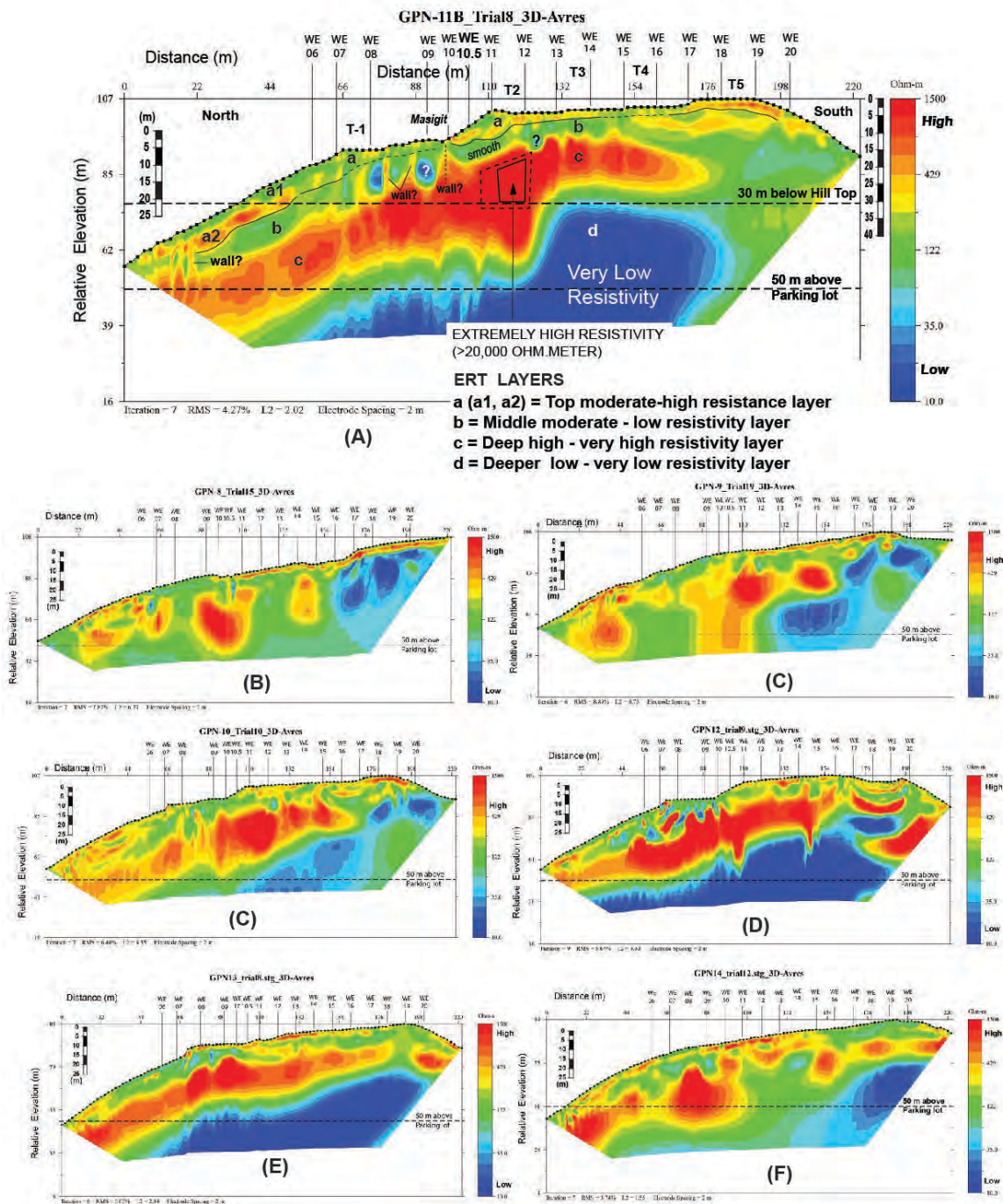
Sup.Figure-F.3. presents the index map of all the 2.5D GRID survey lines conducted for the Electrical Resistivity Tomography (ERT) survey. Various spacing electrodes were used in this study to gather data for the resistivity analysis, allowing for a comprehensive understanding of the subsurface structures.



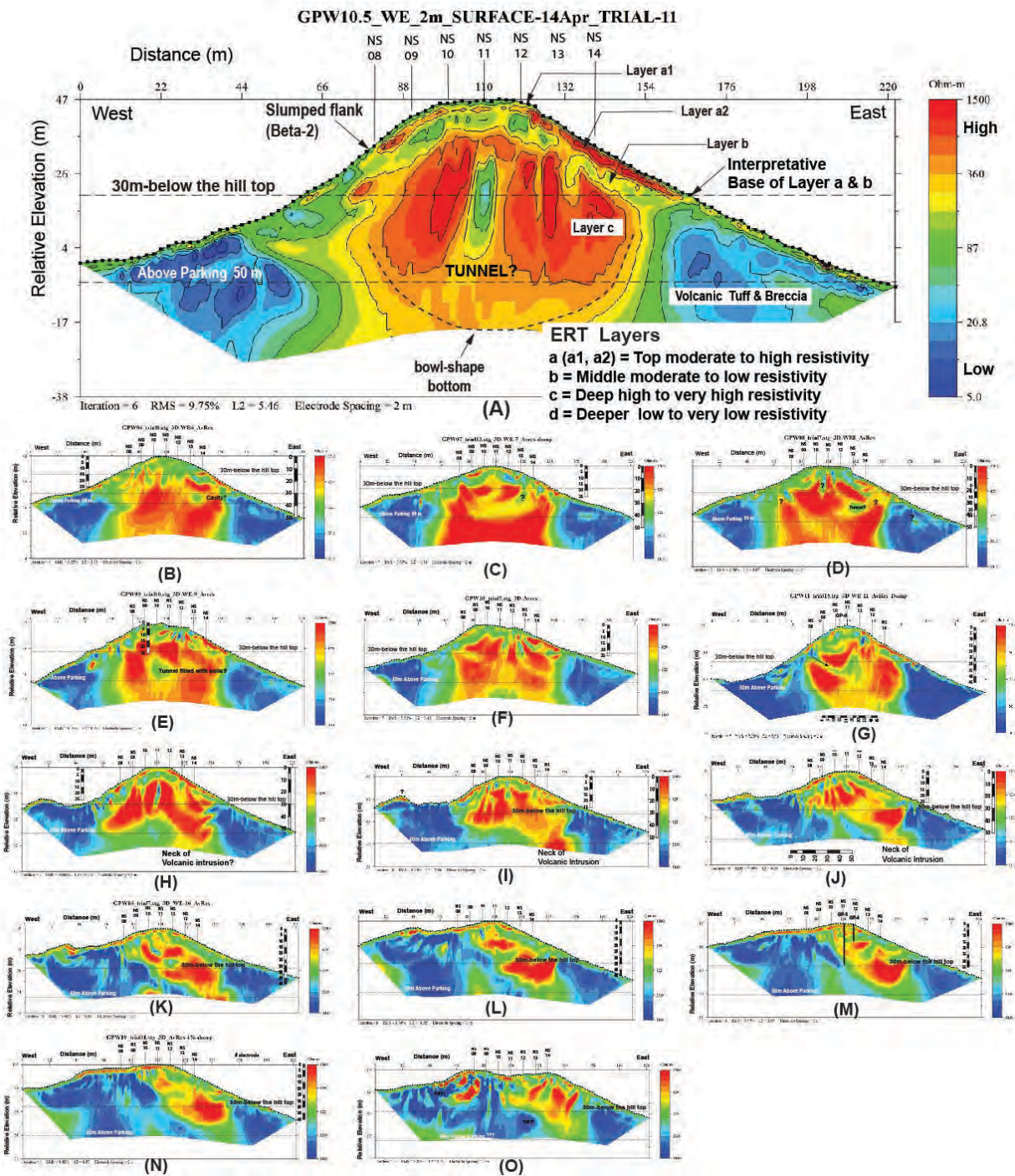
Sup.Figure-F.4. displays the results of 2D resistivity tomography conducted in a north-south direction using different electrode spacing. The figure includes four sub-figures: (A) with 8m spacing, (B) with 5m spacing, (C) with 4m spacing, and (D) with 3m spacing. These sub-figures present the imaging of subsurface resistivity variations along the surveyed profiles with different resolutions and depth of penetrations, providing better insights into the subsurface structures.



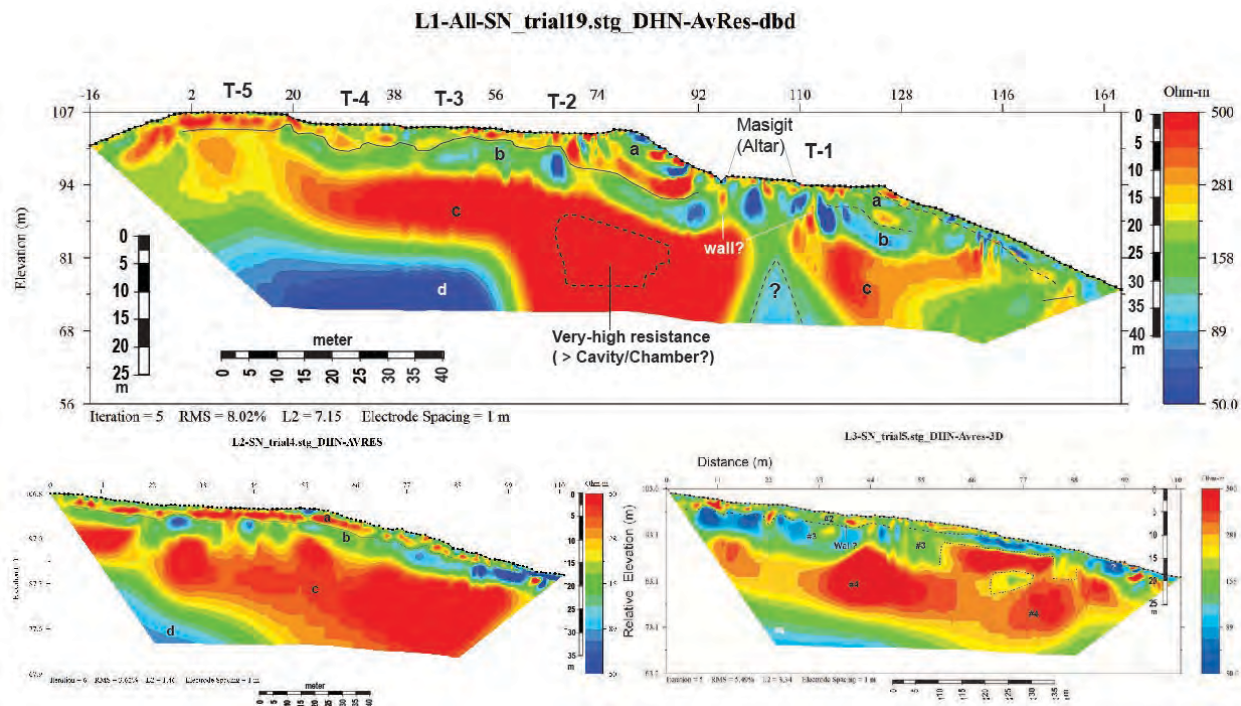
Sup.Figure-F.5. showcases the outcomes of 2D resistivity tomography conducted in both west-east (W-E) and northwest-southeast (NW-SE) directions using larger electrode spacing. The figure consists of three sub-figures: (A) representing the W-E line with a 10m spacing, (B) illustrating the NW-SE line with a 4m spacing, and (C) displaying the same section as in B but with a different color spectrum highlighting the presence of the Extremely-High Resistive Anomaly (EHRA) between the depths of 25 and 30 meters. These sub-figures provide valuable information about the deeper subsurface structures and the detection of the EHRA.



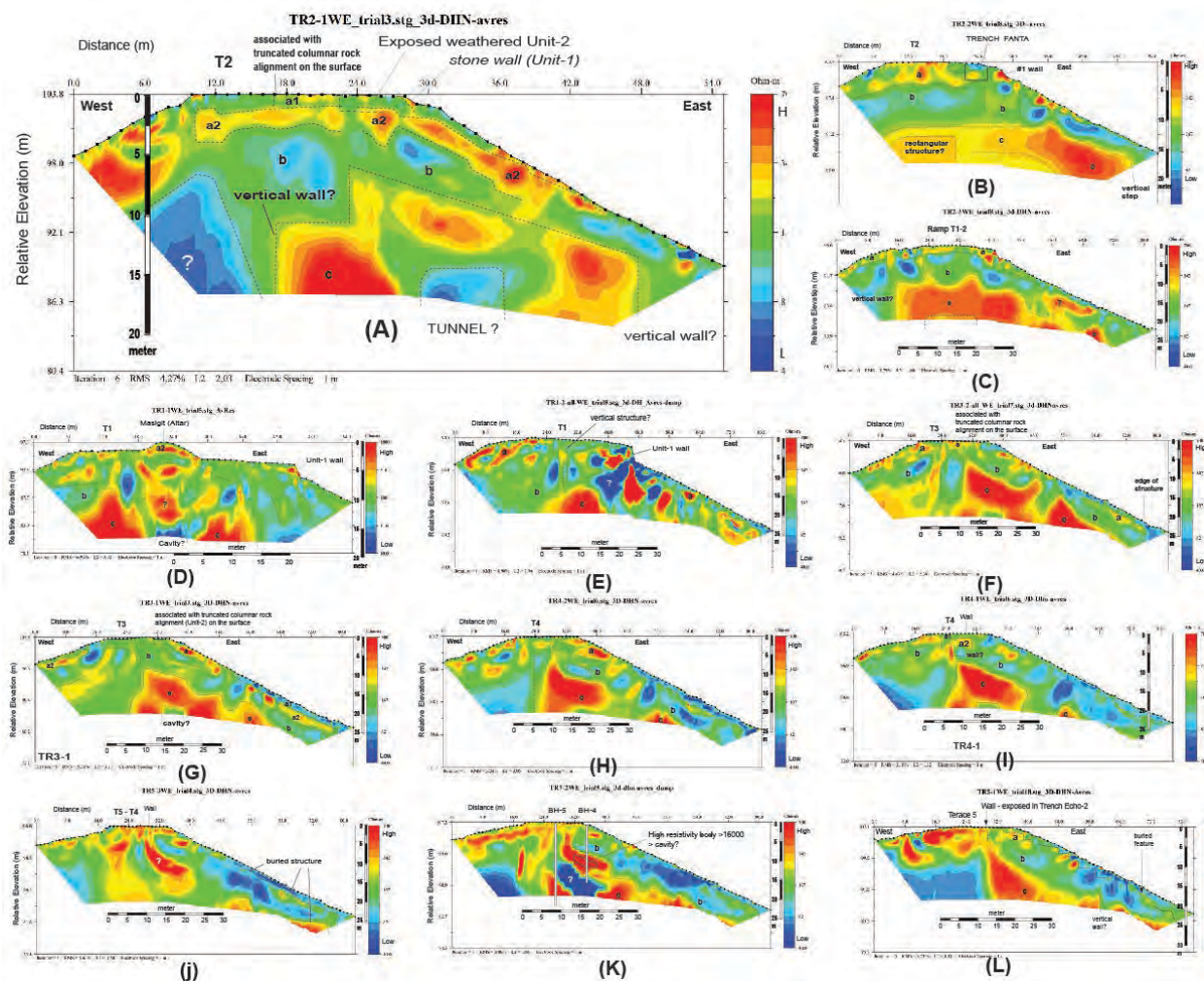
Sup.Figure-F.6. presents the outcomes of the 2.5D gridded Electrical Resistivity Tomography (ERT) survey conducted with 2m spacing electrodes. The figure consists of six sub-figures labeled (A) to (F), which depict the results of the survey lines conducted in the north-south direction. These sub-figures provide valuable insights into the subsurface resistivity variations and help to visualize the geoelectric structure in the surveyed area. The 2.5D gridded ERT survey with 2m spacing electrodes enhance our understanding and allows for a more detailed characterization of the subsurface structures.



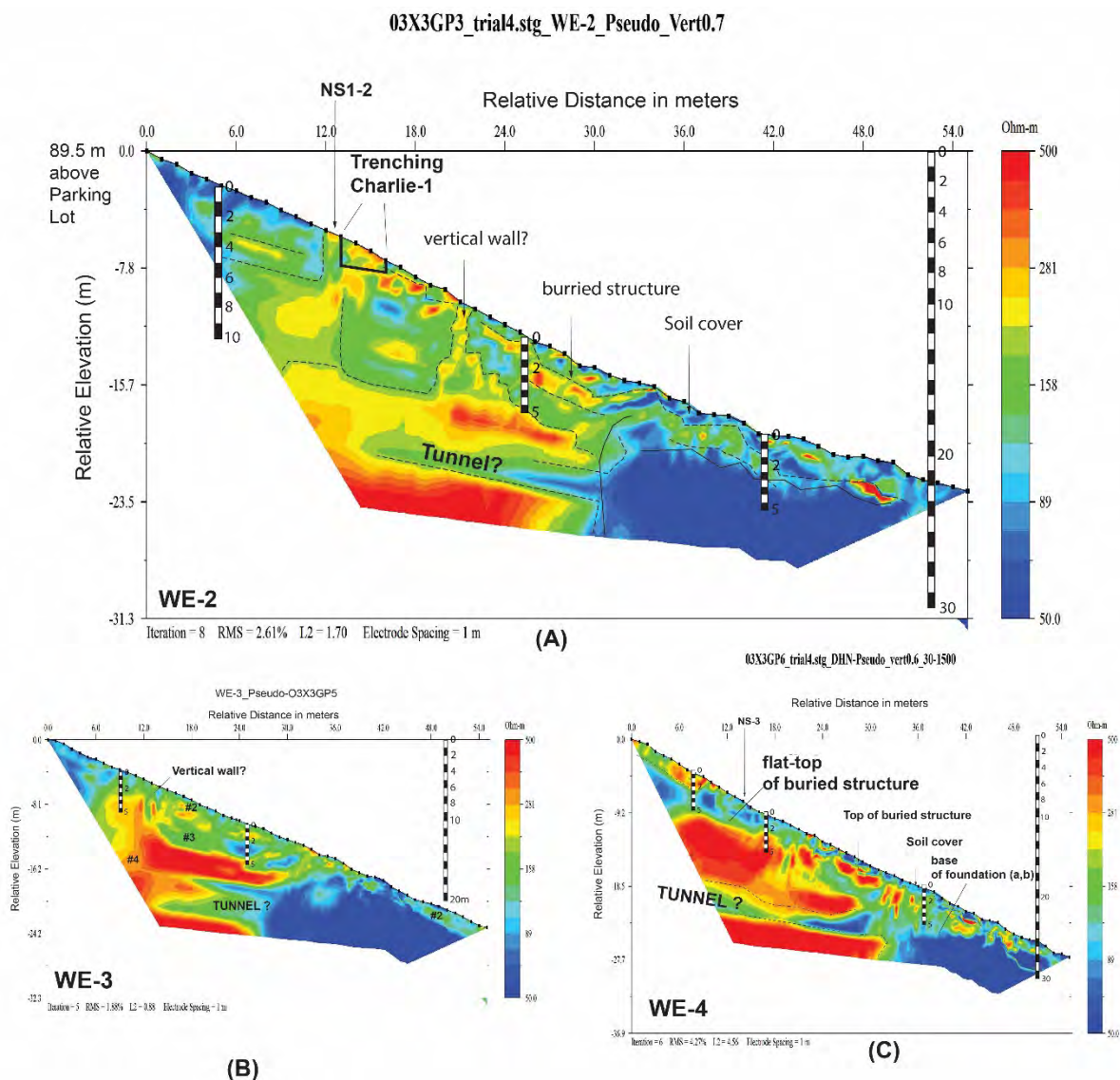
Sup.Figure-F.7. displays the outcomes of the 2.5D gridded Electrical Resistivity Tomography (ERT) survey carried out with 2m spacing electrodes. The figure consists of fifteen sub-figures labeled (A) to (O), which represent the results of the survey lines conducted in the west-east direction.



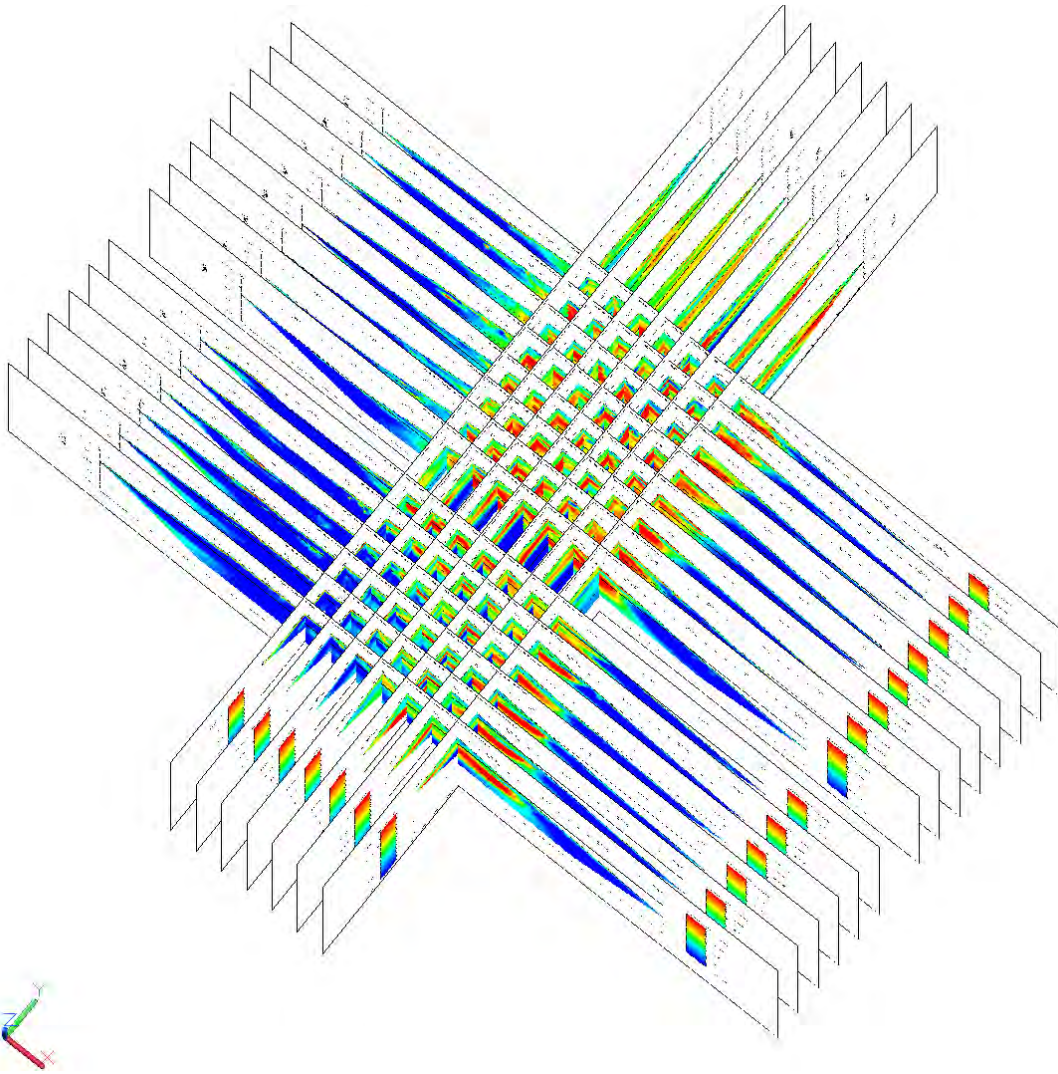
Sup.Figure-F.8. illustrates portions of the 2.5D gridded Electrical Resistivity Tomography (ERT) study conducted with 1m spacing electrodes. The figure focuses on the survey lines carried out in the north-south direction and provides a glimpse into the high-resolution imaging of the subsurface resistivity variations. By employing a closer electrode spacing of 1m, the ERT survey allows for enhanced detail and resolution in capturing the geoelectric structure of the surveyed area. These findings contribute to a more comprehensive understanding of the subsurface characteristics and aid in the interpretation of the geological features in the study area.



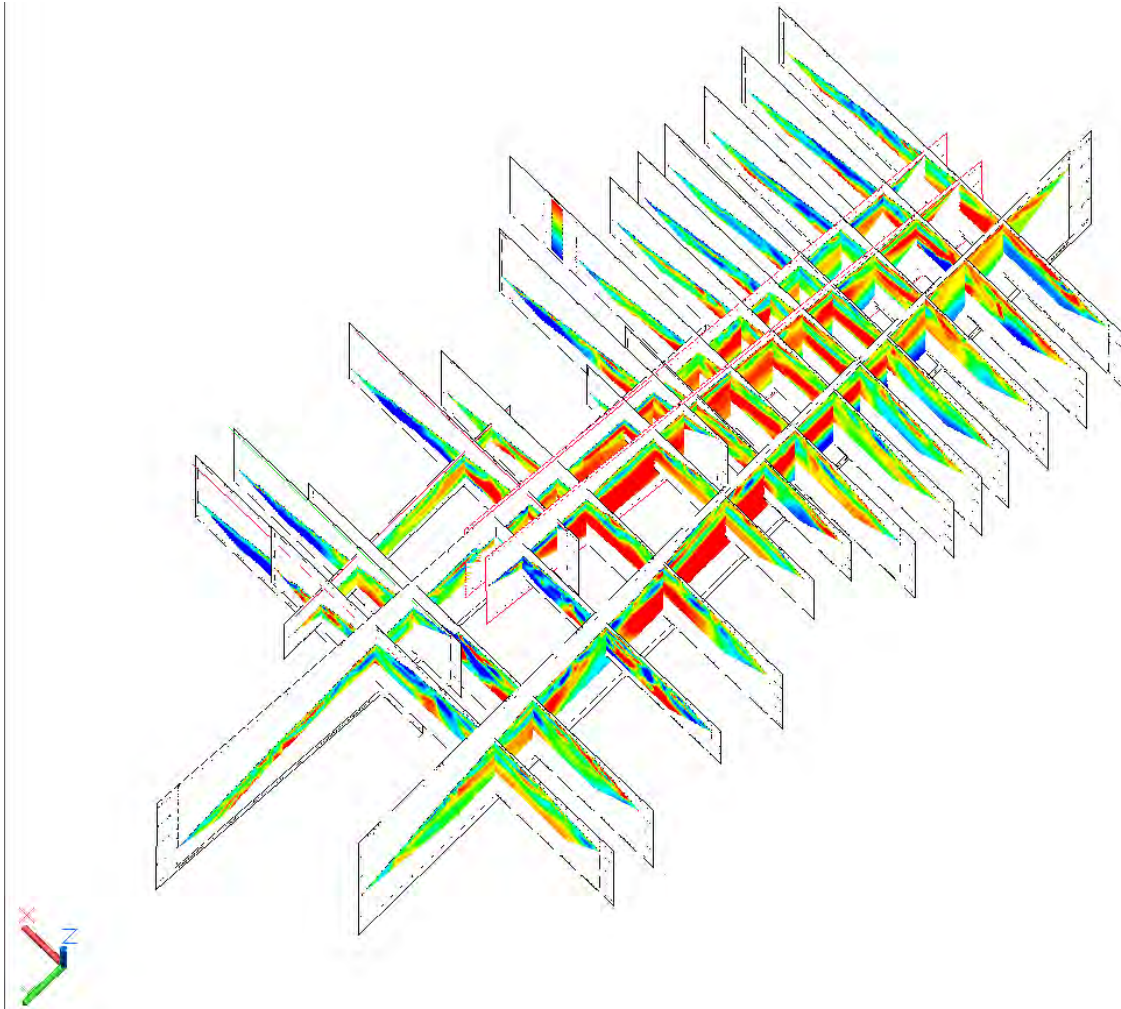
Sup. Figure-F.9. showcases sections of the 2.5D gridded Electrical Resistivity Tomography (ERT) study conducted using 1m spacing electrodes. This figure specifically focuses on the survey lines performed in the west-east direction, providing insights into the detailed imaging of subsurface resistivity variations. By utilizing a close electrode spacing of 1m, the ERT survey enables a higher level of resolution, allowing for more precise characterization of the geoelectric properties in the surveyed area.



Sup.Figure-F.10. presents the outcomes of the Electrical Resistivity Tomography (ERT) survey conducted using a 1m grid spacing electrode configuration on the northeast side flank. The figure showcases detailed imaging of the subsurface structures, providing valuable insights into the geoelectric properties and related subsurface architectures in this specific area of interest. The utilization of a fine grid spacing of 1m enhances the resolution and enables a more comprehensive examination of the subsurface characteristics.



Sup.Figure-F.11. illustrates the process of constructing a 2.5D imaging model using 2D grid survey lines with 2-meter spacing electrodes. The figure showcases the steps involved in integrating multiple 2D surveys to create a comprehensive 2.5D representation of the subsurface. By combining the information obtained from various survey lines, a comprehensive picture of the subsurface structures and their spatial distribution can be achieved. This approach allows for a more accurate interpretation of the subsurface conditions and provides valuable insights into the underground structures of the study area.



Sup.Figure-F.12. demonstrates the process of constructing a 2.5D imaging model using 2D grid survey lines with 1-meter spacing electrodes. This figure highlights the steps involved in integrating multiple 2D surveys with higher electrode density to generate a more detailed and precise representation of the subsurface. By utilizing smaller electrode spacing, the resolution of the imaging improves, allowing for a more accurate characterization of the subsurface structures, boundaries, and anomalies.

SUPPLEMENTARY FIGURE – G SEISMIC TOMOGRAPHY (ST)

Further information on data acquisition and methods

The data acquisition and methods used in this study employed the Fresnel wavepath tomography method and involved specific considerations for the site conditions and Due to the presence of soil on the site surface, geophones (receivers) were placed appropriately on the ground, and sources were also positioned in soil. To generate seismic waves, small firecrackers and sled hammers were used, ensuring the integrity of the megalithic site.

The Fresnel wavepath tomography method utilizes a simple sinc basis function, represented by Equation (1), which combines ray path and inverse scattering tomography principles.

$$L_{\text{wavepath}} = \text{sinc}(2\pi f \cdot \Delta\tau) \quad (1)$$

This method calculates the interpolated Fresnel zone wavepath, denoted as L_{wavepath} , using travel times, $\Delta\tau$, from the source to a point (t_{sr}), travel times from the receiver to a point (t_{rg}), and the travel time from the source to the receiver (t_{sg}). The frequency of the wave is denoted as f .

$$(t_{\text{sg}}), \Delta\tau = t_{\text{sr}} + t_{\text{rg}} - t_{\text{sg}} \cdot f$$

This areal wavepath is called the first Fresnel zone wavepath when the first Fresnel zone restriction is applied. The first Fresnel zone restriction is expressed by equation (2). So, L_{wavepath} becomes 0 when it does not fulfill equation (2).

$$\Delta\tau \leq \frac{1}{2f} \quad (2)$$

The inversion is done by using the slowness updating formula expressed in equation (3).

$$\Delta p_{\text{avr}}(r)_k = \frac{\sum_{i=\text{wavepath number}} \Delta p(r)_i}{\sum_{i=\text{wavepath number}} W(r)_i} \quad (3)$$

Δp_{avr} is slowness updated at each iteration. Where $\Delta p(r)$ and $W(r)$ are expressed in equations (4) and (5), respectively.

$$W(r) = \begin{cases} L_{\text{wavepath}}(r), L_{\text{wavepath}}(r) > 0 \\ 0, L_{\text{wavepath}}(r) \leq 0 \end{cases} \quad (4)$$

$$\Delta p(r) = \frac{dL_{\text{wavepath}}(r) \Delta t(s|g)}{\sum_r d^2 L_{\text{wavepath}}^2(r)} \quad (5)$$

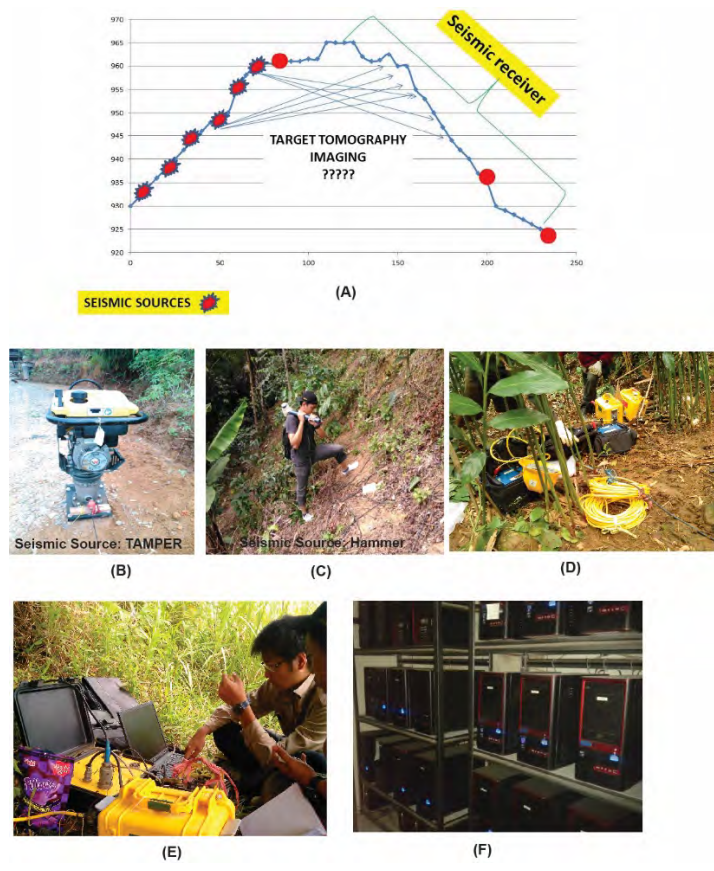
d denotes cell size and $\Delta t(s|g)$ denotes the difference between $t_{\text{observation}}$ and $t_{\text{calculation}}$. The summation in equation (5) is performed to whole area (r).

Wideband Fresnel zone wavepath tomography employs frequency sweeping during the inversion process, starting from the lowest suitable frequency to the highest suitable frequency. This technique accounts for the different characteristics of low-frequency and high-frequency wavepaths. Inversions begin with large and dominant subsurface anomalies and gradually provide more detailed information about smaller anomalies.

The wideband Fresnel wavepath tomography technique yields stable results, and previous studies have demonstrated its accuracy. The frequency sweeping procedure considers seismic field data spectra as polychromatic, rather than monochromatic. Wavelets are finite in the time domain, resulting in frequency spectra represented as a distribution of broad spectra rather than a single spike. This approach allows for the representation of wideband spectra, which closely resembles the natural behavior of seismic waves.

The inversion algorithm for wideband Fresnel zone wavepath tomography follows the following steps: (1) In the initial iteration, the observation travel times are inverted by the first Fresnel zone wavepath tomography with an initial frequency (f_0), (2) In subsequent iterations, the frequency is increased by Δf (equation (6)). and the inversion is performed using the updated frequency. The frequency is gradually swept from the lowest to the highest frequencies within the frequency band.

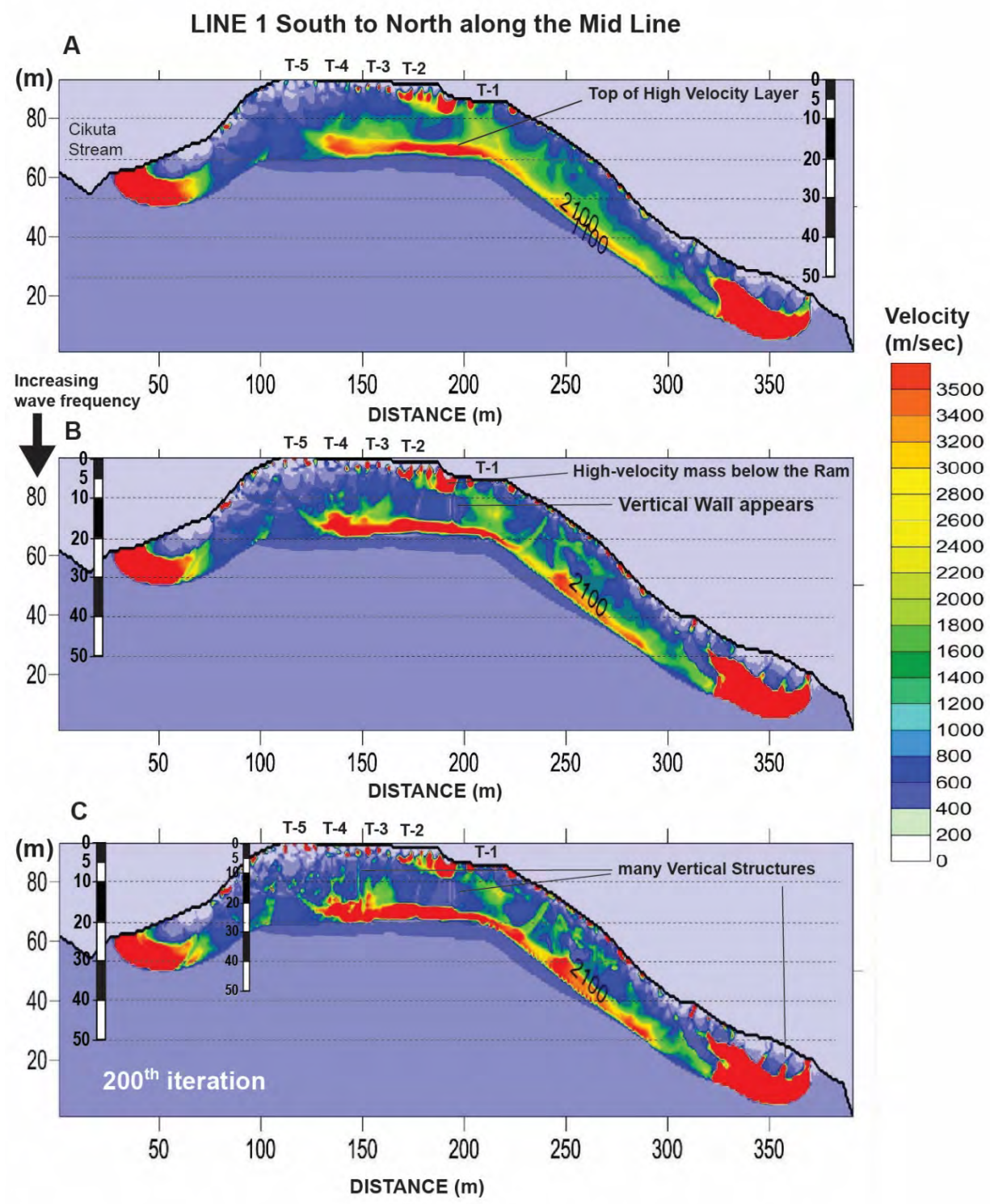
$$\Delta f = \frac{\text{Bandwidth}}{\text{total number of iteration} - 1} \quad (6)$$



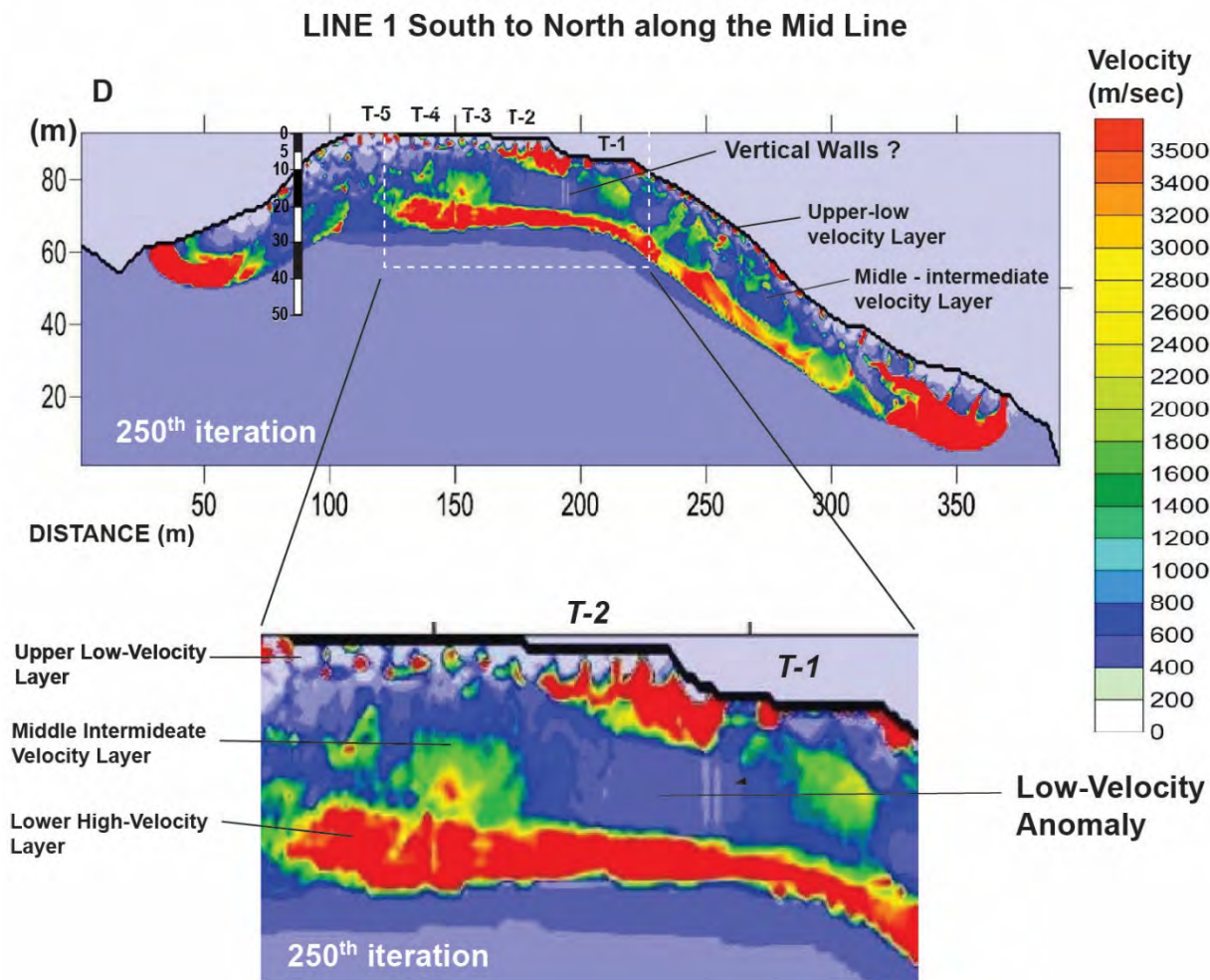
Sup.Figure.G.1. The equipment used in the seismic tomographic survey conducted in this study. (A) Seismic sources and geophones spaced at 5m intervals. Survey Line-2 provided a large aperture angle for seismic tomographic imaging. (B&C) Seismic sources. (D) Seismometer and battery. (E) Main unit. (F) Parallel computer for data processing.



Sup.Figure.G.2. Index map showing the survey lines for the seismic tomography survey.

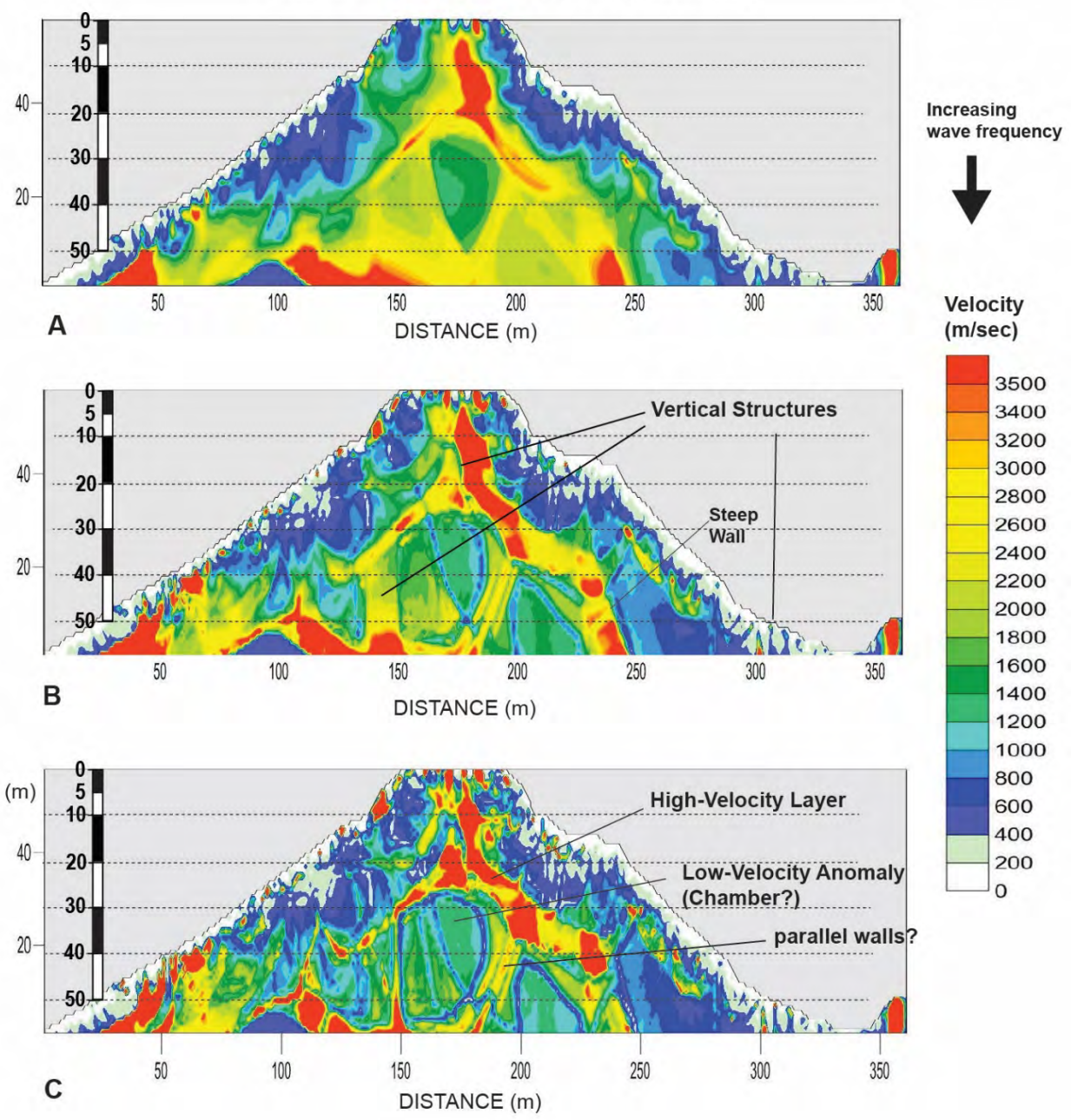


Continued to the next page...

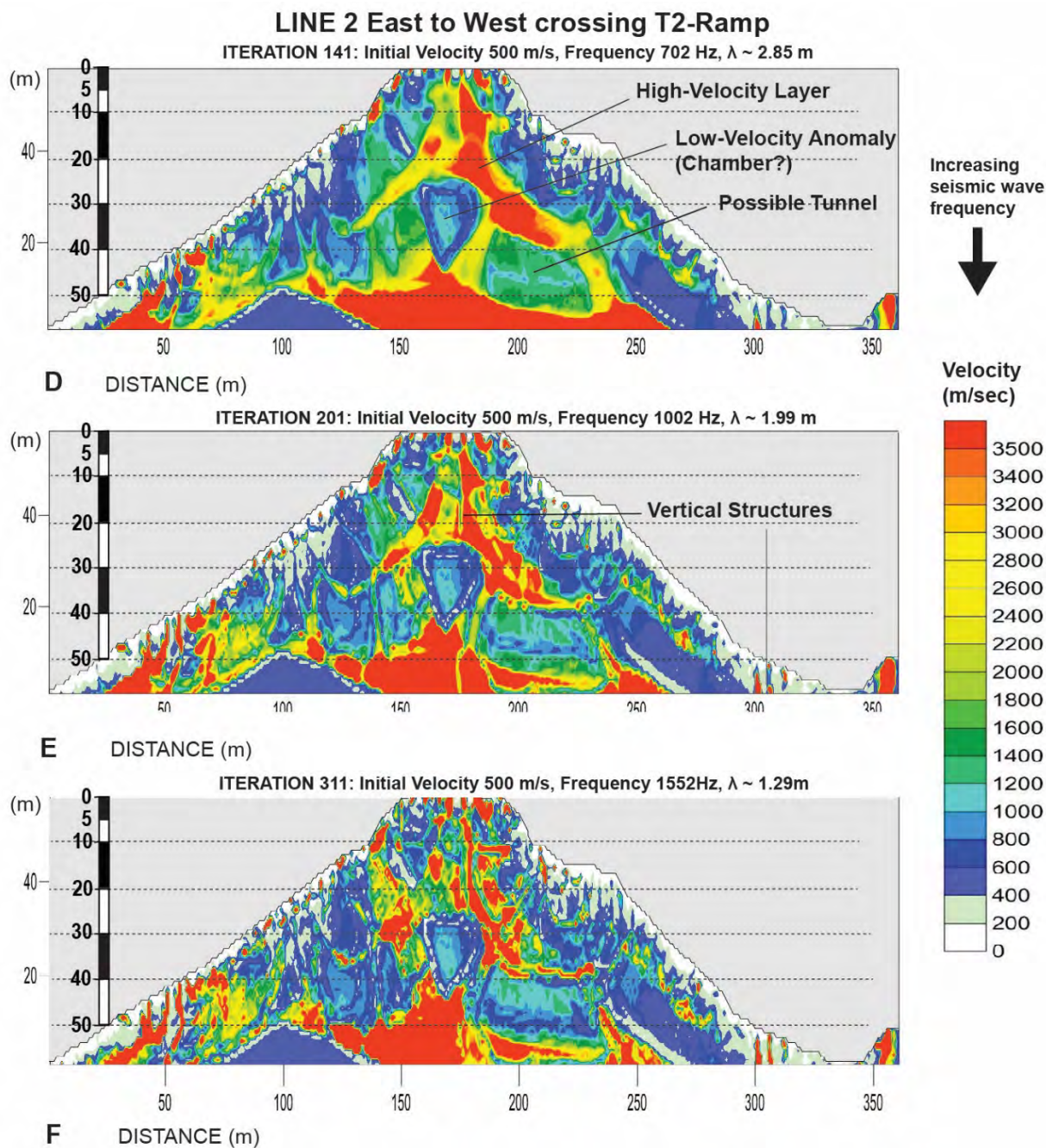


Sup.Figure.G.3. Seismic Tomographic North-South Section (Line-1) through the longitudinal section of the megalith stone terraces. A, B, C, and D represent the ST inversion models using different seismic wave frequencies as input. The vertical structures observed in the tomogram are actual objects and not a result of artificial processing. The zoomed-in Figure D provides a closer look at the stratifications in the seismic tomogram.

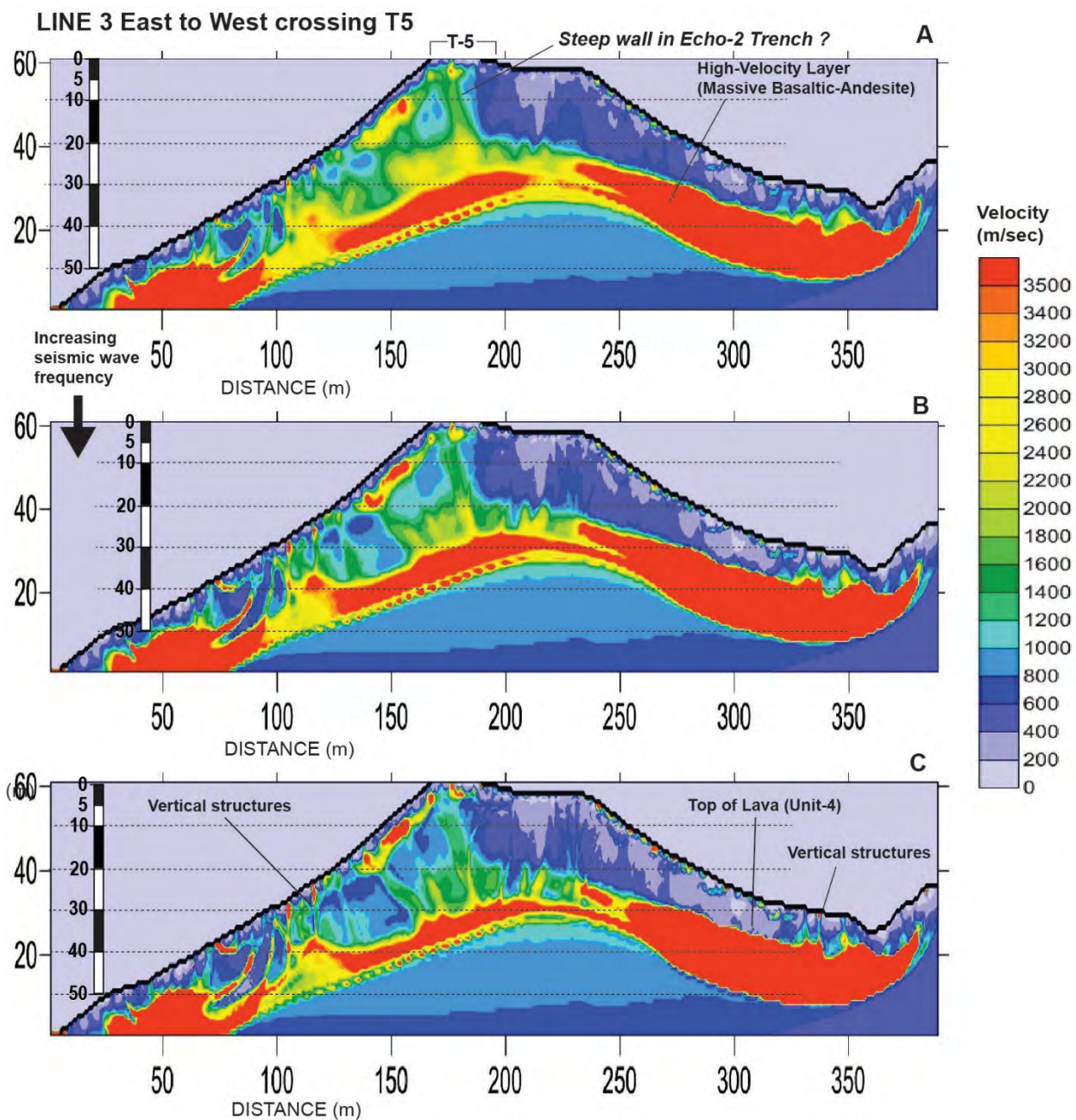
LINE 2 East to West crossing T2-Ramp



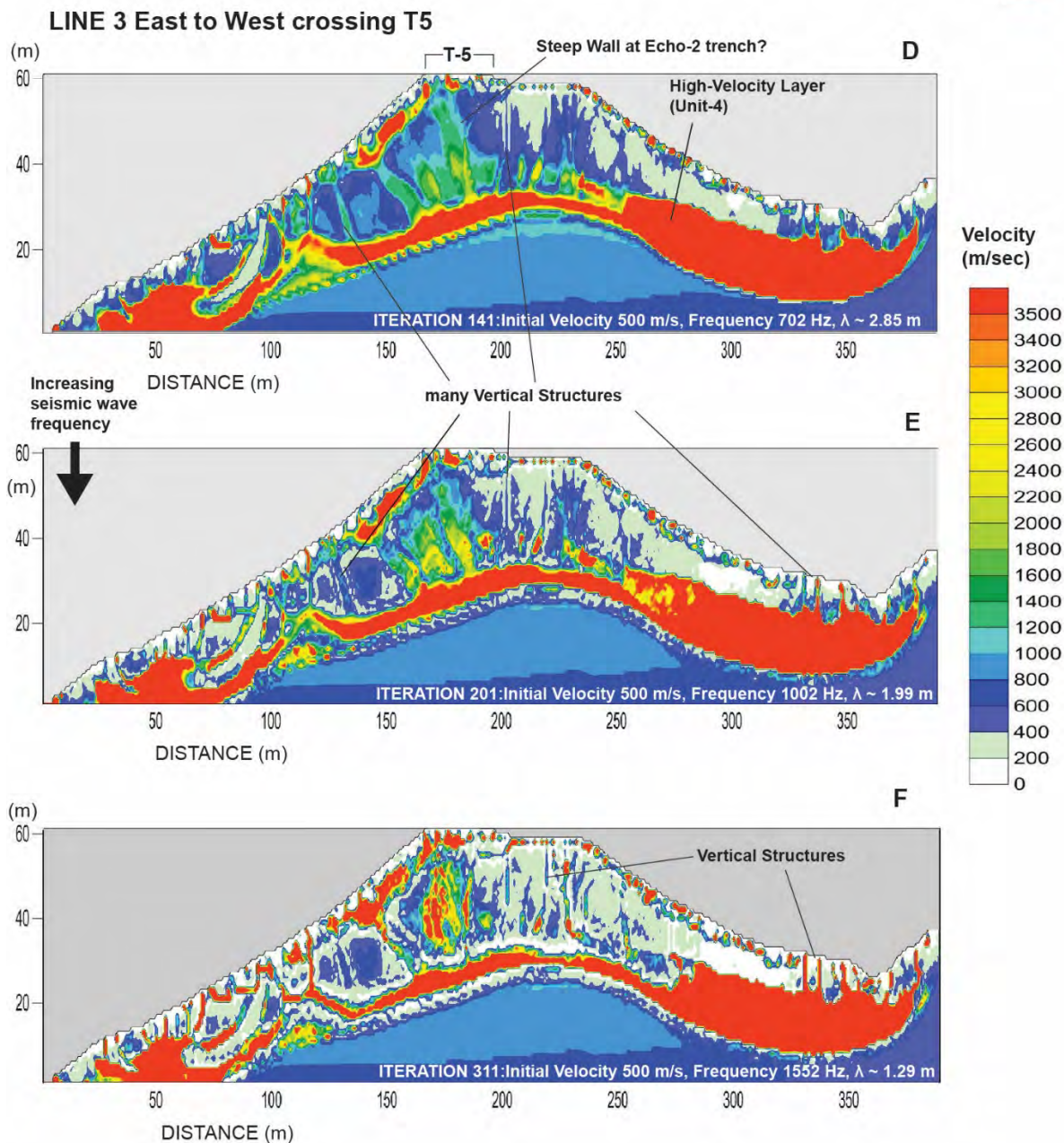
... CONTINUED TO NEXT PAGE



Sup.Figure.G.4. Seismic Tomographic East-West Line-2 cross-section through the center of Terrace 2 and the Ramp. A to F represent the results of ST inversion modeling using different seismic wave frequencies. All alternative models exhibit a consistent basic structural geometry. The presence of High-Velocity Layers, the Low-Velocity Anomaly, and the prominent vertical or upright structures are observed in all models.

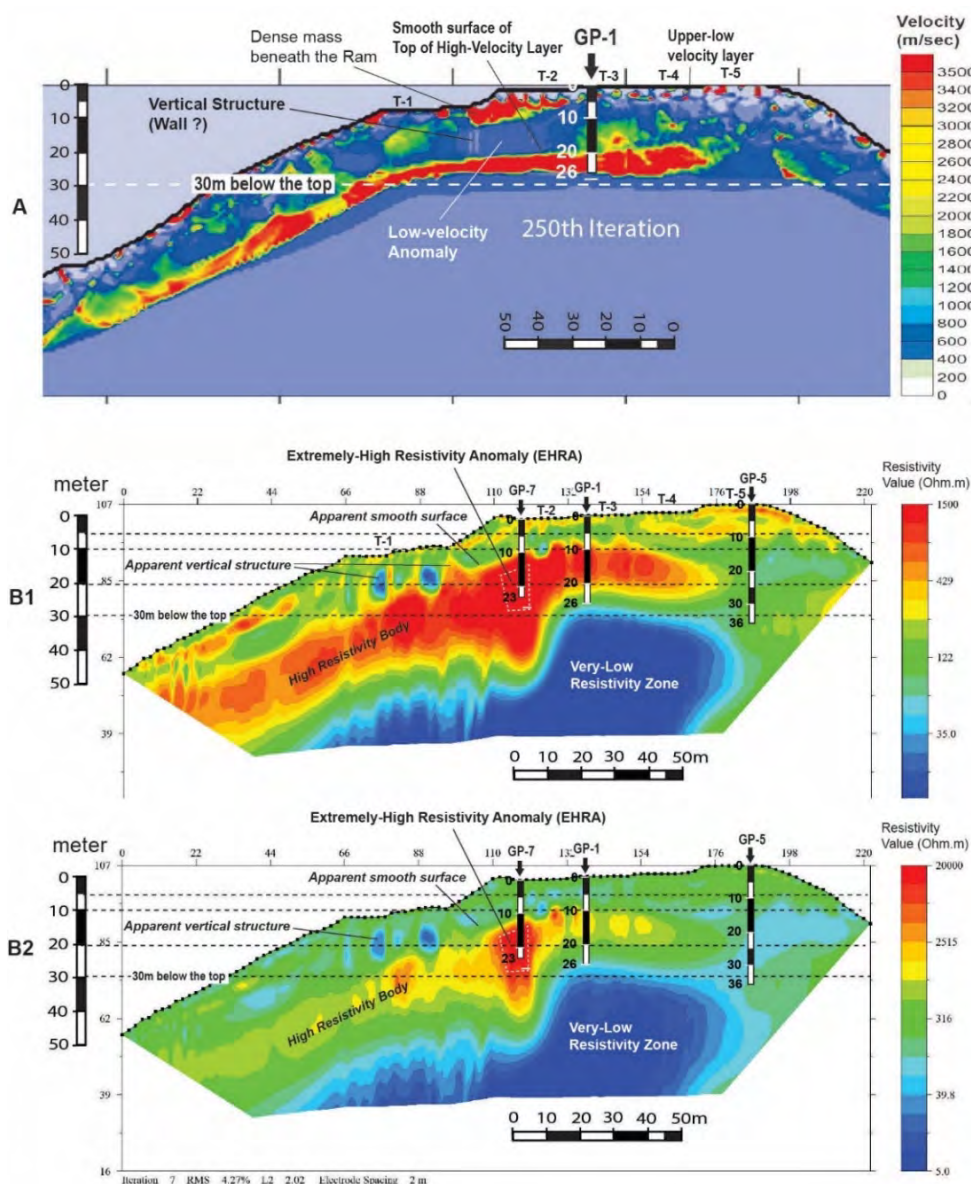


----- CONTINUED TO NEXT PAGE

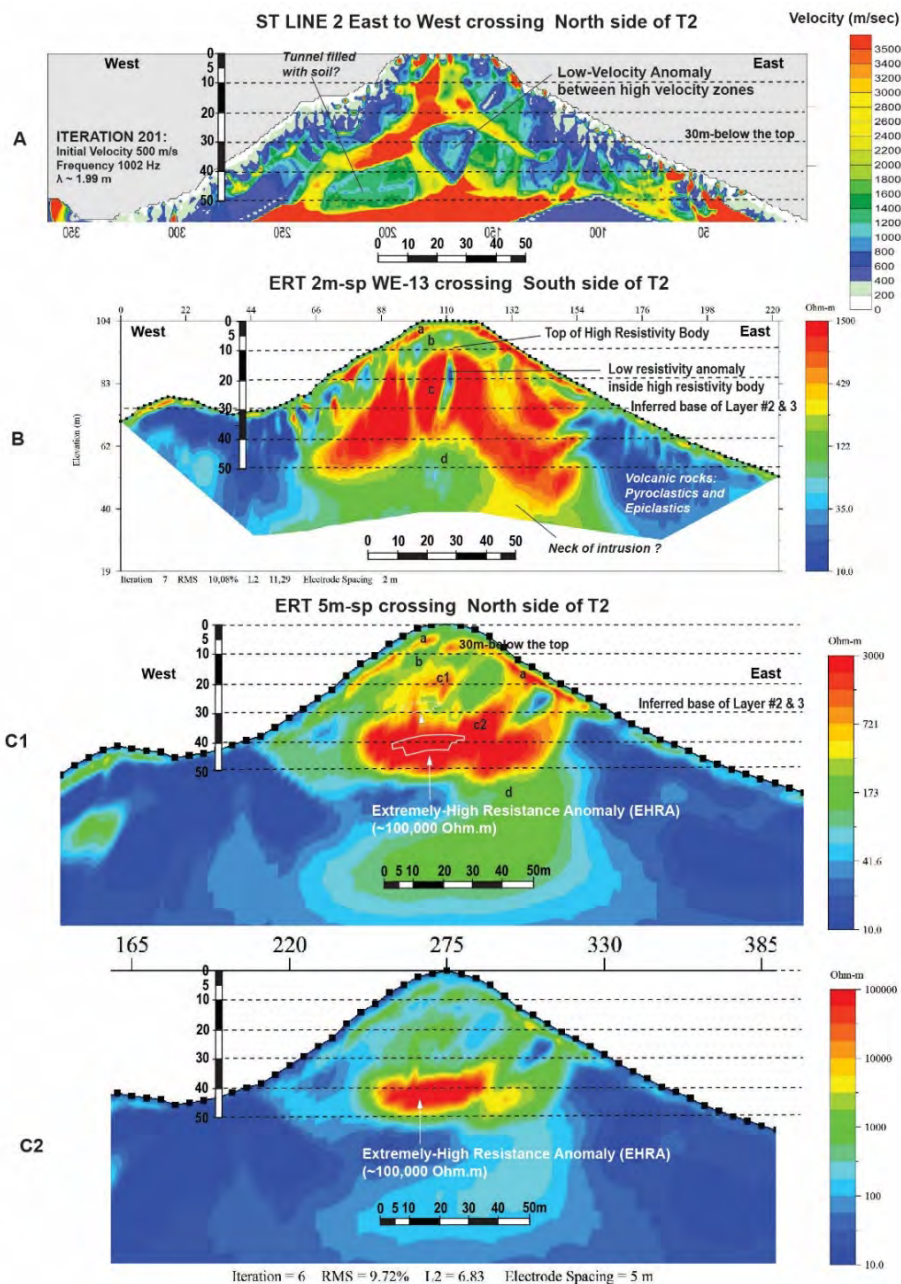


Sup.Figure.G.5. Seismic Tomographic Line-3 East-West cross-section through the southernmost terrace (T-5). A to F represent the results of ST inversion modeling using different seismic wave frequencies.

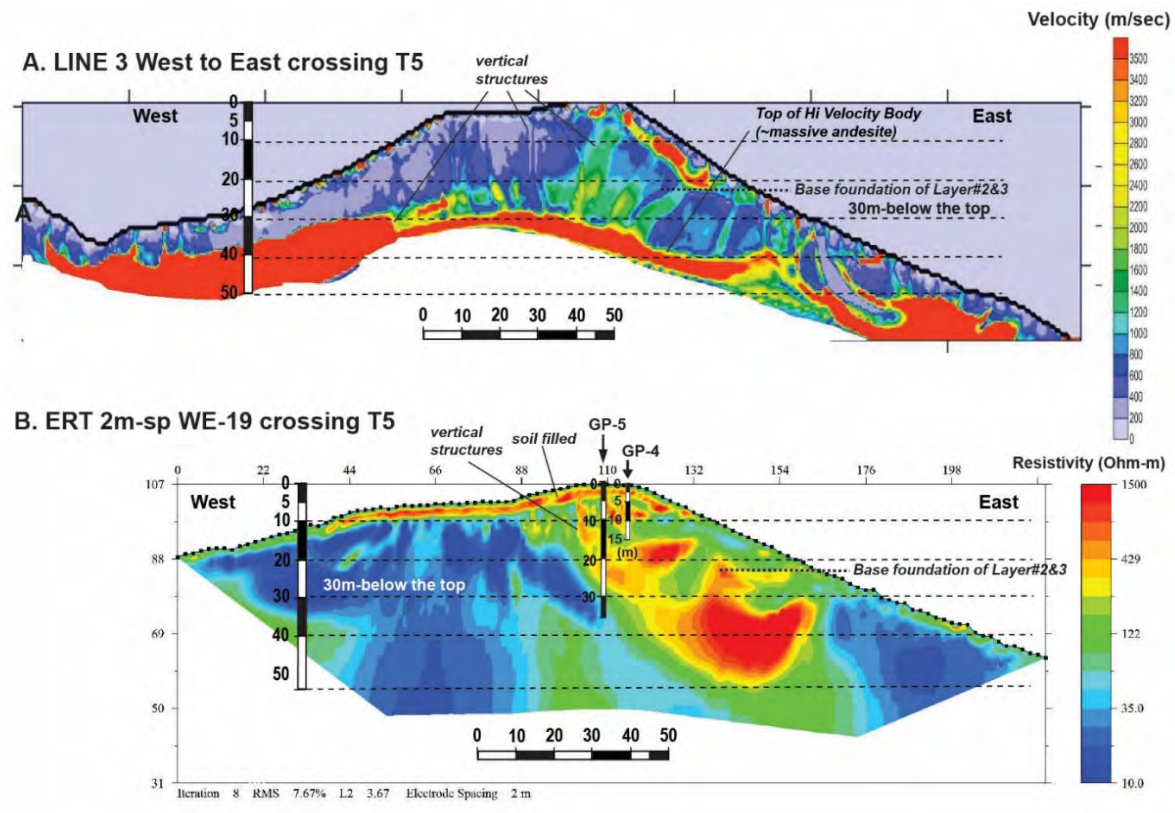
SUPPLEMENTARY FIGURE – H. DATA INTEGRATION AND ANALYSIS



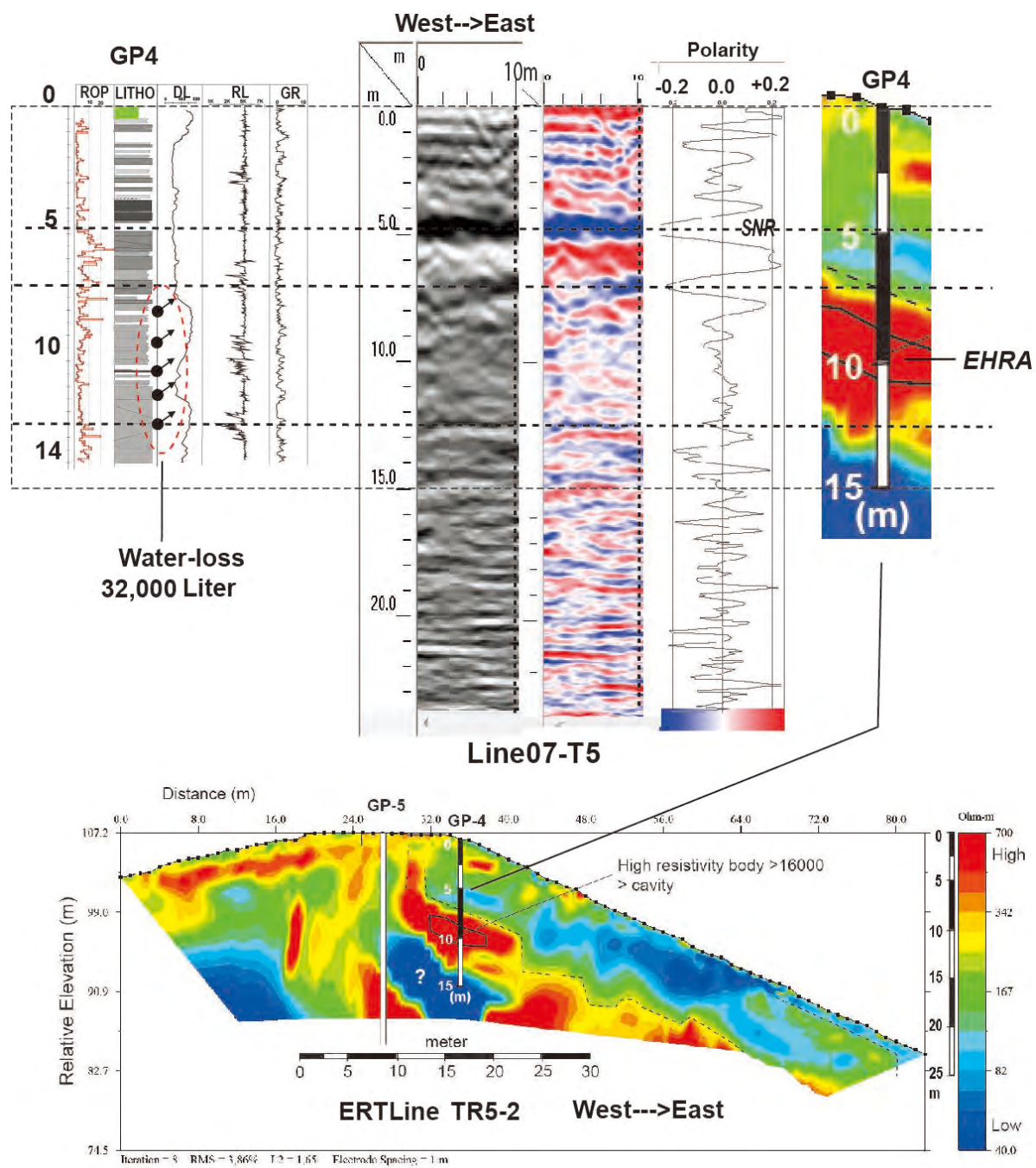
Sup.Figure-H.1. Comparison between the North-South Seismic Tomography (ST) and Electrical Resistivity Tomography (ERT) profiles. Both profiles exhibit a similar basic geometry but may not show identical layers. The top of the high-velocity layer, representing the top of the massive andesite rocks, does not necessarily coincide with the top of the high-resistive layer. The Extremely High Resistive Anomaly (EHRA) indicates the presence of a large cavity/chamber not only within the High-Velocity layer (Unit-4) but also within the lower part of the Intermediate Velocity layer (Lower part of Unit 2). Vertical structures are observed in both the ST and ERT sections.



Sup.Figure-H.2. Comparison between the East-West Seismic Tomography (ST) and Electrical Resistivity Tomography (ERT) profiles with different resolutions or electrode spacings. A. Line-2 ST section revealing a low-seismic velocity anomaly (LVA). B. WE-13 ERT section with 2m spacing electrodes displaying a low-resistance within a high-resistance layer, potentially indicating the presence of a chamber or tunnel filled with soil. C1. ERT section with 5m spacing using a color spectrum to visualize internal structures. C2. The same ERT section with a high-range color table highlighting the Extremely High Resistive Anomaly (EHRA). The EHRA observed in ERT corresponds to the LVA observed in ST, both suggesting the existence of a large cavity or chamber.

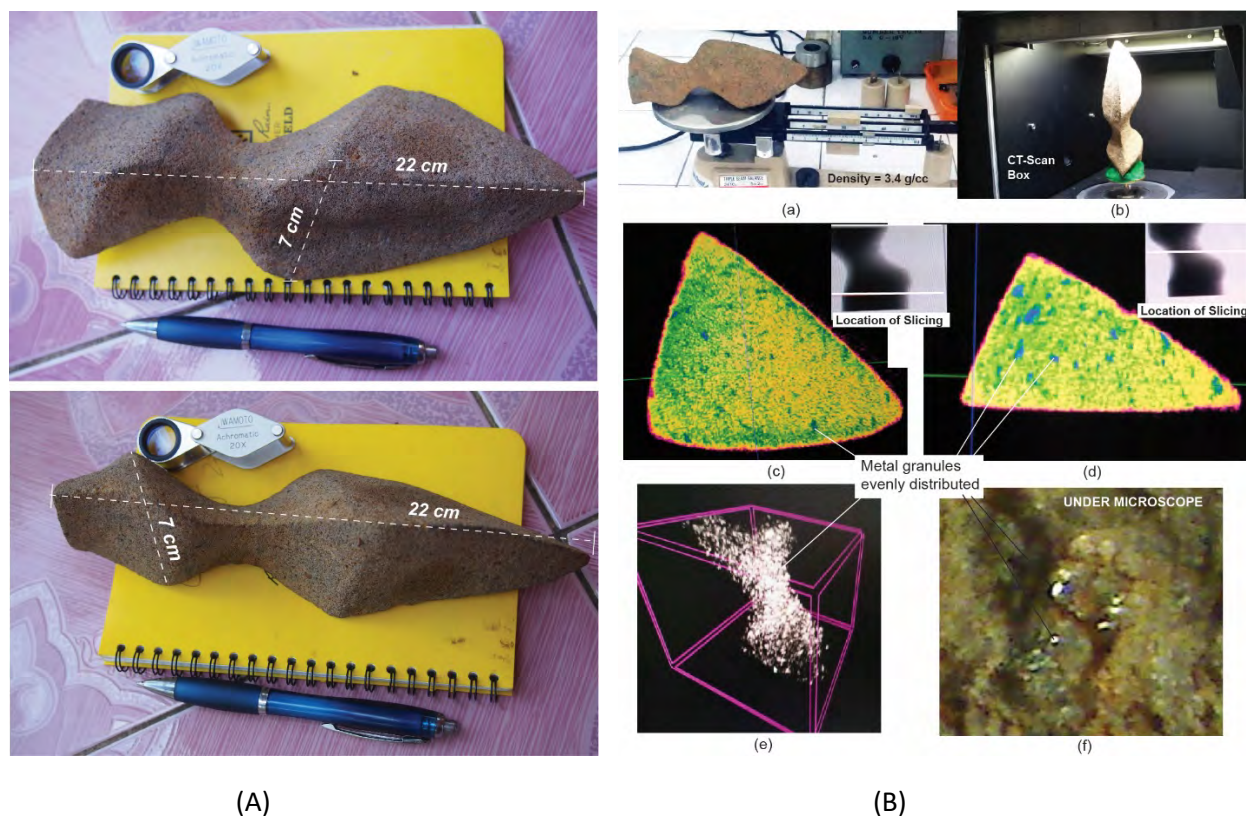


Sup.Figure-H.3. Comparison between Seismic Tomography (ST) Line-3 and Electrical Resistivity Tomography (ERT) Line WE-19, both crossing through T-5. It is noteworthy that the high-velocity layer representing the massive basaltic-andesite rock, which is clearly imaged in the ST section, appears 'invisible' in the ERT section. This phenomenon may be attributed to water saturation caused by high-pressured artesian water.



Sup.Figure-H.4. Comparison between borehole log data from GP4 and the corresponding radargram and ERT section. The significant water loss observed during the GP4 drilling is associated with the presence of an Extremely High Resistive Anomaly (EHRA).

SUPPLEMENTARY FIGURE – I GUNUNG PADANG STONE ARTIFACTS



Sup. Figure-I.1. The Kujang Stone artifact, discovered in the Echo-1 trench, positioned on top of Unit 3 and buried beneath ancient soil deposits. (A) The artifact displays a distinctive geometry, with relative sizes that exhibit a connection to the golden ratio, phi (i.e., $\pi = 22/7$). (B) Analysis of the Kujang Stone in the Physics Lab: (a) Measurement of volume, pores, and density is 3.4 grams/cm³. Significantly heavier than the density of andesite, which typically ranges from 2.4 to 2.8 grams/cm³. (b) CT-scan for tomography scanning, (c) Illustration of a tomography slice revealing a 'twisted' triangular shape, (d) Tomography slice of the artifact's neck, (e) Tomography scanning process, (f) Microscopic view exhibiting abundant granular metals.



(a)



(b)



(c)



(d)



(e)



(f)

Sup. Figure-I.2. Artifacts displaying sharp-tool incisions/nicks. (a)-(d) A large stone artifact in the shape of a *Kujang*, discovered on the surface of the east slope. (e)-(f) Other stone artifacts exhibiting incisions made by sharp tools.



Sup. Figure-I.3. Unusual marks/symbols were observed on the columnar rocks. Further analysis is required to distinguish between natural and artificial markings.

SUPPLEMENTARY FIGURE – J. SELECTED PETROGRAPHY ANALYSIS

1. Sample No. GP-01; 2.85 m (*core from GP-1 Borehole at 2.85 m depth*)

STEREOSCOPIC CHARACTERISTIC

Field Name : Pyroxene Basalt
 Nature of Sample : Small core sample
 Minerals Visible : Feldspars, pyroxene, chlorite, and opaques.
 Texture : Porphyritic (\varnothing 0.5-1.2mm) in very fine grained, slightly oriented groundmass
 Colour : Dark grey - black
 Grain Size : Fine grained
 Other Comments : This weakly microfractured volcanic rock appears under a binocular microscope and hand lens to be a slightly metasomatically altered pyroxene basalt.

MICROSCOPIC CHARACTERISTICS

Constituents : (Percent visual estimate)

This slightly altered basalt displays porphyritic texture consisting of phenocrysts feldspar and mafic minerals (0.5-1.2mm) set in slightly oriented glassy matrix and cryptocrystalline.

25% Plagioclase is represented by bytownite colorles, occurs as phenocrysts (0,3-1,2mm) and groundmass. Some of the phenocrysts retain lath shaped crystal with An₇₅. Part of this mineral are zoned, interlocking and slightly oriented tabular. Evidence of rare sericitic alteration of bytownite can be seen in places.

15% Mafic mineral is mainly represented by clino-pyroxene of augite and scarcely ortho-pyroxene of hypersthene that partly slightly altered to very fine aggregates of sericite, chlorite and iron oxide. Most of this mineral present as primary igneous origin respectively, occur in about equal abundance as fine tabular and prismatic euhedral.

5% Opaque minerals are sparsely disseminated and represented mostly by magnetite.

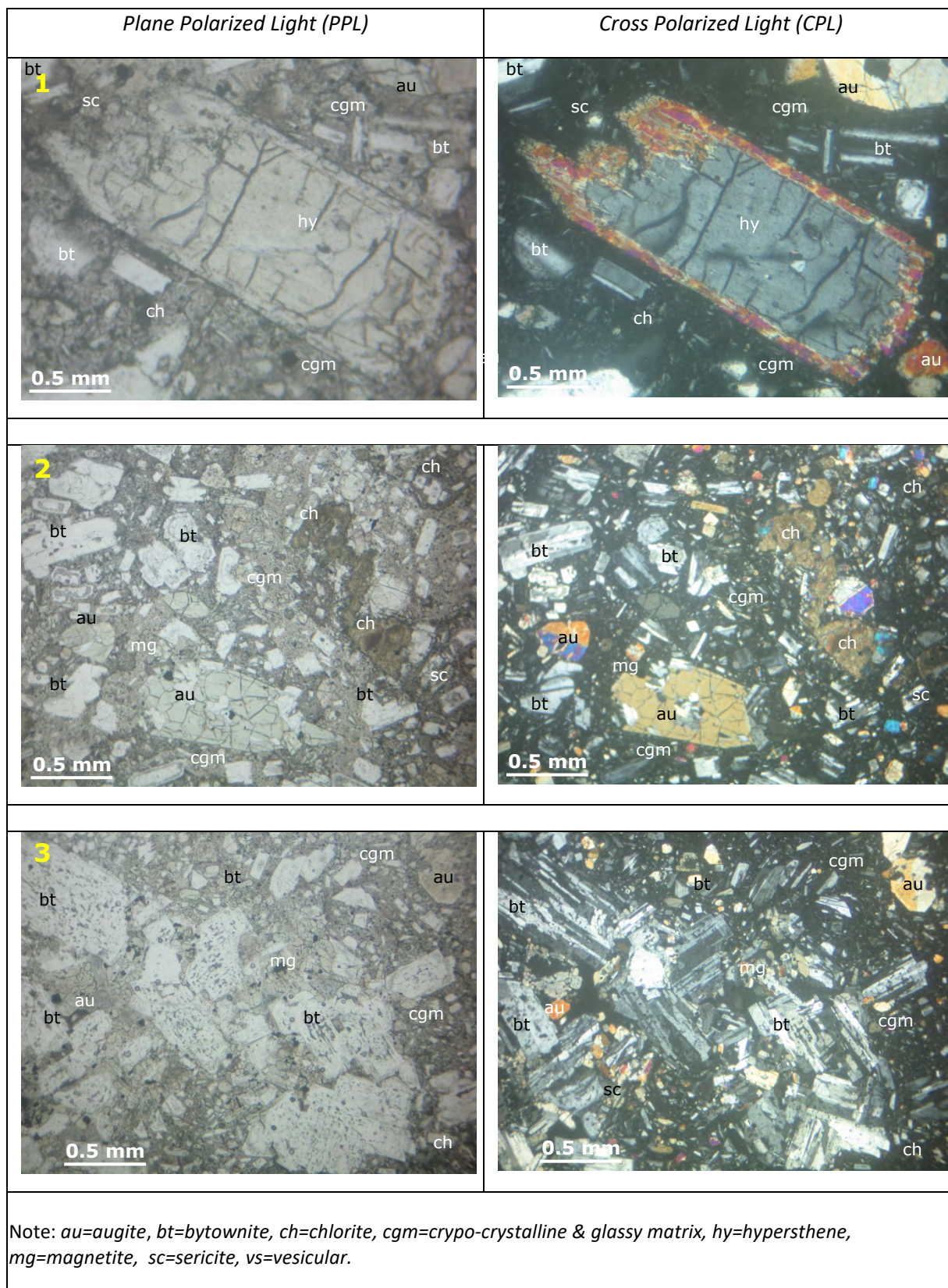
55% The groundmass consisting of microlite plagioclase feldspar, very fine grained mafic mineral and glassy matrix which are partly altered to chlorite and sericite

REMARKS

The sample contain some small vesicular holes (0.3mm in diameter) which indicated upper part of lava sequences or shallow basaltic intrusion. The chlorite and sericite content of the altered pyroxene and feldspar plagioclase is also low

PHOTO PLATES

Sample No. GP-01; 2.85



2. Sample No. GP-01; 9.55 m depth

STEREOSCOPIIC CHARACTERISTIC

Field Name : Pyroxene Basalt Andesite
 Nature of Sample : Small core sample
 Minerals Visible : Feldspars, pyroxene, chlorite, and opaques.
 Texture : Porphyritic (\varnothing 0.5-1.2mm) in very fine grained, slightly oriented groundmass
 Colour : Dark grey - black
 Grain Size : Fine grained
 Other Comments : This weakly microfractured volcanic rock appears under a binocular microscope and hand lens to be a slightly metasomatically altered pyroxene basalt.

MICROSCOPIC CHARACTERISTICS

Constituents : (Percent visual estimate)

This slightly altered basalt displays porphyritic texture consisting of phenocrysts feldspar and mafic minerals (0.5-1.2mm) set in slightly oriented glassy matrix and cryptocrystalline.

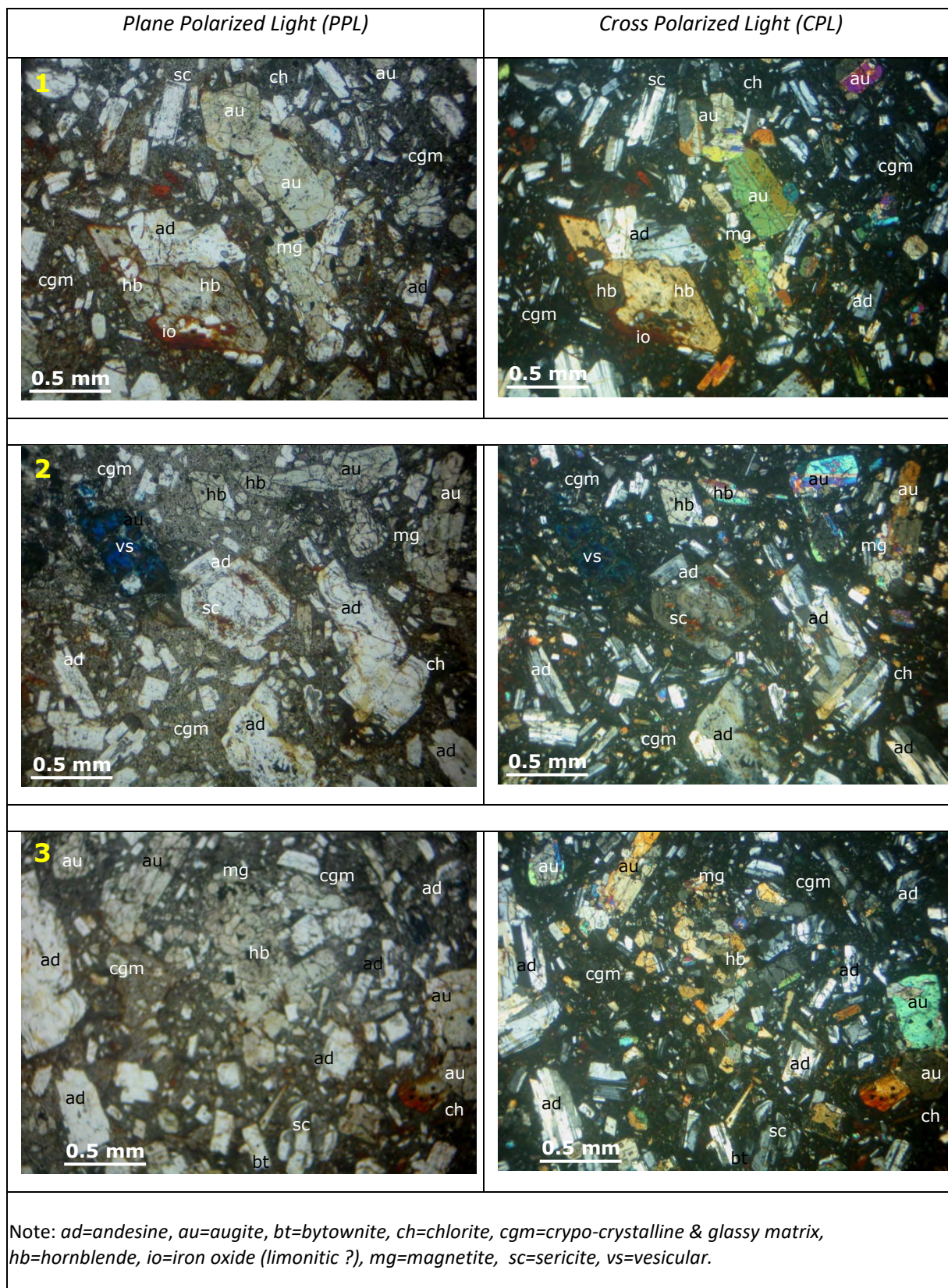
- 27% Feldspar consisting of labradorite until andesine composition, colorless, occurs as phenocrysts (0.3-0.9mm) and groundmass. Some of the phenocrysts retain lath shaped crystal with An₇₅. Part of this mineral are zoned, interlocking and slightly oriented tabular. Evidence of rare sericitic alteration of plagioclase is mainly rimmed crystal border.
- 13% Mafic mineral is mainly represented by clino-pyroxene of augite and hornblende partly slightly altered to very fine aggregates of chlorite and iron oxide. Most of this mineral present as primary igneous origin respectively, occur in about equal abundance as fine tabular and prismatic euhedral.
- 2% Opaque minerals are sparsely disseminated and represented mostly by magnetite.
- 58% The groundmass consisting of microlite plagioclase feldspar, very fine grained mafic mineral and glassy matrix which are partly altered to chlorite and sericite

REMARKS

The sample contain some small vesicular holes (0.3mm in diameter) which indicated lower part of lava sequences or shallow basaltic intrusion. The chlorite and sericite content of the altered pyroxene and feldspar plagioclase is an indication of hydrothermal effect.

PHOTO PLATES

Sample No. GP-01; 9.55 m depth



3. Sample No. GP-01; 26.00 m depth

STEREOSCOPIIC CHARACTERISTIC

Field Name : Pyroxene Basalt
 Nature of Sample : Small core sample
 Minerals Visible : Feldspars, pyroxene, chlorite, and opaques.
 Texture : Porphyritic (\varnothing 0.5-1.2mm) in very fine grained, slightly oriented groundmass
 Colour : Dark grey - black
 Grain Size : Fine grained
 Other Comments : This weakly microfractured volcanic rock appears under a binocular microscope and hand lens to be a slightly metasomatically altered pyroxene basalt.

MICROSCOPIC CHARACTERISTICS

Constituents : (Percent visual estimate)

This slightly altered basalt displays porphyritic texture consisting of phenocrysts feldspar and mafic minerals (0.5-1.2mm) set in slightly oriented glassy matrix and cryptocrystalline.

25% Bytownite colorles, occurs as phenocrysts (0,3-1,2mm) and groundmass. Some of the phenocrysts retain lath shaped crystal with An₇₅. Part of this mineral are zoned, interlocking and slightly oriented tabular. Evidence of rare sericitic alteration of bytownite can be seen in places.

15% Mafic mineral is mainly represented by clino-pyroxene of augite and scarcely olivine partly slightly altered to very fine aggregates of sericite, chlorite and clay minerals. Most of this mineral present as primary igneous origin respectively, occur in about equal abundance as fine tabular and prismatic euhedral.

5% Opaque minerals are sparsely disseminated and represented mostly by magnetite.

55% The groundmass consisting of microlite plagioclase feldspar, very fine grained mafic mineral and glassy matrix which are partly altered to chlorite and sericite

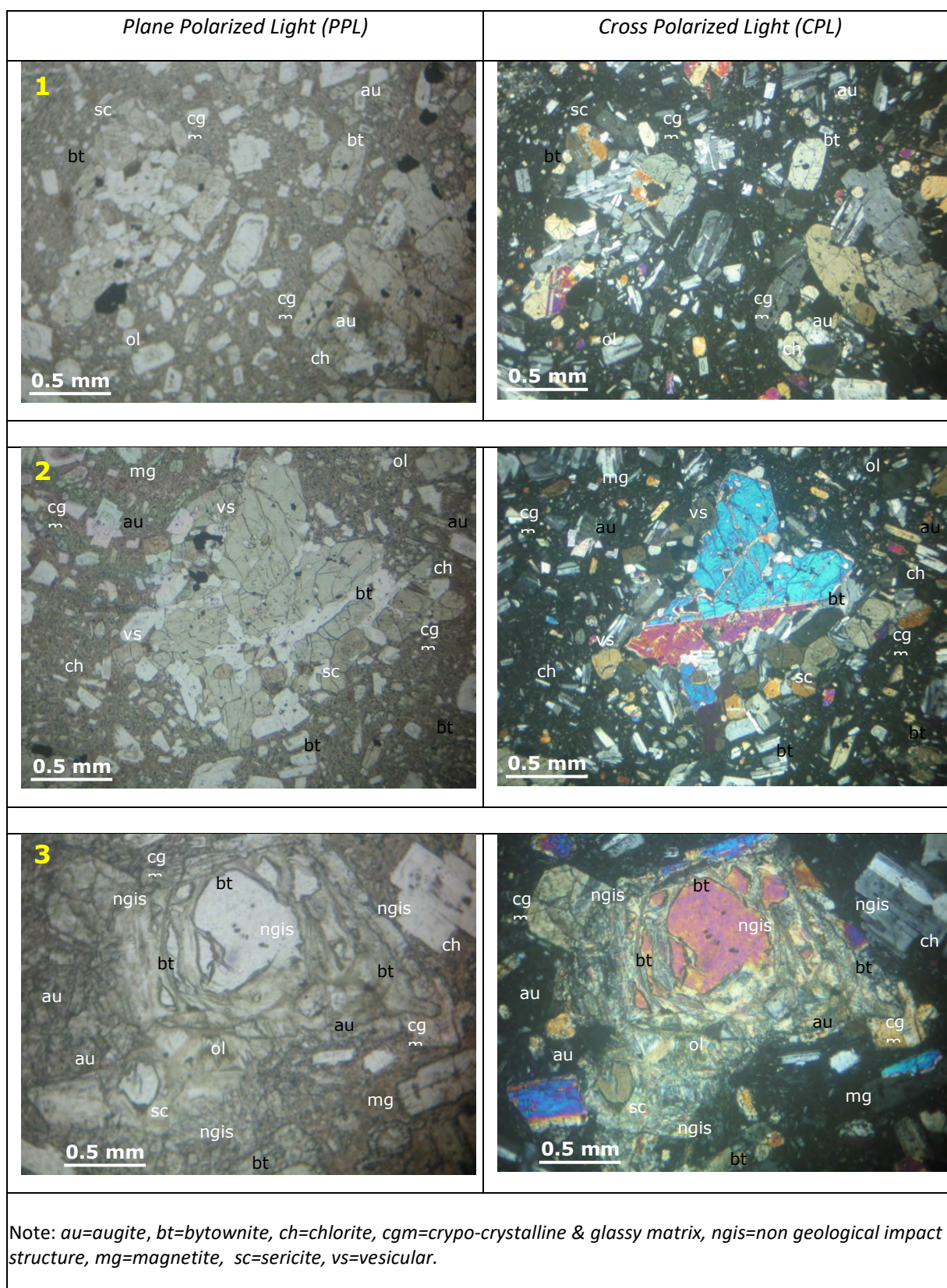
REMARKS

The sample contain some small vesicular holes (1-2mm in diameter) which indicated lower part of lava sequences or shallow basaltic intrusion. The chlorite and sericite content of the altered pyroxene and feldspar plagioclase is also low, so that may be the presence of the volcanic glass in the groundmass should be taken in account. Other thing which should be

taken in attention is the occurrences of “non geological impact microfracture” which filled by opaque minerals.

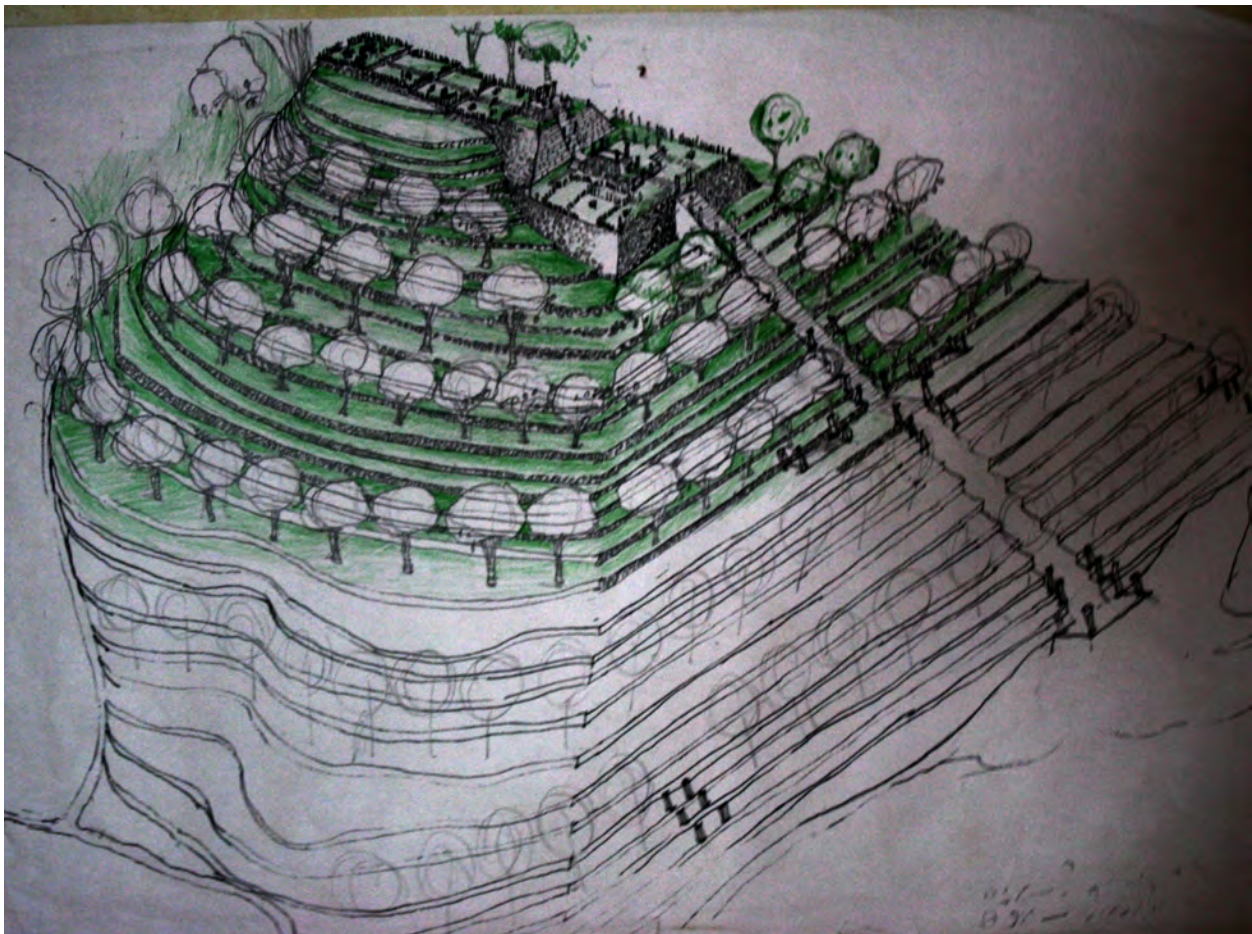
PHOTO PLATES

Sample No. GP-01; 26.00m



SUPPLEMENTARY FIGURE – K IMAGINARY ARCHITECTURES OF GUNUNG PADANG

Below are artistic interpretations and conceptual sketches of Gunung Padang's architecture, inspired by the findings of this study, the traditional wisdom of the Sundanese culture, and artistic perceptions. These sketches, created by Pon Purajatnika, are not intended for scientific purposes but to evoke positive ideas and intuitive interpretations.



Sup. Figure K.1. shows an imaginary architectural sketch of the Unit-1 construction of Gunung Padang by Pon Purajatnika. The sketch depicts an artistic interpretation of the structure based on the study results, traditional wisdom of the living-landscape concept in Sundanese culture, and artistic perceptions.



(a)



(b)

Sup. Figure K.2. An architectural sketch of the Unit-2 construction of Gunung Padang by Pon Purajatnika (a) depicts an imaginary sketch focusing on the surrounding landscape. The sketch offers an artistic representation of the environment in which Unit-2 is situated, (b) A zoom of the Unit-2 pyramid construction.

SUPPLEMENTARY FIGURE – L SELECTED PHOTO OF EVENTS AND PEOPLE

Selected photographs capturing the people and various activities conducted in Gunung Padang during the field study period from 2012 to 2014.



(a)



(b)



(c)



(d)



(e)



(f)

Sup. Figure L.1. (a) - (d) President Susilo Bambang Yudhoyono's visit on 26 February 2014. (e) - (f) Ministry of Education and Culture (Prof. M. Nuh), Vice Governor of West Java Province (Mr. Dedy Mizwar), and the Regent of Cianjur District during their visit in September 2014.



(a)



(b)



(c)



(d)

Sup. Figure L.2. (a) Chief of Army Gen. Gatot Nurmantyo and his staff visiting Gunung Padang in January 2012, (b) In Jakarta before heading to Gunung Padang with a helicopter, (d) – (e) Observing and taking photographs from the helicopter.



(a)



(b)



(c)



(d)



(e)



(f)

Sup. Figure L.3. (a) Explaining about trenching, (b) Geological discussion in the trench, (c) Discussing the stone wall of Unit 1 behind T1, (d) Field excursion with the Indonesian Association of Geophysicists, (e) Field excursion with young scientists from the Indonesian Association of Geologists, (f) After discussions with the Ministry of Education and Cultures, archaeologists from the University of Indonesia, and local communities.